

Skin-Friction and Forced Convection from Rough and Smooth Plates

Aubrey G. Jaffer
e-mail: agj@alum.mit.edu

Abstract

By introducing the concept of self-similar roughness, skin-friction coefficient and forced convection formulas are derived for a plate given its characteristic length, root-mean-squared (RMS) height-of-roughness, isotropic spatial period, and the fluid's Prandtl number. Compared with this novel theory, the RMS relative error (RMSRE) of friction measurements from Pimenta, Moffat, and Kays (1975) is 4.5%. RMSRE is 3.3% and 4.4% from Bergstrom, Akinlade, and Tachie (2005) wire meshes and perforated sheets. RMSRE is 1.7% from this investigation's convection experiments.

Further analysis of self-similar roughness leads to turbulent friction coefficient and forced convection from a smooth plate. This friction formula matches measurements by Smith and Walker (1959) and Spalding and Chi (1964) with unprecedented 0.75% RMSRE. Friction data-sets by Zukauskas and Šlančiauskas (ZS) (1987) yield RMSRE between 2.5% and 5.2%.

Laminar oscillations discovered by Tuck and Kouzoubov (1995) mimic flow along small periodic roughness, leading to comprehensive smooth friction and convection formulas from either critical Reynolds number or free-stream turbulence ratio. Friction measurements by Gebers (1920) yield 2.8% RMSRE. Convection data-sets by ZS yield RMSRE between 1.0% and 6.7%.

Table of Contents

1. <i>Introduction</i>	2
2. <i>Materials and Methods</i>	4
3. <i>Roughness Metrics</i>	5
4. <i>Formulas From Prior Works</i>	6
5. <i>Rough Turbulence</i>	7
6. <i>Smooth Turbulence</i>	10
7. <i>Spectral Roughness</i>	12
8. <i>Periodic Roughness</i>	13
9. <i>Onset of Rough Turbulence</i>	14
10. <i>Plateau Roughness</i>	15
11. <i>Local Skin-Friction Coefficients</i>	17
12. <i>Forced Convection</i>	19
13. <i>Combining Transfer Processes</i>	23
14. <i>Smoothness</i>	25
15. <i>Free-Stream Turbulence</i>	34
16. <i>Fully Rough Regime Friction</i>	36
17. <i>Friction Measurements of Diverse Types of Roughness</i>	37
18. <i>Rough Convection Measurements</i>	40
19. <i>Results</i>	42
20. <i>Discussion</i>	43
21. <i>Conclusions</i>	44
22. <i>Nomenclature</i>	46
23. <i>References</i>	47
24. <i>Appendix A: Convection Measurement Apparatus and Methodology</i>	50
25. <i>Appendix B: Thermal and Transport Properties of Humid Air</i>	56

1. Introduction

Drag is the pressure opposing fluid flow by an object. Drag consists of “form drag” from fluid deflection around the object, and “skin-friction drag” (or “resistance”) from dissipation of the viscous friction stress (shearing stress) generated by flow along the object’s surface. Related to skin-friction, “forced convection” is the heat transfer to or from a surface induced by fluid flow along that surface. Skin-friction and forced convection are fundamental processes with applications from engineering to geophysics.

- This investigation seeks to predict the skin-friction and forced convection from rough plates.

1.1 Pipe-Plate Analogy. Circa 1930, Prandtl [1] and von Kármán [2] developed theories for resistance along (smooth) plates from the results of research on flow through pipes; this is the “pipe-plate analogy”.

In 1934, Prandtl and Schlichting [3] developed a theory of skin-friction resistance for rough plates based on their analysis of Nikuradse’s [4] measurements of sand glued inside pipes (“sand-roughness”). The conclusion of the (translated) paper states:

“The resistance law just derived for rough plates has chiefly validity for a very specific type of roughness, namely a smooth surface to which sand grains have been densely attached and where the Nikuradse pipe results have been taken as the basis. . .

A single roughness parameter (the relative roughness) will in all likelihood no longer answer the purpose in continued investigations of the roughness problem.”

In 1936, Schlichting [5] investigated the velocity field and resistance of water flowing through a closed rectangular channel having one wall replaced in turn by a series of plates, each having an array of identical protrusions attached: spheres, spherical caps (bumps), or cones. The protrusions were positioned on the plates in a hexagonal array which was elongated 15% in the direction of flow.

With significant pressure drop between inflow and outflow of the channel, it was not an instance of the isobaric (no pressure drop) flow which can occur along external plates. The similarity of channel and pipe flows is well known, but neither supports nor refutes treating rough pipe interiors and plates analogously.

In 1954, Hama [6] described three challenges of the pipe-plate analogy:

“Now there is no obvious reason why pipe flow and boundary-layer flow should be identical or even similar. First, a pressure gradient is essential for flow through a pipe but not along a plate. Second, pipe flow is confined and perforce uniform, while flow along a plate develops semi-freely and bears no such a priori guarantee of displaying similar velocity profiles at successive sections. Finally, the diameter and roughness size are the only geometrical dimensions of established flow in pipes, whereas at least three linear quantities are necessary to characterize the boundary-layer.”

1.2 Boundary-Layer. Fluid in contact with the plate surface has 0 velocity. The “boundary-layer” is flow near the surface which has a velocity different from the bulk flow (or “free-stream”) velocity u .

Hama attempted to confirm the rough pipe-plate analogy with measurements of wire screens affixed to smooth plates, but concluded that it was confirmed only in the fully rough regime (defined below).

1.3 Sand-Roughness. Prior works [3, 4, 5, 6, 7, 8, 9, 10, 11] specify sand-roughness k_S , the height of “coarse and tightly placed roughness elements such as, for example, coarse sand grains glued on the surface” (Schlichting [9]).

Testing a machined analogue of sand-roughness circa 1975, Pimenta, Moffat, and Kays [7] stated that, while agreement with the Prandtl-Schlichting model was “rather good” in the fully rough regime, the apparatus’s behavior differed from “Nikuradse’s sand-grain pipe flows in the transition region.”

Modeling the wake component of the velocity profile, in 1985 Mills and Hang [8] presented a formula improving the match with Pimenta et al. data in the rough regime; it did not address other flow regimes.

1.4 Flow Regimes. Along with laminar flow, the theory for flow within pipes (and channels) distinguishes three turbulent flow regimes: smooth, (fully) rough, and transitional. Smooth turbulent pipe flow encounters viscous resistance varying inversely with the fluid velocity per viscosity ratio. Rough pipe flow encounters resistance varying with the height-of-roughness, while largely insensitive to viscosity. The transitional regime describes the range of flow rates where both viscosity and roughness affect the resistance (Colebrook [12]).

1.5 Reynolds Number. The Reynolds number (Re) represents the bulk fluid flow rate (far from the plate); Re with a subscript represents other flow rates. The local Reynolds number $Re_x = x Re/L$, where x

is the distance from the leading edge of the plate in the direction of flow, and characteristic length L is the length scale for the physical system. Unless stated otherwise, L is the plate length in the direction of flow.

1.6 Skin-Friction Coefficient. Skin-friction in prior works is represented by the (dimensionless) local drag coefficient c_f or C_f , a function of the relative sand-roughness x/k_S and Re or a subscripted Re .

Prandtl and Schlichting [3] specified the boundaries between flow regimes using the “sand-roughness Reynolds number” Re_k . For plates, it assigned the boundaries between smooth, transitional, and rough regimes at $Re_k = 7.08$ and 70.8 . Pimenta et al. [7] gave $Re_k = 65$ as the transitional-to-rough boundary.

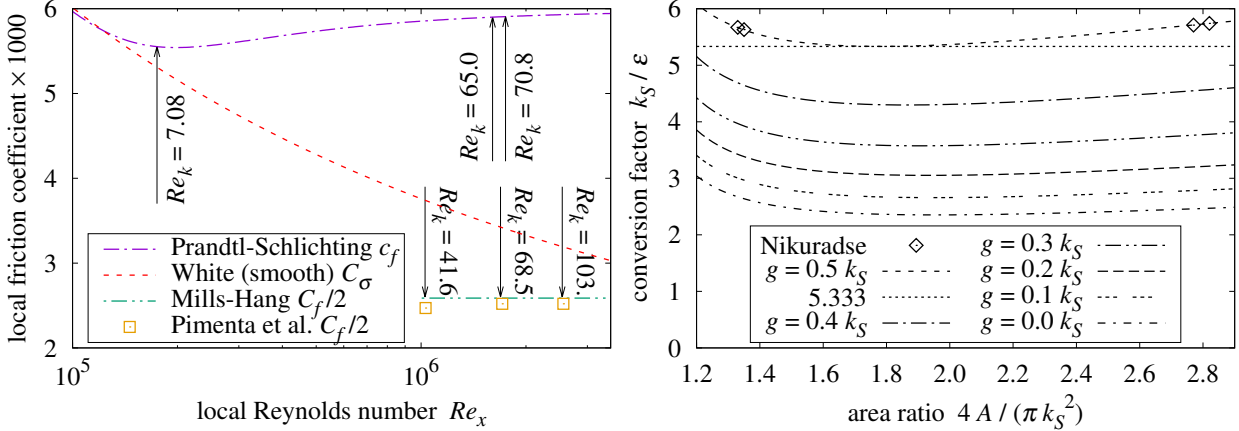


Figure 1 Local c_f versus Re_x

Figure 2 k_S/ε versus cell area of sand-roughness

Figure 1 presents skin-friction coefficient curves, Re_k regime boundaries, and measurements from the Pimenta et al. [7] plate having $k_S = 0.794$ mm at $x = 0.965$ m.

1.7 Plate Flow Versus Pipe Flow. Schlichting [9] states: “The resistance to flow offered by rough walls [of pipes] is larger than that . . . for smooth pipes.”

The rough pipe-plate analogy holds that this rule also applies to rough, external plates. For example, the “Prandtl-Schlichting c_f ” curve is never less than the “White (smooth) C_σ ” curve in Figure 1.

The Pimenta et al. measurements are much closer to $c_f/2$ than they are to c_f .¹ Pimenta et al. [7] and Mills and Hang [8] both designated $c_f/2$ as the friction coefficient. All three measurements in Figure 1 are less than the smooth turbulent coefficient C_σ . If rough friction is never less than smooth friction, then these measurements must not be in any turbulent flow regime; the remaining alternative is laminar flow. Laminar flow coefficients have a steeper slope than C_σ ; yet these measurements are near the constant level predicted by Mills-Hang $C_f/2$ for the rough regime.

- The pipe-plate analogy fails for roughness because rough turbulent skin-friction coefficients can be less than smooth turbulent coefficients for external plates, but not inside pipes.

1.8 More Recent Work. With the rough pipe-plate analogy’s failure obscured by the factor of 2, research based on the pipe-plate analogy continued. The 2004 survey article Jiménez [13] did not question the rough pipe-plate analogy, writing: “The theoretical arguments are sound, but the experimental evidence is inconclusive.”

Circa 2005, Bergstrom, Akinlade, and Tachie [14], performed experiments with sandpapers, woven wire meshes, and perforated sheets attached onto a flat plate, reporting that: $\sqrt{C_f} = [0.360 \pm 0.025] \delta^*/\delta$, where δ^* is the displacement thickness and δ is the 99% velocity boundary-layer thickness. As a function of a roughness metric, this formula has no predictive value because both δ^* and δ must be inferred from velocity field measurements along the surface under test. Fortunately, Bergstrom et al. included free-stream velocity in their tables, allowing comparisons of their skin-friction data with the present theory.

- Sand-roughness’s lack of generality, the need for additional roughness parameters, and the failure of the pipe-plate analogy for roughness motivate a fresh theoretical analysis of isobaric flow along a rough plate, an analysis derived from traceable roughness metrics.

¹ The Bergstrom, Akinlade, and Tachie [14] local friction coefficient (C_f) measurements of woven wire meshes and perforated sheets (present work Section 17) are also much closer to $c_f/2$ than c_f .

2. Materials and Methods

2.1 Not Empirical. Empirical theories derive their coefficients from measurements, inheriting the uncertainties from those measurements. Theories developed from first principles derive their coefficients mathematically. For example, the Blasius model of laminar flow coefficient $0.3320+$ is the solution of a differential equation (Lienhard and Lienhard [15]). Another example is the heat conduction shape factor for one face of a disk, which is exactly twice its diameter. The present theory derives from first principles; it is not empirical. Each formula is tied to aspects of the plate geometry, fluid, and flow.

2.2 Mathematics. Familiarity with calculus is assumed. Computational geometry, probability, self-similar recurrences, the Lambert W function, vector-space norms, and Fourier transforms are also employed; each is briefly introduced or illustrated graphically. Differential equations are not explicitly used.

Table 1 Sources of friction measurements

Source	Measured Quantity	Pr_∞	$Re \geq$	$Re \leq$	\pm	Count
[11, 16, 17] Churchill	smooth turbulent average, air	0.71	1.0×10^5	1.0×10^9		9
[11, 16, 17] Churchill	smooth turbulent local, air	0.71	1.0×10^5	1.0×10^{10}		11
[18] Žukauskas & Šlančiauskas	smooth turbulent local, oil	55.2	3.6×10^5	1.1×10^7		5
[18] Žukauskas & Šlančiauskas	smooth turbulent local, water	5.42	3.6×10^5	2.4×10^6		8
[18] Žukauskas & Šlančiauskas	smooth turbulent local, water	2.78	7.2×10^5	4.4×10^6		8
[18] Žukauskas & Šlančiauskas	smooth turbulent local, air	0.71	7.6×10^5	3.2×10^6		9
[19, 20] Gebers	smooth transition average		7.4×10^5	3.3×10^7		33
[7] Pimenta et al.	packed sphere rough local, air	0.71	3.8×10^5	5.8×10^6	10%	19
[14] Bergstrom et al.	smooth turbulent local, air	0.71	1.6×10^6	4.6×10^6	5%	4
[14] Bergstrom et al.	wire mesh rough local, air	0.71	1.6×10^6	4.7×10^6	9%	12
[14] Bergstrom et al.	perforated sheet local, air	0.71	1.6×10^6	4.6×10^6	9%	12

Note: Churchill [11] extracted its measurements from Smith and Walker [16] and Spalding and Chi [17].

Table 2 Sources of convection measurements

Source	Measured Quantity	Pr_∞	$Re \geq$	$Re \leq$	\pm	Count
[21] Kestin et al.	UWT transition local, air	0.7	3.8×10^4	3.5×10^5		13
[21] Kestin et al.	UWT transition local, air	0.7	4.3×10^4	2.9×10^5		7
[22] Reynolds et al.	UWT transition local, air	0.71	8.2×10^4	1.1×10^6	4%	22
[18] Žukauskas & Šlančiauskas	UHF transition local, air	0.71	1.1×10^4	8.2×10^5	5%	10
[18] Žukauskas & Šlančiauskas	UHF transition local, air	0.71	1.1×10^4	8.2×10^5	5%	10
[18] Žukauskas & Šlančiauskas	UHF transition local, air	0.71	1.1×10^4	8.2×10^5	5%	10
[18] Žukauskas & Šlančiauskas	UHF transition local, water	6.57	4.0×10^3	2.2×10^5	10%	19
[18] Žukauskas & Šlančiauskas	UHF transition local, water	6.57	5.0×10^3	2.2×10^5	10%	15
[18] Žukauskas & Šlančiauskas	UHF transition local, oil	108.	3.0×10^4	3.0×10^5	5%	17
[18] Žukauskas & Šlančiauskas	UHF transition local, oil	257.	1.2×10^4	1.1×10^5	5%	17
[18] Žukauskas & Šlančiauskas	UWT average, air	0.71	1.1×10^5	6.3×10^5	5%	16
[18] Žukauskas & Šlančiauskas	UWT average, air	0.71	1.7×10^5	7.5×10^5	5%	19
[18] Žukauskas & Šlančiauskas	UWT average, water	5.8-7.1	1.4×10^6	2.3×10^6	10%	5
[18] Žukauskas & Šlančiauskas	UWT average, water	2.9-7.2	2.1×10^5	6.4×10^6	10%	21
[18] Žukauskas & Šlančiauskas	UWT average, water	2.0-5.8	1.8×10^5	1.4×10^6	10%	40
[18] Žukauskas & Šlančiauskas	UWT average, oil	75-246	5.0×10^4	7.0×10^5	5%	40
[18] Žukauskas & Šlančiauskas	UWT average, oil	80-205	1.1×10^5	3.6×10^5	5%	11
[18] Žukauskas & Šlančiauskas	UWT average, oil	92-317	2.7×10^4	7.5×10^5	5%	29
present apparatus $\varepsilon = 3.00$ mm	UWT rough average, air	0.71	2.3×10^3	9.3×10^4	3-7%	13
present apparatus $\varepsilon = 1.04$ mm	UWT plateau average, air	0.71	2.0×10^3	6.8×10^4	2-6%	14

Note: UHF is uniform heat flux; UWT is uniform wall temperature.

2.3 Measurement Data-Sets. Tables 2 and 1 list the data-sets to be compared with the present theory.

Rough surface convection measurements were obtained from an apparatus built for this investigation, which measured average convection in air at $2300 < Re < 93000$. Section 24 describes this apparatus and its measurement methodology. Section 18 presents its measurements.

The Gebers [19, 20] skin-friction measurements were captured from a graph in Schlichting [9] by measuring the distance from each point to the graph’s axes, then scaling to the graph’s units using the “Engauge” software. The remaining measurement data-sets were manually entered from tables in the cited works. Several obvious single-digit typographical errors were corrected.

Two non-obvious single digit errors in the text of a prior work are detailed in Section 17.

2.4 RMS Relative Error.

The “±” column of Tables 1 and 2 lists the estimated measurement uncertainties stated by the cited studies. While essential to empirical theories, these estimates are merely indicative for non-empirical theories.

Root-mean-squared relative error (RMSRE) provides an objective, quantitative evaluation. It gauges the fit of measurements $g(Re_j)$ to function $f(Re_j)$, giving each of the n samples equal weight in formula (1).

$$\sqrt{\frac{1}{n} \sum_{j=1}^n \left| \frac{g(Re_j)}{f(Re_j)} - 1 \right|^2} \quad (1)$$

$$\text{bias} = \frac{1}{n} \sum_{j=1}^n \left\{ \frac{g(Re_j)}{f(Re_j)} - 1 \right\} \quad \text{scatter} = \sqrt{\frac{1}{n} \sum_{j=1}^n \left| \frac{g(Re_j)}{f(Re_j)} - 1 - \text{bias} \right|^2} \quad (2)$$

Along with presenting RMSRE, charts in the present work split RMSRE into the bias and scatter components defined in formula (2). The root-sum-squared (RSS) of bias and scatter is RMSRE.

3. Roughness Metrics

Two established, traceable roughness metrics are the root-mean-squared (RMS) height-of-roughness and the arithmetic-mean height-of-roughness. For an elevation function $z(x, y)$ defined on area A having a convex perimeter, its mean elevation \bar{z} and RMS height-of-roughness ε are:

$$\bar{z} = \frac{\int_A z \, dA}{\int_A dA} \quad (3)$$

$$\varepsilon = \sqrt{\frac{\int_A |z - \bar{z}|^2 \, dA}{\int_A dA}} \quad (4)$$

The arithmetic-mean height-of-roughness is defined in terms of the same mean elevation \bar{z} formula (3):

$$\frac{\int_A |z - \bar{z}| \, dA}{\int_A dA} \quad (5)$$

3.1 Sand-Roughness. Modeling sand-roughness grains as diameter k_S spheres sitting in a pool of depth g glue, the mean elevation \bar{z} of a cell of area A containing one sphere is:

$$\bar{z} = g + \frac{5 \pi k_S^3}{24 A} - \frac{\pi k_S^2 g}{4 A} \quad (6)$$

With the cell’s RMS height-of-roughness ε computed from formula (4), Figure 2 shows k_S/ε versus the ratio of cell area to the sphere’s shadow area, at six glue-levels between 0% and 50% of k_S . Table 3 lists k_S , grain densities, and k_S/ε conversion factors for Nikuradse’s [4] sand coatings, assuming $g = 0.5 k_S$.

Table 3 Nikuradse’s sand coatings at $g = 0.5 k_S$

k_S	grains/cm ²	k_S/ε
.08 cm	150	5.67
.04 cm	590	5.63
.02 cm	1130	5.74
.01 cm	4600	5.71

3.2 Conversions. Afzal, Seena, and Bushra [23] fitted 5.333 as the RMS to sand-roughness conversion factor k_S/ε , and 6.45 as the arithmetic-mean to sand-roughness conversion factor (both in pipes).

$k_S/\varepsilon = 5.333$ is a broad minimum of the $g = 0.5 k_S$ curve in Figure 2.

The “ k_S/ε ” column values in Table 3 (“Nikuradse” in Figure 2) match each other within 2%. The tightest spread on Table 3 data with the arithmetic-mean height-of-roughness exceeds 20%. Thus, sand-roughness correlates an order of magnitude more strongly with RMS than arithmetic-mean height-of-roughness.

Flack, Schultz, Barros, and Kim [24] measured skin-friction from grit-blasted surfaces in a duct, writing “The root-mean-square roughness height is shown to be most strongly correlated with the equivalent sand-roughness height (k_S) for the grit-blasted surfaces.”

- Arithmetic-mean height-of-roughness will not be considered further by this investigation.

3.3 Packed Spheres Roughness. The Pimenta et al. [7] plate was composed of 11 layers of closely packed 1.27 mm diameter metal spheres “arranged such that the surface has a regular array of hemispherical roughness elements.” Joined by brazing, there was no pool of glue surrounding the spheres. Shrinking the cell to the sphere’s shadow, $\pi k_S^2/4$, the RMS height-of-roughness of the top half of the 1.27 mm sphere is 0.150 mm. Pimenta et al. gave $k_S = 0.794$ mm; $k_S/5.333 \approx 0.149$ mm, which matches 0.150 mm within 1%.

- This investigation will use $k_S/\varepsilon = 5.333$ as the RMS to sand-roughness conversion factor.

4. Formulas From Prior Works

Several prior works gave formulas for skin-friction coefficient in the fully rough regime.

4.1 Prandtl and Schlichting. In *Boundary-layer theory* [9], Prandtl and Schlichting gave formulas for fully rough local (c_f) and plate average ($\overline{c_f}$) skin-friction coefficient for a rough plate as a function of x/k_S and L/k_S , respectively:

$$c_f = \left[2.87 + 1.58 \log_{10} \frac{x}{k_S} \right]^{-2.5} \quad x \leq L \quad (7)$$

$$\overline{c_f} = \left[1.89 + 1.62 \log_{10} \frac{L}{k_S} \right]^{-2.5} \quad 10^2 < \frac{L}{k_S} < 10^6 \quad (8)$$

4.2 Mills and Hang. Mills and Hang [8] gave a formula (9) which is more accurate than formula (7) on the local skin-friction measurements from Pimenta et al. [7]. Their local (C_f) and average ($\overline{C_f}$) coefficient formulas were:

$$C_f = \left[3.476 + 0.707 \ln \frac{x}{k_S} \right]^{-2.46} \quad 750 < \frac{x}{k_S} < 2750 \quad (9)$$

$$\overline{C_f} = \left[2.635 + 0.618 \ln \frac{L}{k_S} \right]^{-2.57} \quad (10)$$

4.3 White. White [10] gave formula (11) for fully rough local skin-friction coefficient:

$$C_f = \left[1.4 + 3.7 \log_{10} \frac{x}{k_S} \right]^{-2} \quad \frac{x}{k_S} > \frac{Re_x}{1000} \quad (11)$$

White is also the source of a widely used formula for turbulent skin-friction coefficient of smooth plates:

$$C_\sigma(Re_x) = \frac{0.455}{\ln^2(0.06 Re_x)} \quad (12)$$

4.4 Average Coefficient. Mills and Hang [8] derived the average formula (10) from the local formula (9) by fitting a curve to the result of a numerical integration such as formula (13):

$$\overline{C_f} \left(\frac{L}{k_S} \right) = \frac{k_S}{L - L_0} \int_{L_0/k_S}^{L/k_S} C_f(x) dx \quad (13)$$

The local formulas (7), (9), and (11) each have a singularity where the expression containing the logarithm is 0. The lower limit of integration (L_0/k_S) must be large enough to avoid this; but the lower limit is not revealed in the prior works. The averaging formula (13) is quite sensitive to the lower limit because the largest value of the local formula occurs there.

For the Mills-Hang formula (9), with lower bound $L_0/k_S = 1.6$ and initial $dx/k_S = 0.01$, integration of the local C_f is within $\pm 0.5\%$ of the average $\overline{C_f}$ in formula (10) over the range $200 < x/k_S < 2 \times 10^5$.

For the Prandtl-Schlichting formula (7), with lower bound $L_0/k_S = 0.5$ and initial $dx/k_S = 0.5$, integration of the local c_f is within $\pm 0.5\%$ of the average $\overline{c_f}$ in formula (8) over the range $200 < x/k_S < 2 \times 10^5$.

4.5 Churchill. Churchill [11] compared 8 formulas from diverse sources versus the data from Pimenta et al. [7], finding none significantly closer to the measurements than the Mills-Hang local formula (9).

Churchill gave distinct formulas for computing the average (mean) skin-friction C_m from local C_f for smooth and rough surfaces, respectively:

$$C_m = C_f \frac{1 - 4.516\sqrt{C_f}}{1 - 7.965\sqrt{C_f} + 21.52 C_f} \quad (14)$$

$$C_m = C_f \frac{1 - 4.516\sqrt{C_f}}{1 - 7.965\sqrt{C_f}} \quad (15)$$

Section 16 compares the local fully rough regime formulas with measurements from Pimenta et al. [7].

5. Rough Turbulence

Forced flow along a plate with a rough surface differs in character from forced flow along a smooth surface because roughness disrupts what would otherwise be a viscous sub-layer adjacent to the plate. Lienhard and Lienhard [15] teaches: “Even a small wall roughness can disrupt this thin sublayer, causing a large decrease in the thermal resistance (but also a large increase in the wall shear stress).”

Jiménez [13] wrote “In flows with $\delta/k < 50$, the effect of the roughness extends across the boundary-layer, and is also variable. There is little left of the original wall-flow dynamics in these flows, which can perhaps be better described as flows over obstacles.”

5.1 Flow Over Obstacles. This investigation focuses first on a case where flow over obstacles dominates the dynamics. It models the shearing stress of flow along a roughness which disrupts that flow at a succession of scales: $L, L/2, L/2^2, L/2^3, \dots$. While simpler surfaces may produce rough turbulence, a roughness which disrupts at all these scales surely will.

- This approach departs from prior works because their continuous boundary-layer assumption is incompatible with a roughness which disrupts boundary-layers.

5.2 Profile Roughness. Simpler than surface roughness, profile roughness is nonetheless informative.

Let a “profile roughness” be a function $z(x)$ with $0 \leq x \leq L$; its mean elevation \bar{z} and RMS height-of-roughness ϵ are computed similarly to surface roughness ε :

$$\bar{z} = \frac{1}{L} \int_0^L z(x) dx \quad (16)$$

$$\epsilon = \sqrt{\frac{1}{L} \int_0^L |z(x) - \bar{z}|^2 dx} \quad (17)$$

5.3 Self-Similar Profile Roughness. Let a “self-similar profile roughness” be a profile roughness function $z(x)$ such that the RMS height-of-roughness of $z(x)$ over an open interval is twice the RMS height-of-roughness of $z(x)$ over each half of that interval (leaving out the midpoint).

These x intervals are open (not containing the endpoint); the $z(x)$ value for each endpoint contributes to the height-of-roughness of its parent interval, but not to any sub-interval. A consequence of this definition is:

- The RMS height-of-roughness of $z(x)$ over an open interval, divided by the length of that interval will be invariant through its succession of scales.

5.4 Ramp Permutation. Of particular interest are self-similar profile roughnesses which are permutations of the linear ramp $z(x) = \zeta x/L$ with $0 \leq x \leq L$. Each elevation from 0 to peak height ζ occurs exactly once.

The only occurrence of x in formulas (16) and (17) is $z(x)$; hence the RMS height-of-roughness calculation depends only on the z values, not on their relation to x . Thus, the height-of-roughness of any ramp-permutation is identical to the height-of-roughness of the linear ramp:

$$\epsilon = \sqrt{\frac{1}{L} \int_0^L \left| \frac{\zeta x}{L} - \frac{\zeta}{2} \right|^2 dx} = \frac{\zeta}{\sqrt{12}} \quad (18)$$

5.5 Self-Similar Ramp Permutation. A self-similar integer sequence $Y(t, w)$ from integers $0 \leq t < w = 2^q$ allows self-similar behavior to be explored with a finite approximation. Letting $t = \lfloor wx/L \rfloor \equiv \text{floor}(wx/L)$ constructs a profile roughness from a sequence by $z(x) = \zeta Y(\lfloor wx/L \rfloor, w)/w$.

The following three examples are self-similar ramp-permutation sequences. Each element of the sequence is generated by calling its recurrence formula with a sequence index $0 \leq t \leq w$ and w , an integer power of 2. Each recursive call divides w by 2, terminating (and returning) when w reaches 1.

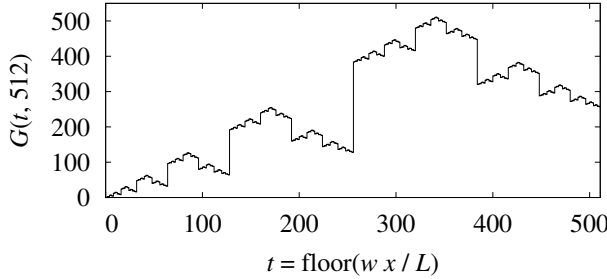


Figure 3 Gray-code profile roughness

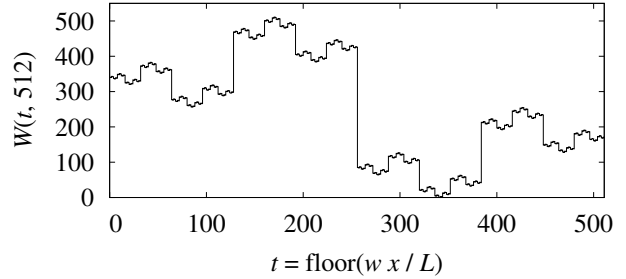


Figure 4 Wiggliest self-similar roughness

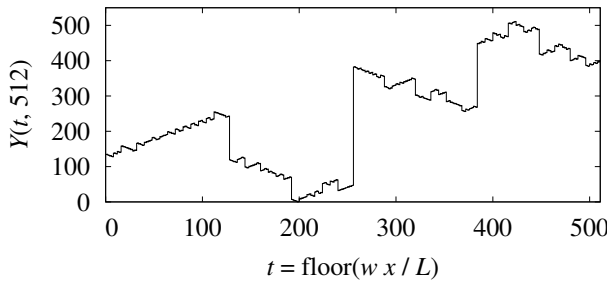


Figure 5 Random reversal profile roughness

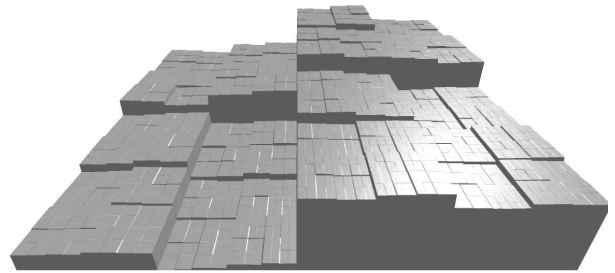


Figure 6 Random reversal ramp surface

Self-similar recurrence (19) defines the integer Gray-code sequence $G(t, w)$ shown in Figure 3.

$$G(t, w) = \begin{cases} t, & \text{if } w = 1; \\ w + G(w - 1 - (t \bmod w), w/2), & \text{if } \lfloor t/w \rfloor = 1; \\ G(t \bmod w, w/2), & \text{otherwise.} \end{cases} \quad (19)$$

Recurrence (20) defines the integer sequence $W(t, w)$ shown in Figure 4; it reverses direction at each bifurcation, yielding a wiggliest possible self-similar ramp-permutation sequence.

$$W(t, w) = \begin{cases} t, & \text{if } w = 1; \\ \lfloor t/w \rfloor w + W(w - 1 - (t \bmod w), w/2), & \text{otherwise.} \end{cases} \quad (20)$$

Figure 5 shows a sequence generated by randomly reversing or not at each bifurcation in recurrence (21). Figure 6 shows a random reversal, self-similar, ramp-permutation surface roughness.

$$Y(t, w) = \begin{cases} t, & \text{if } w = 1; \\ w + Y(w - 1 - (t \bmod w), w/2), & \text{with probability 0.5;} \\ Y(t \bmod w, w/2), & \text{otherwise.} \end{cases} \quad (21)$$

5.6 Cardinality. For a given $w = 2^q \geq 4$, there are 2^{w-1} distinct self-similar ramp-permutation sequences, but only 2 distinct ramps and 2 distinct wiggliest sequences.

5.7 Friction Travel and Velocity. In the conversion of bulk flow to rough turbulence, some particles of fluid must move in directions not parallel to the bulk flow. Such movement results from deflections of flow by roughness peaks, pits, ridges, and valleys; the amount of deflection and turbulence induced should grow with the RMS height-of-roughness.

Let “run” be the horizontal axis and “friction” be the vertical axis of a profile roughness such as in Figure 5. For an integer ramp-permutation sequence $Y(t, w)$, the sum of the (dimensionless) lengths of all its run segments is simply $w - 1 = 2^q - 1$. The sum of its friction segment lengths is:

$$\sum_{t=0}^{2^q-2} |Y(t, 2^q) - Y(t+1, 2^q)| \quad (22)$$

If a particle of fluid traces the ramp-permutation sequence $Y(t, w)$ between $t = 0$ and $t = w - 1$, then $w - 1$ is the run travel, while formula (22) is the friction travel.

Figure 7 shows the friction per run travel ratio versus $q = \log_2(w)$. The linear ramp trace has slope 0; Gray-code’s is 1/2; random reversal cases are approximately 1/2; and wiggliest roughness has slope 2/3.

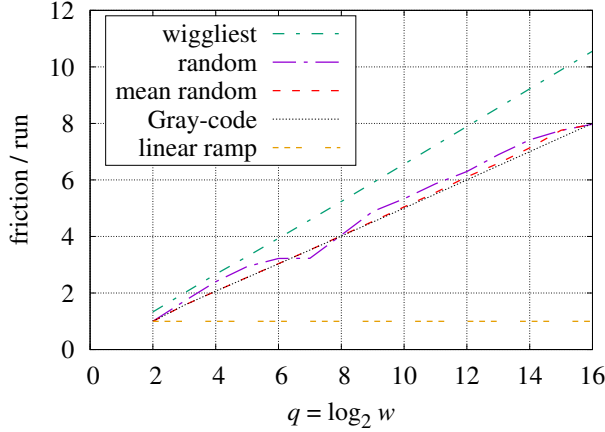


Figure 7 Travel along profile roughness

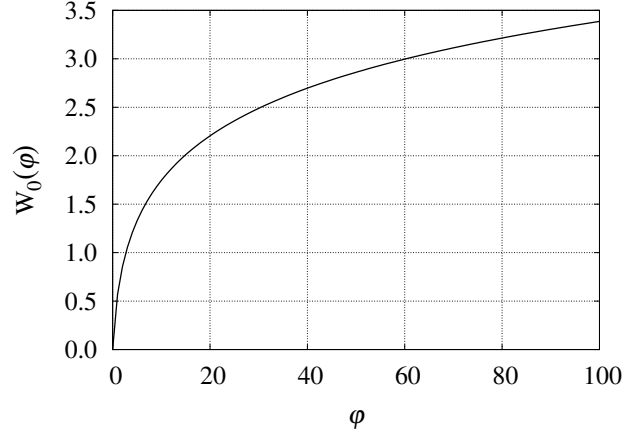


Figure 8 Lambert function W_0

5.8 Roughness Sequence Outliers. A wiggliest roughness sequence $W(t, w)$ is an extreme case; it reverses friction direction at each increment of run (t). For each wiggliest roughness sequence with $w \geq 4$ there are $2^{w-1} - 2$ other random reversal roughness sequences. In contrast, the linear ramp never reverses direction. For each linear ramp sequence there are $2^{w-1} - 2$ other random reversal sequences.

- Being outliers, $W(t, w)$ and linear ramps are excluded from further consideration as roughness.

5.9 Dimensional Analysis. Excluding the outliers, Figure 7’s friction per run ratios are about:

$$\frac{q}{2} \equiv \frac{\log_2 w}{2} \quad (23)$$

$Y(t, w)$, t , and w are dimensionless. The friction per run ratio (23) needs to be reformulated in terms of ϵ and L , which have length units. Turning to dimensional analysis, the argument to \log_2 must be

dimensionless, involve ϵ , and be greater than 1, so that the logarithm will be positive. This friction per run ratio must increase with increasing ϵ . Thus, ϵ and the logarithm will be in denominators, yielding:

$$\frac{2}{\log_2(L/\epsilon)} \quad (24)$$

Scaling formula (24) by $1/\sqrt{12}$ from formula (18) converts it into the RMS friction per run travel ratio:

$$\frac{1}{\sqrt{12}} \frac{2}{\log_2(L/\epsilon)} = \frac{1}{\sqrt{3} \log_2(L/\epsilon)} \quad (25)$$

- Considering the run travel and friction travel with respect to time lets formula (25) also serve as the friction velocity per bulk flow velocity ratio: u_τ/u .

5.10 Isotropy. Fluid particles stay within the vertical plane of profile roughness. Surface roughness deflects particles in all directions. Therefore, this investigation restricts its attention to “isotropic” roughness: rotating the flow’s azimuth (direction) in the rough surface’s plane does not substantially affect its behavior (Section 8 develops a decision procedure for roughness isotropy).

Newberry and Savage [25] demonstrated that some self-similar systems modeled using continuous power-law probability distributions can be modeled using discrete power-law distributions.

This investigation uses that idea in reverse. Formula (25) modeled flow along a discrete self-similar roughness. Formula (26) models flow along a random self-similar surface roughness (ϵ instead of ϵ) using a continuous random variable $Z > 1$ having a Pareto distribution whose probability density function is $1/Z^2$:

$$\frac{u_\tau}{u} = 1 \left/ \left[\sqrt{3} \int_\epsilon^L \frac{Z}{Z^2} dZ \right] \right. = \frac{1}{\sqrt{3} \ln(L/\epsilon)} \quad (26)$$

5.11 Shearing Stress. The skin-friction coefficient $\overline{f_c}$ is the ratio of the shearing stress τ_2 per the fluid flow’s dynamic pressure (kinetic energy density) $\rho u^2/2$, where ρ is the fluid’s density:

$$\overline{f_c} = \frac{\tau_2}{\rho u^2/2} \quad (27)$$

Both $\tau_2 = \rho u_\tau^2/2$ and $\rho u^2/2$ have units of pressure, $\text{kg}/(\text{m} \cdot \text{s}^2)$. From formula (26):

$$u_\tau = \frac{u}{\sqrt{3} \ln(L/\epsilon)} \quad \tau_2 = \frac{\rho u_\tau^2}{2} = \frac{\rho u^2}{6 \ln^2(L/\epsilon)} \quad (28)$$

- Eliminating τ_2 from formulas (27) and (28) yields the average skin-friction coefficient of an isotropic, self-similar roughness:

$$\overline{f_\rho} = \frac{1}{3 \ln^2(L/\epsilon)} \quad \frac{L}{\epsilon} \gg 1 \quad (29)$$

Sections 16 and 17 compare formula (29) with friction measurements from rough surfaces.

Note that Prandtl and Schlichting [3] calculated $\tau = \rho u_\tau^2$, not $\tau_2 = \rho u_\tau^2/2$. As a result, $\overline{c_f} \geq 2 \overline{f_\rho}$ and $c_f \geq 2 f_\rho$. Pimenta et al. [7] and Mills and Hang [8] designated $c_f/2$ as the friction coefficient.

6. Smooth Turbulence

Given $Re \gg 1$ there must be an L/ϵ so large that a length L plate with a self-similar roughness of RMS height ϵ induces skin-friction midway between that of a rough surface and that of a smooth surface.

6.1 Roughness Reynolds Number. Let the “roughness Reynolds number” Re_ϵ derive from friction velocity u_τ at scale ϵ :

$$Re_\epsilon = \frac{u_\tau \epsilon}{\nu} = \frac{Re}{\sqrt{3} [L/\epsilon] \ln(L/\epsilon)} \quad (30)$$

where ν is the fluid’s kinematic viscosity (with units m^2/s) and $Re = Lu/\nu$. The Re strength at which rough plate friction transitions to smooth plate friction should have the same Re_ϵ value at all $L/\epsilon \gg 1$. Combining $Re_\epsilon = 1$ with formula (30) relates Re and L/ϵ at this transition:

$$Re = \sqrt{3} \frac{L}{\epsilon} \ln \frac{L}{\epsilon} \quad (31)$$

Relation (31) linking Re with L/ε suggests that the smooth turbulent friction coefficient $\overline{f_\sigma}$ can be inferred by combining formulas (29) and (31). However, there being no roughness on a smooth plate, $\overline{f_\rho}$ formula (29) must be adapted for this application. Scaling $\overline{f_\rho}(L/\varepsilon)$ by $\sqrt[3]{2}$, and its argument by $1/e$:

$$\overline{f_\sigma} = \sqrt[3]{2} \overline{f_\rho} \left(\frac{L}{e\varepsilon} \right) = \sqrt[3]{2} \left[\frac{1}{3} \ln^{-2} \frac{L}{e\varepsilon} \right] \quad (32)$$

$\sqrt[3]{2}/3 \approx 0.4200$. Euler's number $e = \exp(1)$ is a fixed point of $\varphi \ln \varphi$ and its inverse, $\exp(W_0(\vartheta))$.

6.2 Lambert W Function. L/ε can be eliminated from formulas (31) and (32) using the Lambert W function's principal branch W_0 , which is defined by equivalence (33) and plotted in Figure 8.

$$\vartheta = \varphi \exp \varphi \Leftrightarrow \varphi = W_0(\vartheta) \quad (33)$$

$$\vartheta = \varphi \ln \varphi \Leftrightarrow \varphi = \exp W_0(\vartheta) \quad (34)$$

The related equivalence (34) lets $\exp(W_0(Re/\sqrt{3}))$ replace L/ε in formula (32) when $Re \gg \sqrt{3}e \approx 4.71$:

$$\overline{f_\sigma} = \frac{\sqrt[3]{2}}{3} \ln^{-2} \left(\frac{\exp(W_0(Re/\sqrt{3}))}{e} \right) = \frac{\sqrt[3]{2}/3}{[W_0(Re/\sqrt{3}) - 1]^2} \quad (35)$$

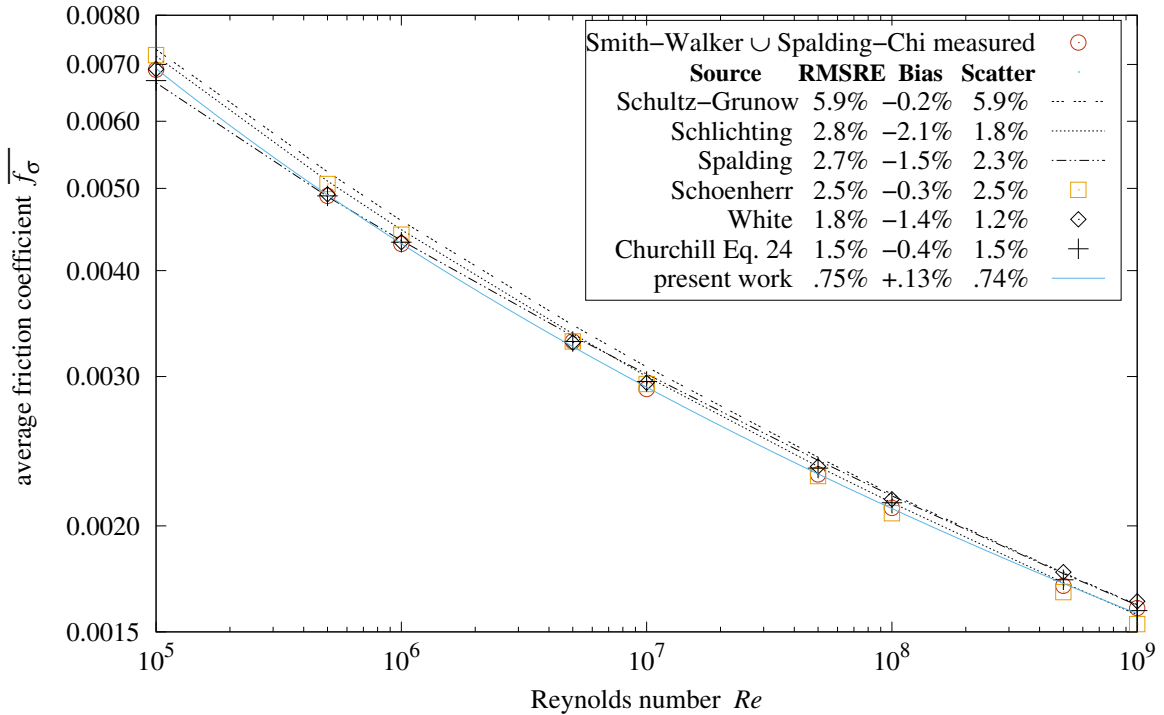


Figure 9 Average $\overline{f_\sigma}$ versus Re of smooth plate

6.3 Comparison With Measurements. Churchill [11] compared smooth turbulent friction formulas from multiple studies with measurements from Smith and Walker [16], and Spalding and Chi [17]. Figure 9 plots them and $\overline{f_\sigma}$ formula (35); the key gives the RMS error of the measurements relative to each formula (RMSRE was introduced in Section 2).

- With 0.75% RMSRE, $\overline{f_\sigma}$ formula (35) has less error than any formula evaluated by Churchill.

7. Spectral Roughness

Several prior works [4, 5, 6, 8, 12] use the term “uniform roughness” to describe sand-roughness, implying that its height-of-roughness is the same at all scales. This concept of uniform roughness is incompatible with self-similarity; the RMS height-of-roughness of a portion of a self-similar surface must shrink with its succession of scales.

Sand-roughness can be described as “repeated roughness”. However, a roughness composed of parallel rows of 1000 sand grains spanning its length can also be described as having 500 sand grain pairs spanning its length. Needed is an unambiguous method for determining the spatial period.

7.1 Discrete Fourier Transform. The discrete Fourier transform (36) converts a series of equally-spaced samples of a function into a complex-number coefficient X_j for each of its harmonic sinusoidal components:

$$X_j = \sum_{t=0}^{w-1} Y(t, w) \exp\left(\frac{-2\pi i j t}{w}\right) \quad (36)$$

A complex number consists of two real numbers as $a + bi$, where $i = \sqrt{-1}$; b is called the imaginary part. The amplitude of $a + bi$, written $|a + bi| = \sqrt{a^2 + b^2}$.

There is a profound connection between X_j and the RMS height-of-roughness ϵ :

$$\epsilon = \sqrt{\frac{1}{w} \sum_{j=1}^{w-1} |X_j|^2} \quad (37)$$

$|X_{w-j}| = |X_j|$ because all the $Y(t, w)$ elevations have imaginary parts = 0; hence there are $w/2 + 1$ distinct $|X_j|$; only $0 \leq j \leq w/2$ needs to be considered in the developments which follow.

7.2 Dominant Component of Roughness. The $X_0 = \bar{z}$ term, the mean value of Y , is the only X_j term not included in the formula (37) sum for ϵ . Hence, the dominant component of roughness will be the X_j ($0 < j \leq w/2$) having the largest amplitude.

- Let the “period index” j_P be the nonzero index j of the X_j having the largest amplitude $|X_j|$.
- When one $|X_j|$ is dominant, j_P is well-defined and the profile roughness’s spatial period is $L_P = L/j_P$.

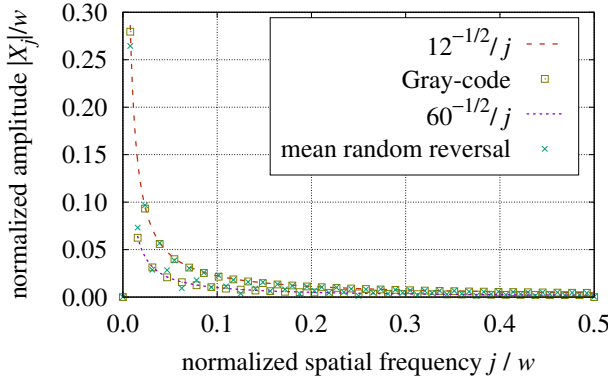


Figure 10 Gray and random spectra

Figure 10 shows the $|X_j|/w$ amplitude spectrum of the Gray-code profile roughness from Figure 3; also the mean Fourier spectrum amplitudes from 187 instances of 128-point random reversal profiles ($w = 128$). For both spectra, X_1 has the largest amplitude; thus $j_P = 1$, indicating that neither spectrum is from repeated roughness.

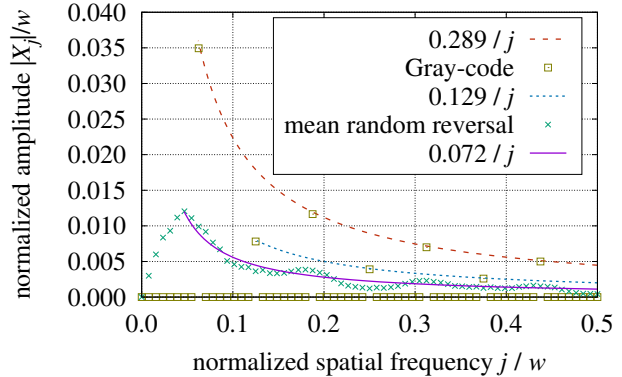


Figure 11 Gray and random eighths

Figure 11 shows the spectrum of eight concatenated repetitions of a Gray-code sequence; also the mean Fourier spectrum amplitudes from 187 instances of eight concatenated random reversal sequences. The period index j_P of the Gray-code eighths is 8, as expected; but the random reversal sequences have $j_P = 6$ because their amplitudes are not correlated between the random eighths.

- This use of the discrete Fourier transform was able to determine the spatial period of profile roughness. The next section generalizes this spatial period metric to isotropic surface roughness.

8. Periodic Roughness

- Let a “periodic roughness” be a flat surface tiled with many isotropic, uniformly sized patches, all sharing the same mean elevation \bar{z} and RMS height-of-roughness ε .
- The mean elevation and RMS height-of-roughness of the entire surface will therefore be \bar{z} and ε .

8.1 Discrete Spatial Fourier Transform. Let $S_{s,t}$ be a $w \times w$ matrix of mean elevations from a $w \times w$ square grid of an $L_w \times L_w$ region of a rough surface. Its 2-dimensional discrete spatial Fourier transform is:

$$X_{j,k} = \sum_{t=0}^{w-1} \sum_{s=0}^{w-1} S_{s,t} \exp\left(-2\pi i \frac{j t + k s}{w}\right) \quad (38)$$

- Let the 2-dimensional period index $j_P = \sqrt{j^2 + k^2} > 0$, where $0 \leq j \leq w/2$ and $0 \leq k \leq w/2$ are the indexes of the coefficient $X_{j,k}$ having the largest amplitude, excluding $X_{0,0}$.
- The 2-dimensional spatial period $L_P = L_w/j_P$.

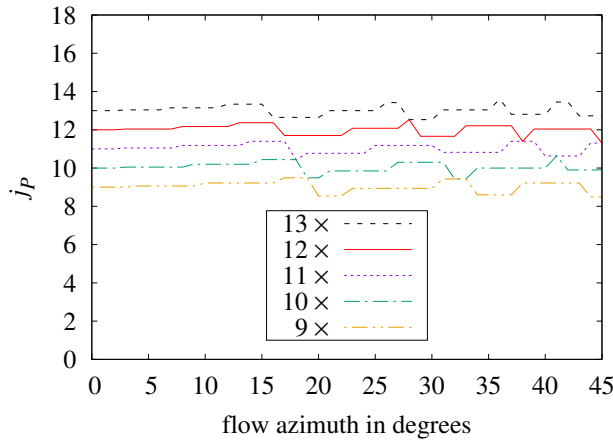


Figure 12 Bi-level plate 50%

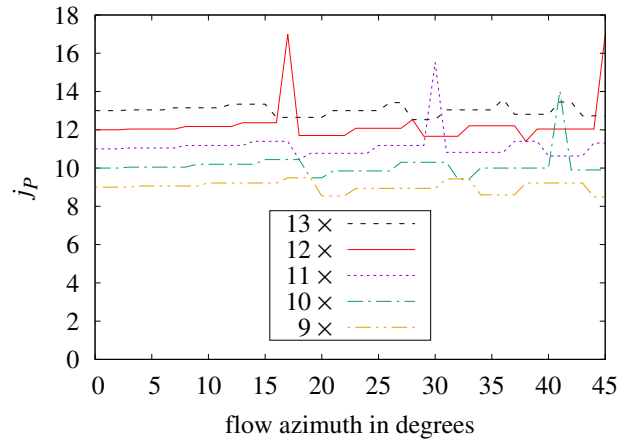


Figure 13 Bi-level plate 25%

Figure 12 shows the j_P values of a square equal-area bi-level surface (regular array of square posts on a flat plate) computing $X_{j,k}$ from a 64×64 interpolated sampling of that surface with azimuth from 0° through 45° , and which is scaled between 9 and 13 cells per side. At each scale, j_P varies within a ± 1 range as the azimuth is rotated. Figure 13 shows j_P values of a 25% high, 75% low, bi-level surface; some of its j_P traces have peaks outside of the ± 1 range. This suggests a quantitative criterion for surface roughness isotropy:

- A surface roughness is isotropic if $j_P \gg 1$ varies no more than ± 2 through its full flow azimuth rotation.
- More specifically, using $w \times w$ ($w \geq 64$) samplings of roughness at nine scales over a 2:1 range such that most of the calculated j_P values satisfy $8 \leq j_P \leq 16$ at each scale, do 56 sampling trials with randomized offset and randomized azimuth rotation per scale. A roughness is considered isotropic if no more than 5 of the $504 (= 56 \times 9)$ trials have j_P varying more than $\pm w/32$ from its scale.

8.2 Exploring Isotropy. Tests of this criterion applied to 128×128 interpolated samplings found the following roughnesses to be isotropic:

- square arrays of aligned square posts having an upper area fraction between 27% and 76%;
- square arrays of circular columns having an upper area fraction between 24% and 78%;
- hexagonal arrays of circular columns having an upper area fraction between 6% and 75%;
- hexagonal arrays of circular wells (depressions) having an upper area fraction between 25% and 94%;
- hexagonal arrays of aligned square posts having an upper area fraction between 4% and 49%;
- hexagonal arrays of aligned square wells having an upper area fraction between 51% and 96%;
- 15% elongated hexagonal arrays of cone or bump protrusions described in Schlichting [5].

8.3 Visual Isotropy. This isotropy test is not equivalent to the visual appearance of isotropy. Square

post arrays having upper area fractions of 20% fail the isotropy test, while those with 30% pass. Plates from Schlichting [5] having elongated hexagonal arrays of cones are not visually isotropic, yet pass the test.

9. Onset of Rough Turbulence

For an isotropic, periodic roughness with $0 < \varepsilon < L_P \ll L$, there must be some value $Re_\lambda > 0$ such that when $0 < Re < Re_\lambda$, there is only laminar or smooth turbulent fluid flow along the plate.

The boundary-layer is thinnest at the leading edge. For isotropic, periodic roughness, any disruption will start within the leading band ($0 < x < L_P$) of roughness. This investigation considers a boundary-layer disrupted when $\varepsilon > \delta_2(L_P)$, where $\delta_2(x)$ is the boundary-layer momentum thickness at x .

9.1 Momentum Thickness. $\delta_2(x)$ is the thickness of bulk flow having the same momentum flow rate as the plate's boundary-layer at x . δ_2 is not directly measurable. Schlichting [9] gives the momentum thickness of laminar and smooth turbulent boundary-layers as formulas (39) and (40), respectively:

$$\delta_{2\lambda}(x) = \frac{0.664 x}{Re_x^{1/2}} = 0.664 \sqrt{Re_x} \frac{L}{Re} \quad (39)$$

$$\delta_{2\sigma}(x) = \frac{0.036 x}{Re_x^{1/5}} = 0.036 Re_x^{4/5} \frac{L}{Re} \quad (40)$$

Laminar $\delta_{2\lambda}$ derives from the compelling Blasius boundary-layer model. Smooth turbulent $\delta_{2\sigma}$ is less certain.

Momentum thickness $\delta_2(x)$ is a local property of the fluid flow. In order to work locally with Re_ε formula (30), change $L \rightarrow x$ and $Re \rightarrow Re_x$; then solve $Re_\varepsilon = 1$ for x/ε :

$$\frac{Re_x}{\sqrt{3}} = \frac{x}{\varepsilon} \ln \frac{x}{\varepsilon} \quad \frac{x}{\varepsilon} = \exp\left(W_0\left(\frac{Re_x}{\sqrt{3}}\right)\right) \quad (41)$$

Re_x is proportional to x ($Re_x \propto x$); hence, the smooth turbulent momentum thickness $\delta_2(x)$ should be proportional to the product of x and u_τ/u formula (26). Eliminating x/ε using formula (41):

$$\delta_2(x) \propto \frac{x}{\sqrt{3} \ln(x/\varepsilon)} = \frac{x}{\sqrt{3} W_0(Re_x/\sqrt{3})} \quad (42)$$

The proposed formula (43) coefficient is $1/3^3 \approx 0.0370$, which may relate to $\varphi^\varphi \equiv \exp(\varphi \ln \varphi)$.

$$\delta_2(x) = \frac{x}{3^3 W_0(Re_x/\sqrt{3})} \quad (43)$$

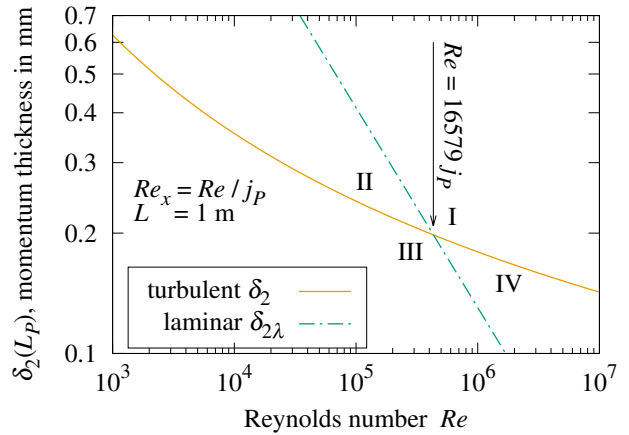
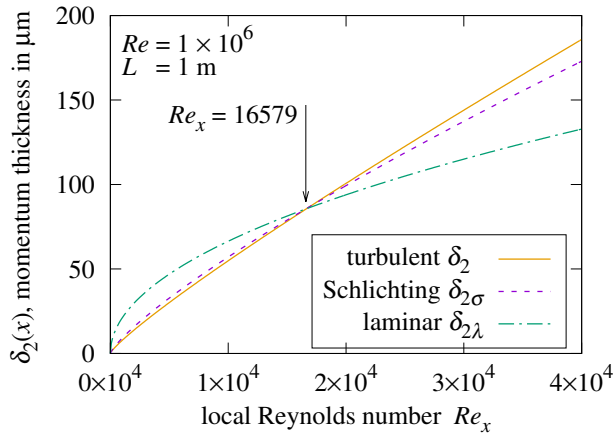


Figure 14 Smooth plate $\delta_2(x)$ versus Re_x **Figure 15** Smooth plate $\delta_2(L_P)$ versus Re

Figure 14 demonstrates that (smooth) “turbulent δ_2 ” formula (43) and “Schlichting $\delta_{2\sigma}$ ” formula (40) nearly match between the origin and the intersection of the laminar and turbulent curves at:

$$Re_x = \left[\frac{0.664}{0.036}\right]^{10/3} \approx 16579 \quad (44)$$

- Thus, $\delta_{2\sigma}(L_P)$ is a reasonable approximation for $\delta_2(L_P)$ in the leading band of roughness.

9.2 Flow Mode Re Bounds. Figure 15 shows the leading band momentum thickness of laminar and smooth turbulent flows along a 1 m long plate versus Re . The intersecting laminar $\delta_{2\lambda}$ and smooth turbulent δ_2 curves partition the graph into four regions labeled I, II, III, and IV.

- When the point at coordinates $[Re, \varepsilon]$ is in region I, the roughness is sufficient to disrupt both laminar and smooth turbulent flow; hence, leading band fluid flow will be rough turbulent.
- When $[Re, \varepsilon]$ is in regions II or III, the roughness is not high enough to significantly disrupt laminar flow; hence, leading band fluid flow will be laminar, possibly transitioning to smooth turbulent.
- When $[Re, \varepsilon]$ is in region IV, the roughness would be sufficient to disrupt laminar flow, but not large enough to disrupt smooth turbulent flow; hence, leading band fluid flow would be smooth turbulent.

With $\delta_{2\lambda} = \varepsilon$ and $x = L_P$, solve formula (39) for the laminar upper-bound Re_λ :

$$Re_\lambda = \left[\frac{0.664}{\varepsilon} \right]^2 L_P L \quad (45)$$

With $x = L_P$ and $\delta_2(x) = \varepsilon$ in formula (43) with $Re \gg \sqrt{3}eL/L_P$:

$$W_0 \left(\frac{Re L_P}{\sqrt{3} L} \right) = \frac{L_P}{3^3 \varepsilon} \quad (46)$$

The inverse of $\varphi = W_0(\vartheta)$ is $\vartheta = \varphi \exp \varphi$. Solving for the smooth turbulent upper-bound $Re_\sigma = Re$:

$$Re_\sigma = \frac{\sqrt{3} L}{3^3 \varepsilon} \exp \frac{L_P}{3^3 \varepsilon} \quad (47)$$

Equating Re_λ and Re_σ yields their intercept (found numerically) at $L_P/\varepsilon \approx 194.3$.

The combination of $L_P/\varepsilon > 194.3$ and $L \gg L_P$ required by region IV operation will be rare; $Re_\sigma < Re_\lambda$ will hold for nearly all isotropic, periodic roughnesses.

10. Plateau Roughness

Distinct flow mode regions can form along plates whose roughness peaks are all co-planar (at the same elevation) plateaus. With $Re > \max(Re_\sigma, Re_\lambda)$ producing rough turbulence in the leading band of the plate, smooth turbulence occurs downstream from where $\delta_2(x)$ is large enough to bridge the gaps. The drag from the downstream portion of the surface will be proportional to $\overline{f_\sigma}$, not the constant $\overline{f_\rho}$ of rough turbulence.

Informally, a “plateau roughness” is an isotropic, periodic roughness with most of its area at its peak elevation. Of particular interest are plateau roughnesses where each cell contains a single continuous plateau area whose boundary has a convex perimeter within the cell. This will either be an array of “islands” whose tops are all co-planar, or an array of “wells” dropping below an otherwise flat plane.

10.1 Plateau Islands. Consider a smooth flat plate etched with a square grid of grooves subjected to a $Re > \max(Re_\sigma, Re_\lambda)$ flow. When the boundary-layer is disrupted by a groove perpendicular to the flow, the smooth turbulent boundary-layer restarts at the leading edge of the next island. At the scale of the roughness period L_P , the momentum thickness of the boundary-layer grows from 0 to nearly the L -scale $\delta_2(x)$ value (depending on the size of the island). If δ_2 grows to exceed ε , then the rest of the plate (to its trailing edge) will have a smooth turbulent friction coefficient proportional to $\overline{f_\sigma}$ with characteristic length L_P .

Along isotropic roughness, the growth of δ_2 depends on plateau size, but not on orientation. An isotropic size metric is needed. In natural convection from an upward-facing horizontal plate [26, 27], the (isotropic) characteristic length metric $L^* = A^*/p^*$, where A^* is the convex region’s area and p^* is its perimeter length. For a regular polygon or circle, $L^* = r/2$, where r is the minimum radius of the regular polygon or circle.

In order to find the island Re_x threshold Re_I , multiply both sides of equation (43) by $3^3 Re / [\sqrt{3} L]$. This allows Re_x to be isolated using the Lambert W_0 function identity $\varphi/W_0(\varphi) = \exp W_0(\varphi)$:

$$\frac{3^3 Re}{\sqrt{3} L} \delta_2 = \exp W_0 \left(\frac{Re_x}{\sqrt{3}} \right) \quad (48)$$

The boundary-layer thickness needed to bridge the gap grows with ε and shrinks with increasing L^* , suggesting $\delta_2 = \varepsilon^2/L^*$. The Re strength needed to reach δ_2 thickness at $x = L_P$ grows strongly with L/L_P . Letting $Re = [L/L_P]^3$ in equation (48), then taking the logarithm of both sides:

$$\ln \frac{3^3 \varepsilon^2 L^2}{\sqrt{3} L^* L_P^3} = W_0 \left(\frac{Re_x}{\sqrt{3}} \right) \quad (49)$$

The inverse of $\varphi = W_0(\vartheta)$ is $\vartheta = \varphi \exp \varphi$. Solving formula (49) for $Re_I = Re_x$:

$$Re_I = \frac{3^3 \varepsilon^2 L^2}{L^* L_P^3} \ln \frac{3^3 \varepsilon^2 L^2}{\sqrt{3} L^* L_P^3} \quad \frac{[4 L^*]^2}{L_P^2} > \frac{1}{2} \quad (50)$$

With large enough gaps, the islands are too narrow to support smooth turbulence bridging the gaps, leading to the inequality in formula (50). Formula (50) is tested against two square-grooved plates in Section 18.

10.2 Plateau Wells. Laying a perforated sheet on a flat plate turns its holes into wells. $L^* = A^*/p^*$. Fluid is forced up after diving into a well; instead of $Re = [L/L_P]^3$ in formula (49), let $Re = L^3/[2 L_P]^3$, leading to the wells Re_x threshold Re_W :

$$Re_W = \frac{3^3 \varepsilon^2 L^2}{2^3 L^* L_P^3} \ln \frac{3^3 \varepsilon^2 L^2}{2^3 \sqrt{3} L^* L_P^3} \quad \frac{[4 L^*]^2}{L_P^2} < \frac{1}{2} \quad (51)$$

With large enough wells, the flats between them are too narrow to support smooth turbulence bridging the wells, leading to the inequality in formula (51). Formula (51) is tested with perforated sheets in Section 17.

10.3 Openness. Let “openness” $0 < \Omega < 1$ be the non-plateau area per cell area ratio; $1 - \Omega$ is thus the “upper area fraction” of Section 8. Let $S_{s,t}$ be a $w \times w$ matrix of elevations. The span of elevations accepted as plateau must be a length smaller than ε and decrease with increasing $[4 L^*]$, which suggests $\varepsilon^2/[4 L^*]$:

$$\Omega \approx \frac{1}{w^2} \sum_{t=0}^{w-1} \sum_{s=0}^{w-1} \begin{cases} 1, & \text{if } S_{s,t} < \max(S) - \varepsilon^2/[4 L^*]; \\ 0, & \text{otherwise.} \end{cases} \quad (52)$$

This allows a quantitative definition of plateau roughness:

- “Plateau roughness” is an isotropic, periodic roughness with $\Omega < 1/2$.

An isotropic, periodic roughness which is not plateau roughness disrupts nascent boundary layers every L_P , but lacks the flat peaks necessary for smooth turbulent layer growth. Thus, this investigation proposes:

- When $\Omega > 1/2$ and $Re > \max(Re_\sigma, Re_\lambda)$, flow along the entire surface will be rough turbulent.

Note that $\Omega < 1/2$ does not replace the inequalities (50, 51); it is an additional constraint. However, they are related by “circularity”.

10.4 Circularity. For island area A^* with perimeter p^* , circularity $o^* = 4 \pi A^*/p^{*2}$ takes its maximum value, 1, in disks; it is $\pi\sqrt{3}/6 \approx 0.907$ in hexagons, $\pi/4 \approx 0.785$ in squares, and $\pi\sqrt{3}/9 \approx 0.605$ in equilateral triangles. Similarly, for square cell area A with perimeter p , circularity $o = 4 \pi A/p^2$. Scaling by the circularity ratio derives $[4 L^*]^2/L_P^2$ from $[1 - \Omega]$.

$$[1 - \Omega] \frac{o^*}{o} = \frac{A^{*2}}{p^{*2}} \frac{p^2}{A_P^2} = \frac{[4 L^*]^2}{L_P^2} \quad (53)$$

Formula (53) is the same within a hexagonal cell, $A = \sqrt{3}/2 L_P^2$ and perimeter $p = 2 \sqrt{3} L_P$.

The plateau wells roughness formula simply replaces replaces $[1 - \Omega]$ with Ω :

$$\Omega \frac{o^*}{o} = \frac{A^{*2}}{p^{*2}} \frac{p^2}{A_P^2} = \frac{[4 L^*]^2}{L_P^2} \quad (54)$$

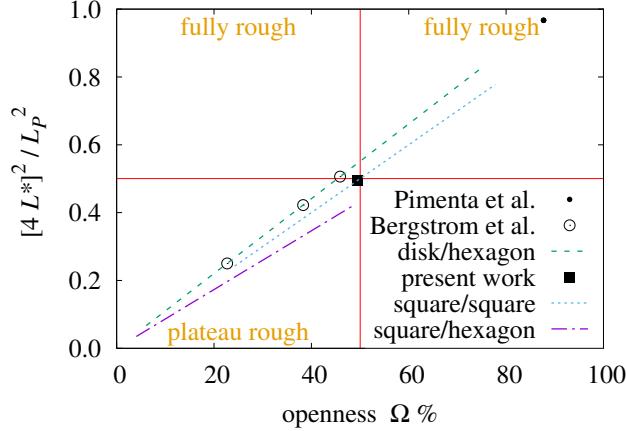


Figure 16 $[4L^*]^2/L_P^2$ versus Ω

The slope of each trace in Figure 16 is its o^*/o ratio. The “square/square” trace for a square array of square posts has slope 1. The “disk/hexagon” trace for a hexagonal array of circular wells has slope $\sqrt{12}/\pi \approx 1.1$. The “square/hexagon” trace for a hexagonal array of square posts has slope $\sqrt{3}/2 \approx 0.87$. Each trace spans the bounds for that bi-level configuration discovered in Section 8.

Also plotted are the Ω values of experiments by Pimenta et al. [7], Bergstrom et al. [14], and this investigation. The experiments of Sections 16, 17, and 18 find friction and convection consistent with the type of flow named in three of the quadrants. The lower right quadrant would be reached when the convex region circularity is less than the cell circularity. But Section 8 found that such bi-level surfaces did not qualify as isotropic, periodic roughness when $\Omega > 1/2$. The Pimenta et al. plate was not bi-level roughness.

- This experimental data locates the $[4L^*]^2/L_P^2$ threshold between 0.495 and 0.506.

11. Local Skin-Friction Coefficients

Conversions between local and average skin-friction are needed in order to compare prior with present work.

11.1 Continuous Local to Average Skin-Friction. The ratio of average to local skin-friction $\overline{f_c}/f_c > 1$ of a continuous boundary-layer is calculated from f_c by formula (55). Using $Re_0 > 0$ as the integration lower-bound avoids the division-by-zero singularity at the leading edge of the plate.

$$\frac{\overline{f_c}(Re)}{f_c(Re)} = \frac{1}{Re - Re_0} \int_{Re_0}^{Re} \frac{f_c(Re_x)}{f_c(Re)} dRe_x \quad (55)$$

The Blasius laminar model in Schlichting [9] derives the local drag coefficient:

$$f_\lambda = \frac{0.664}{\sqrt{Re_x}} \quad (56)$$

Applying transform (55) to formula (56) and factoring the denominator produces a novel formula for the average laminar friction coefficient which lacks the leading-edge singularity:

$$\overline{f_\lambda}(Re) = 1.328 \frac{\sqrt{Re} - \sqrt{Re_0}}{Re - Re_0} = \frac{1.328}{\sqrt{Re} + \sqrt{Re_0}} \quad (57)$$

Lienhard and Lienhard [15] estimates $Re_0 = 600$, leading to $\overline{f_\lambda}(0) \approx 0.0542$.

11.2 Disrupted Local to Average Skin-Friction. The local skin-friction coefficient is not well-defined for self-similar roughness because of its constant L/ε . Periodic roughness has varying L/ε ; conveniently, it also provides L_P/ε as the lower-bound of integration.

A crucial distinction between periodic roughness and smooth surfaces is that periodic roughness disrupts the boundary-layer repeatedly. Thus, the local skin-friction coefficients being averaged are independent. Instead of $\overline{f_\rho}/f_\rho$ scaling linearly, it should scale as the square:

$$\frac{\overline{f_\rho}(L/\varepsilon)}{f_\rho(L/\varepsilon)} = \left[\frac{\varepsilon}{L - L_P} \int_{L_P/\varepsilon}^{L/\varepsilon} \frac{f_\rho(r)}{f_\rho(L/\varepsilon)} dr \right]^2 \quad (58)$$

Applying formula (58) to the Mills-Hang local formula (9) yields the average skin-friction coefficient:

$$\overline{C_f}^2 / C_f \quad (59)$$

where C_f and $\overline{C_f}$ are from equations (9) and (10), respectively.

11.3 Disrupted Average to Local Skin-Friction. For disrupted boundary-layers, the transform for local friction f_ρ given average friction $\overline{f_\rho}$ is:

$$\frac{f_\rho(L/\varepsilon)}{\overline{f_\rho}(L/\varepsilon)} = \left[\frac{d([L - L_P] \overline{f_\rho}(L/\varepsilon))}{dL} \bigg/ \overline{f_\rho}(L/\varepsilon) \right]^2 \quad (60)$$

Applying formula (60) to $\overline{f_\rho}$ formula (29) with $L \geq x > L_P \geq \varepsilon$ yields the local friction coefficient:

$$f_\rho(x/\varepsilon) = \frac{1}{3} \left[\frac{\ln(x/\varepsilon) + 2[L_P/x - 1]}{\ln^2(x/\varepsilon)} \right]^2 \quad (61)$$

11.4 Continuous Average to Local Skin-Friction. For continuous boundary-layers, the transform for local friction f_c given average friction $\overline{f_c}$ is:

$$\frac{f_c(Re_x)}{\overline{f_c}(Re)} = \frac{1}{\overline{f_c}(Re)} \frac{d([Re_x - Re_0] \overline{f_c}(Re_x))}{dRe_x} \quad (62)$$

The local skin-friction coefficient for smooth turbulent flow f_σ can be derived from $\overline{f_\sigma}$ equation (35), formula (62), and W_0 identity (63), provided that $Re_x \geq Re_0 \geq \sqrt{3}e$ and $Re_x \gg \sqrt{3}e$:

$$\frac{dW_0(\vartheta)}{d\vartheta} \equiv \frac{W_0(\vartheta)}{\vartheta [W_0(\vartheta) + 1]} \quad (63)$$

$$f_\sigma(Re_x) = \frac{W_0^2(Re_x/\sqrt{3}) - 2[1 - Re_0/Re_x] W_0(Re_x/\sqrt{3}) - 1}{[W_0(Re_x/\sqrt{3}) - 1]^3 [W_0(Re_x/\sqrt{3}) + 1]} \quad (64)$$

Table 4 Local smooth turbulent performance

Source	RMSRE	Bias	Scatter
Schultz-Grunow	8.5%	+5.5%	6.6%
White	4.2%	-2.9%	3.0%
Von Karman	3.7%	+0.7%	3.6%
Schlichting	3.6%	-2.4%	2.7%
Spalding	3.4%	-2.5%	2.3%
Churchill Eq. 16	3.0%	-2.3%	2.0%
present work	1.9%	+1.2%	1.4%
Churchill Eq. 18	1.3%	+0.6%	1.2%

11.5 Comparison With Local Measurements. Table 4 compares measurements at $10^5 \leq Re_x \leq 10^{10}$ made by Smith and Walker [16] and Spalding and Chi [17] with “present work” formula (64) and formulas collected by Churchill [11].

When calculating RMSRE, the error due to variation in a single sample tends to be larger than the error when that variation is distributed among multiple samples. Thus, local measurements tend to have larger RMSRE than average measurements do. Other than “Churchill Eq. 18”, this is the case when comparing Table 4 with Figure 9.

- The Churchill local data-set has 1.9% RMSRE versus “present work” formula (64).

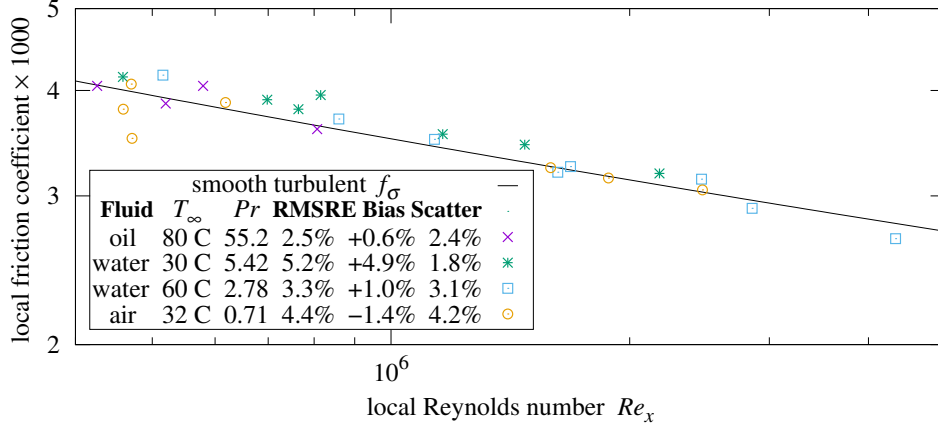


Figure 17 Local f_σ versus Re_x of smooth plate

11.6 Skin-Friction in Liquids. Figure 17 compares f_σ formula (64) with skin-friction measurements in several fluids from Žukauskas and Šlančiauskas [18].

A fluid’s Prandtl number (Pr) is its kinetic viscosity per thermal diffusivity ratio. Fluids with $Pr \gg 1$ transport heat primarily via fluid flow; conduction dominates heat transfer in fluids with $Pr \ll 1$.

- These data-sets have 2.5%-5.2% RMSRE versus “present work” formula (64).
- No significant dependence on Pr is manifest.

12. Forced Convection

Forced convective heat transfer is expressed as the (dimensionless) average Nusselt number $\overline{Nu} \equiv \overline{h} L/k$, where k is the fluid’s thermal conductivity ($W/(m \cdot K)$) and \overline{h} is the plate’s average convective surface conductance in that fluid ($W/(m^2 \cdot K)$). The local version, $Nu \equiv h x/k$, has the same units.

12.1 Rough Plate. Rough turbulence, and hence its heat transfer, grow with $Re \overline{f}_\rho(Re)$. Jaffer [28] finds that the natural convection boundary layer of an upward-facing plate is disrupted by collision of the flows and their detachment from the plate’s center; the other plate orientations have continuous boundary layers. Boundary layer disruption being the essence of rough turbulence, this investigation proposes that heat transfer also grows with the same $\sqrt[3]{Pr}$ dependence as upward-facing natural convection.

Fluid heating by the leading part of the plate reduces heat transfer from the trailing part; hence, convection is scaled by 1/2. Expanding \overline{f}_ρ from equation (29) yields formula (65) for rough turbulent average forced convection, provided that $L/\varepsilon \gg 1$ and $Pr \geq 0$:

$$\overline{Nu}_\rho = \frac{Re \overline{f}_\rho Pr^{1/3}}{2} = \frac{Re Pr^{1/3}}{6 \ln^2(L/\varepsilon)} \quad (65)$$

The present analysis for self-similar \overline{f}_ρ did not involve continuous boundary-layers; hence, it avoids the $Pr \geq 0.6$ restriction affecting formula (66). Formula (65) is compared with measurements in Section 18.

12.2 Smooth Plate. For smooth turbulent convection, Lienhard [29] recommends composing the Gnielinski formula (66) with the White smooth formula (12) as C_σ , subject to $Pr \geq 0.6$:

$$Nu = \frac{Re_x Pr C_\sigma/2}{1 + 12.7 [Pr^{2/3} - 1] \sqrt{C_\sigma/2}} \quad (66)$$

Lienhard states that Nu formula (67) has similar accuracy for gases with $0.6 \leq Pr < 2$:

$$Nu = 0.0296 Re_x^{4/5} Pr^{0.6} \quad (67)$$

$$\overline{Nu} = 0.037 Re^{4/5} Pr^{0.6} \quad (68)$$

Smooth plate forced convection is similar to natural convection from a vertical plate; in both, fluid flows parallel to the plate’s characteristic length axis, and is uniform across the plate’s other axis. Jaffer [28]

finds that stationary fluid conducts heat from the vertical plate with an effective Nusselt number $Nu_0 = 2^4/[\pi^2 \sqrt[4]{2}] \approx 1.363$; it is a coefficient factor of both the static and flow-induced heat transfer terms.

Flow-induced heat transfer grows with $Nu_0 Re \overline{f_\sigma}$. Because this heat traverses boundary-layers, the Pr dependence is more complex than $Pr^{1/3}$. In Jaffer [28], the vertical-plate natural convection dependence is $\sqrt[3]{Pr/\Xi(Pr)}$, where $\Xi(Pr)$ is defined using ℓ^p -norm (discussed in Section 13) formula (69) with $p = \sqrt{1/3}$:

$$\|\varphi, \vartheta\|_p \equiv [|\varphi|^p + |\vartheta|^p]^{1/p} \quad (69)$$

$$\Xi(Pr) = \left\| 1, \frac{0.5}{Pr} \right\|_{\sqrt{1/3}} \quad (70)$$

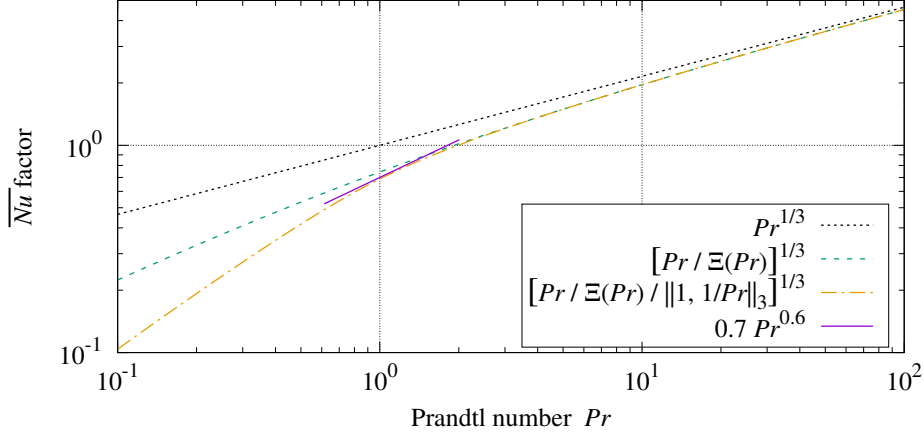


Figure 18 Smooth plate $\overline{Nu_\sigma}$ dependence on Pr

In Figure 18, $\sqrt[3]{Pr/\Xi(Pr)}$ is asymptotically $Pr^{1/3}$ at large Pr , and $\sqrt[3]{2} Pr^{2/3}$ at small Pr . At small Pr , conduction does not amplify forced convection as it does for natural convection; the Pr exponent should be 1. An additional factor using the ℓ^3 -norm accomplishes this. Formula (71) is asymptotically $\sqrt[3]{2} Pr$ when $Pr \ll 0.5$. The “ $0.7 Pr^{0.6}$ ” trace shows that formula (71) has a slope close to formulas (67) and (68) for gases.

$$\sqrt[3]{\frac{Pr}{\Xi(Pr)}} \sqrt[3]{\frac{1}{\|1, 1/Pr\|_3}} \quad (71)$$

The slope of formula (66) $Nu(C_\sigma)$ decreases with increasing Pr ; at large Pr , $Nu \propto \sqrt{C_\sigma}$. Recall from equations (27) and (28) that $\overline{f_c} \propto u_\tau^2$; hence $\sqrt{\overline{f_c}} \propto u_\tau$. This indicates that transport through the boundary-layer restricts convection at large Pr . In order to reduce the asymptotic dependence from $\overline{f_\sigma}$ to $\sqrt{\overline{f_\sigma}}$, the convection formula will include a factor which takes the square-root of an expression gating $\overline{f_\sigma}$ by Pr :

$$\sqrt{\frac{Pr/\sqrt{162} + 1}{\sqrt{162} Pr \overline{f_\sigma} + 1}} \quad \sqrt{162} \equiv 9\sqrt{2} \approx 12.7 \quad (72)$$

The scaling for upstream heating was $1/2$ in $\overline{Nu_\rho}$ formula (65) for disruptive roughness; the smooth turbulent boundary-layer reduces this interaction; $\sqrt{1/3} \approx 0.577$ appears correct in the smooth case.

- Formula (73) is proposed for smooth turbulent convection for all $Pr \geq 0$ and $Re \gg \sqrt{3}e$:

$$\overline{Nu_\sigma} = \frac{Nu_0 Re \overline{f_\sigma}}{\sqrt{3}} \sqrt{\frac{Pr/\sqrt{162} + 1}{\sqrt{162} Pr \overline{f_\sigma} + 1}} \sqrt[3]{\frac{Pr/\Xi(Pr)}{\|1, 1/Pr\|_3}} \quad (73)$$

12.3 Performance. Section 14 compares $\overline{Nu_\sigma}$ formula (73) with measurements over a wide range of Pr .

Lienhard [29] compares the Gnielinski-White convection formula with local measurements from studies of fluids with $0.7 \leq Pr \leq 257$ spanning $4000 < Re_x < 4.3 \times 10^6$. The smallest turbulent Re_x was $\approx 10^5$. Gas formula (67) is more accurate than Gnielinski-White for turbulent air ($Pr \approx 0.71$) at $Re_x < 10^5$.

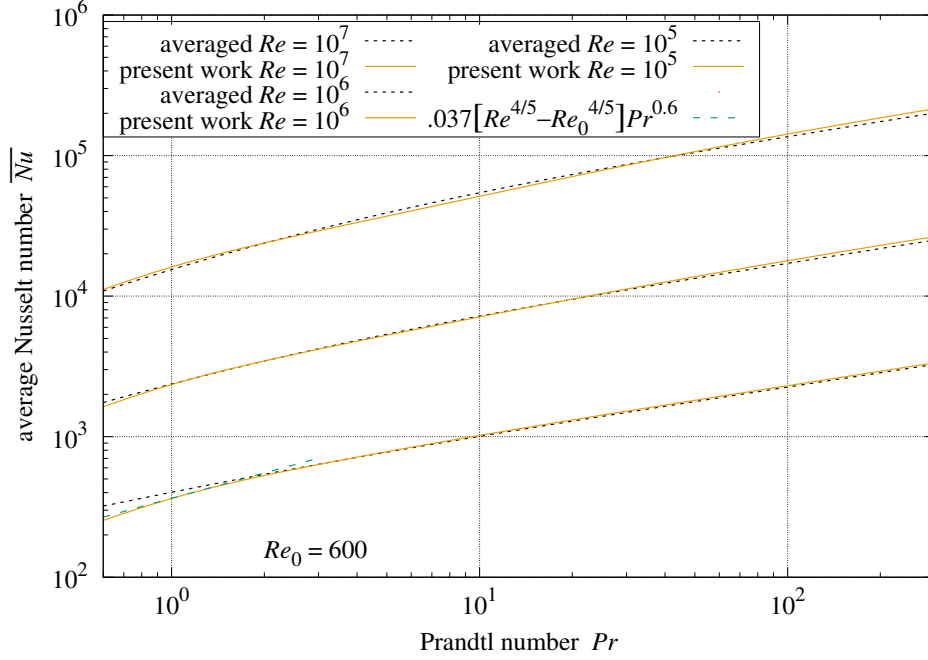


Figure 19 Smooth plate average turbulent convection versus Pr by Re

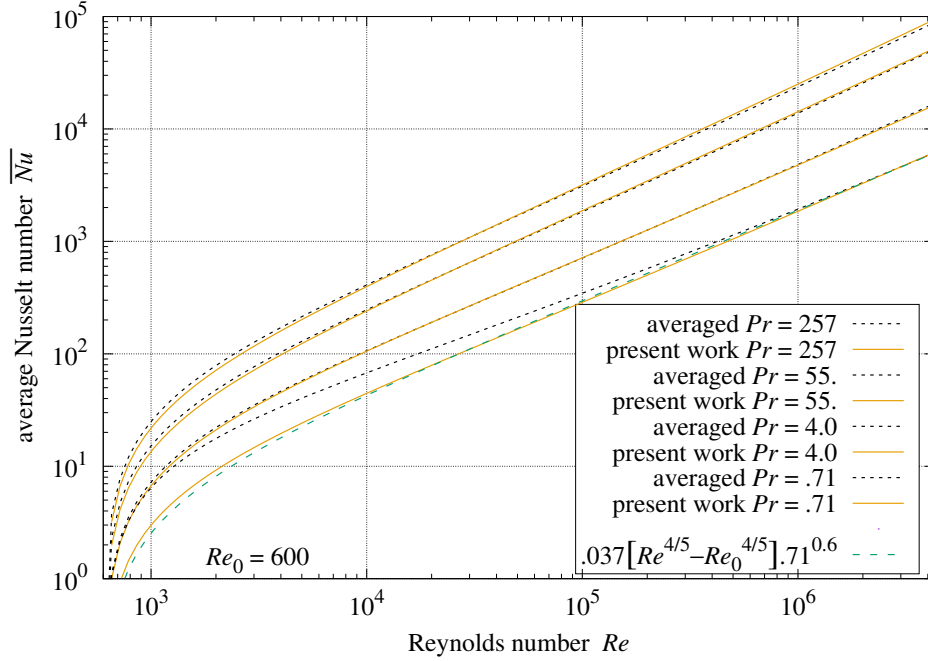


Figure 20 Smooth plate average turbulent convection versus Re by Pr

Figures 19 and 20 show \overline{Nu}_σ versus Pr and Re , respectively. The “present work” traces are formula (73). The “averaged” traces use formula (74) to numerically average the composition of the Gnielinski formula (66) with the White formula (12).

$$\overline{Nu}_\sigma(Re) = \int_{Re_0}^{Re} \frac{Nu_\sigma(Re_x)}{Re_x} dRe_x \quad (74)$$

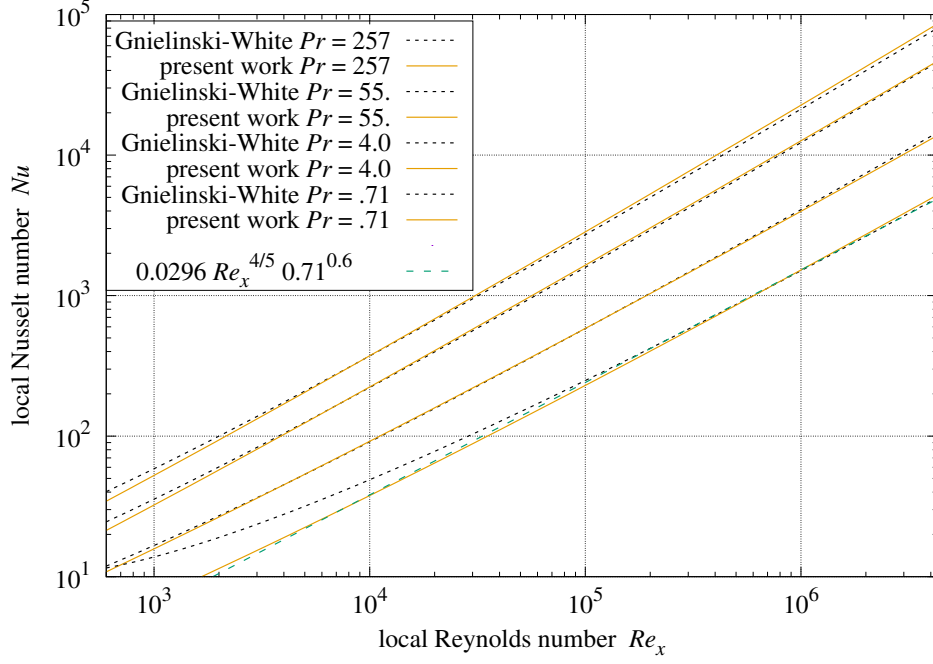


Figure 21 Smooth plate local turbulent convection

Figure 21 shows Gnielinski formula (66) and local convection Nu_σ formula (75) versus Re_x .

$$Nu_\sigma(Re_x) = Re_x \frac{d\overline{Nu_\sigma}(Re_x)}{dRe_x} \quad (75)$$

- $\overline{Nu_\sigma}$ formula (73) matches the numerically averaged Gnielinski-White formula within $\pm 6.6\%$ over the range $10^5 < Re < 4.3 \times 10^6$ with $4.0 \leq Pr \leq 257$.
- At $Pr = 0.71$, $\overline{Nu_\sigma}$ matches gases formula (68) within $\pm 4\%$ over the range $10^4 < Re < 4.3 \times 10^6$.
- Over the same ranges, local convection Nu_σ formula (75) matches formulas (66) and (67) within $\pm 7.1\%$.

12.4 Laminar Forced Convection. Formula (76) is the Reynolds-Colburn [30] analogy relating laminar friction to forced convective heat transfer. Applying it to $\overline{f_\lambda}$ formula (57), and scaling by the reduction in characteristic length due to an unheated starting band $x_u/L \equiv Re_u/Re$, yields the laminar forced convection formula (77) for $Re \geq 0$, $Pr \geq 0$, and $0 \leq x_u \ll L$.

$$\overline{Nu}(Re) = \overline{f_c}(Re) Re Pr^{1/3} / 2 \quad (76)$$

$$\overline{Nu_\lambda}(Re) = \frac{0.664 Re Pr^{1/3}}{\sqrt{Re} + \sqrt{Re_0}} \left\{ 1 - \left\| 1, \frac{x_u}{L} \right\|_{-2} \right\} \quad (77)$$

- Section 14 tests $\overline{Nu_\sigma}$ formula (73) and $\overline{Nu_\lambda}$ formula (77) extensively.

13. Combining Transfer Processes

This unnamed form appears frequently in heat transfer formulas:

$$F^p(\xi) = F_0^p(\xi) + F_\infty^p(\xi) \quad (78)$$

Churchill and Usagi [31] stated that such formulas are “remarkably successful in correlating rates of transfer for processes which vary uniformly between these limiting cases.” Convection and skin-friction are transfer processes. Convection transfers heat; skin-friction drag ($\propto Re f_c$) transfers momentum.

13.1 The ℓ^p -norm. Requiring $F_0(\xi) \geq 0$ and $F_\infty(\xi) \geq 0$, and taking the p th root of both sides of equation (78) yields a vector-space functional form known as the ℓ^p -norm, which is notated $\|F_0, F_\infty\|_p$:

$$\|F_0, F_\infty\|_p = [|F_0|^p + |F_\infty|^p]^{1/p} \quad (79)$$

Norms generalize the notion of distance. Formally, a vector-space norm obeys the triangle inequality: $\|y, z\|_p \leq \|y\|_p + \|z\|_p$, which holds only for $p \geq 1$. The present work finds $p < 1$ useful as well.

Let $y \geq 0$ and $z \geq 0$. When $p > 1$, the processes compete and $\|y, z\|_p \geq \max(y, z)$; the most competitive is $\|y, z\|_{+\infty} \equiv \max(y, z)$. The ℓ^2 -norm is equivalent to root-sum-squared; it models perpendicular competitive processes such as forced and natural convection from the present apparatus plate sides in formula (113).

The ℓ^1 -norm models independent processes; $\|y, z\|_1 \equiv y + z$. It appears in formulas (87, 88, 89).

When $0 < p < 1$, the processes cooperate and $\|y, z\|_p \geq y + z$. Cooperation between conduction and flow-induced heat transfer uses the $\ell^{1/2}$ -norm in natural convection ([28]). Formula (70) uses the $\ell^{\sqrt{1/3}}$ -norm from natural convection in forced convection.

When $p < 0$, $\|y, z\|_p \leq \min(y, z)$, with the transition sharpness controlled by p ; the extreme is $\|y, z\|_{-\infty} \equiv \min(y, z)$. Negative p can model a single flow through serial processes; the most restrictive process limits the flow. The ℓ^{-1} -norm appears in the critical Re_c formulas (101) and (102). The ℓ^{-2} -norm appears in the unheated starting length term of formula (77), and in fan-speed formula (109). The ℓ^{-4} -norm appears in laminar-turbulent transition formulas (82, 83, 86, 88, 89).

13.2 Turbulent Flow Modes. Isotropic, periodic surfaces with $Re_\sigma < Re_\lambda$ and $\Omega > 1/2$ shed the rough turbulence of formulas (29, 61, 65) when $Re > Re_\lambda$. Plateau roughness ($\Omega < 1/2$) sheds either smooth or rough turbulence, or a combination. Table 5 proposes the behaviors of plateau islands and plateau wells roughnesses. If the $[4L^*]^2/L_P^2$ condition is not satisfied, then the Re_x conditions split the plate at distance x from the leading edge into regions operating in different modes. Formula (50) is the islands threshold Re_I ; formula (51) is the wells threshold Re_W .

Table 5 Turbulent flow modes for plateau roughness

Islands condition	Plateau islands	Wells condition	Plateau wells
$[4L^*]^2/L_P^2 < 1/2$	rough formulas (29, 61, 65)	$[4L^*]^2/L_P^2 > 1/2$	rough formulas (29, 61, 65)
$Re_x < Re_I$	rough formulas (29, 61, 65)	$Re_x < Re_W$	blend formula (84)
$Re_x > Re_I$	smooth formulas (80, 81)	$Re_x > Re_W$	smooth formula (85)

13.3 Plateau Islands. The “ $Re_x > Re_I$ ” flow mode is smooth turbulence with characteristic length L_P . The island’s plateau area is augmented by 1/2 of the non-plateau area and an area which grows with ε , combined using the ℓ^2 -norm because ε and L_P are perpendicular:

$$\overline{f_I} = \left\{ 1 - \Omega + \left\| \frac{\Omega}{2}, \frac{2\varepsilon[4L^*]}{L_P^2} \right\|_2 \right\} \frac{L}{L_P} \overline{f_\sigma} \left(\frac{Re L_P}{L} \right) \quad (80)$$

$$\overline{Nu_I} = \left\{ 1 - \Omega + \left\| \frac{\Omega}{2}, \frac{2\varepsilon[4L^*]}{L_P^2} \right\|_2 \right\} \frac{L}{L_P} \overline{Nu_\sigma} \left(\frac{Re L_P}{L} \right) \quad (81)$$

$\overline{f_\rho}$ and $\overline{Nu_\rho}$ are active at $Re_x < Re_I$; $\overline{f_I}$ and $\overline{Nu_I}$ are active at $Re_x > Re_I$. The $\|Re, Re_I\|_{-4}$ term transitions between these parts gradually in formulas (82, 83). The $[\|Re, Re_I\|_{-4}/Re]$ factor normalizes the characteristic length in formula (82).

$$\overline{f_c} = \overline{f_I}(Re) + [\|Re, Re_I\|_{-4}/Re] \{ \overline{f_\rho} - \overline{f_I}(\|Re, Re_I\|_{-4}) \} \quad (82)$$

$$\overline{Nu}_\ell = \overline{Nu}_I(Re) + \overline{Nu}_\rho(\|Re, Re_I\|_{-4}) - \overline{Nu}_I(\|Re, Re_I\|_{-4}) \quad (83)$$

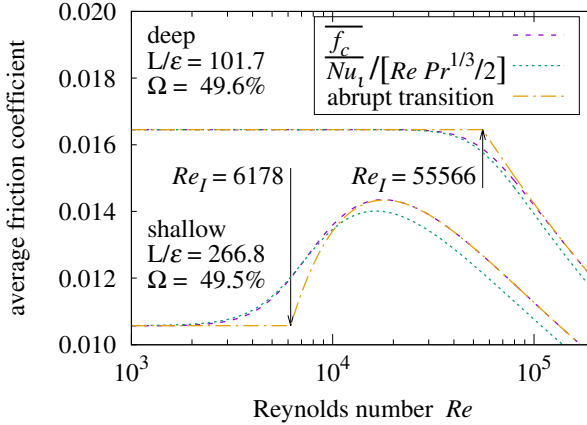


Figure 22 Plateau islands friction

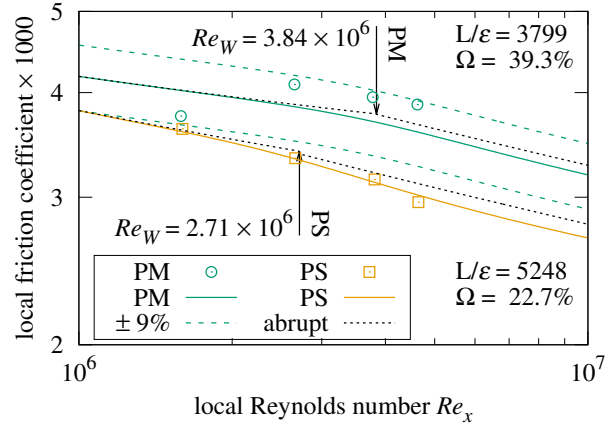


Figure 23 Plateau wells friction

Figure 22 shows that \overline{Nu} and $\overline{f_c}$ are closely related in gases. Section 18 compares convection measurements from two bi-level plates with \overline{Nu}_ℓ formula (83).

13.4 Plateau Wells. In “blend” mode, the plateau sheds smooth turbulence while its wells are in rough turbulence. The effective friction coefficient is the area-proportional blend:

$$f_\beta = \Omega \overline{f_\rho}(L/\varepsilon) + [1 - \Omega] f_\sigma(Re) \quad (84)$$

Where $Re_x > Re_W$, the friction is smooth turbulent, but with additional area $2\pi\varepsilon[4L^*]$. The well walls are perpendicular to the plateau, but only a portion of each well wall is parallel to the flow, which must divert to brush by both. A strength between $\ell^{\sqrt{2}}$ and ℓ^2 is needed; their geometric mean is $p = \sqrt[4]{8} \approx 1.682$:

$$f_W = \left\| 1, 2\pi\varepsilon[4L^*]/L_P^2 \right\|_{\sqrt[4]{8}} f_\sigma(Re) \quad (85)$$

f_β is active at $Re_x < Re_W$; f_W is active at $Re_x > Re_W$:

$$f_W(Re) + [\|Re, Re_W\|_{-4}/Re] \{ f_\beta(\|Re, Re_W\|_{-4}) - f_W(\|Re, Re_W\|_{-4}) \} \quad (86)$$

The $Re_x = Re_W$ plane can split wells; thus the transition between f_β and f_W flows must be gradual in formula (86). With the ℓ^{-4} -norm, the PM $\pm 9\%$ (expected uncertainty) curves in Figure 23 bound the PM measurements from Bergstrom et al. [14]; the ℓ^{-2} -norm does not. Section 17 compares local friction measurements of perforated sheets with formulas (85, 86).

13.5 Staged-Transition. When laminar and smooth turbulent flow occupy distinct plate regions separated at Re_c , their transfers combine using the ℓ^1 -norm (addition). An abrupt transition at Re_c would behave as formula (87). In practice, staged-transitions are not abrupt, behaving as the ℓ^{-4} -norm in formulas (88, 89). The subscript 4 is used to identify staged-transition formulas.

$$\left\| \frac{Re'}{Re} \overline{f_\lambda}(Re'), \overline{f_\sigma}(Re) - \frac{Re'}{Re} \overline{f_\sigma}(Re') \right\|_1 \quad Re' = \min(Re, Re_c) \quad (87)$$

$$\overline{f_4} = \left\| \frac{Re'}{Re} \overline{f_\lambda}(Re'), \overline{f_\sigma}(Re) - \frac{Re'}{Re} \overline{f_\sigma}(Re') \right\|_1 \quad Re' = \|Re, Re_c\|_{-4} \quad (88)$$

$$\overline{Nu_4} = \left\| \overline{Nu}_\lambda(Re_4), \overline{Nu}_\sigma(Re) - \overline{Nu}_\sigma(Re_4) \right\|_1 \quad Re_4 = \|Re, \sqrt{2} Re_c\|_{-4} \quad (89)$$

Formula (89) models staged-transition convection. Convection’s positive slope versus friction’s negative slope requires scaling Re_c by $\sqrt{2}$ so that the lower edge of the transition is at Re_c .

14. Smoothness

Schlichting [9] describes the behavior of parallel flow of “low turbulence intensity” along a sharp-edged, smooth surface as a “stable laminar flow following the leading edge”, transitioning to a “fully developed turbulent boundary-layer” at some $Re_x < 5 \times 10^5$. Flow along a silicon wafer should behave this way. However, a silicon wafer is an isotropic, periodic roughness with $L_P = 543$ nm and $\varepsilon = 31.2$ nm.

The amount of laminar flow displaced by a periodic roughness grows with both ε and L_P . Dimensional analysis suggests that this displacement is significant when $Re > L/\sqrt{\varepsilon L_P}$. However, Section 9 proposed that smooth turbulence is disrupted when $Re > Re_\sigma$, leading to a proposed criterion:

- An isotropic, periodic roughness behaves as a “smooth” surface when $L/\sqrt{\varepsilon L_P} > Re_\sigma$ and $Re < Re_\lambda$.
- When $L/\sqrt{\varepsilon L_P} < Re_\sigma$, the purely laminar upper-bound (critical Re) $Re_c = L/\sqrt{\varepsilon L_P}$.

The “silicon wafer” has $L/\sqrt{\varepsilon L_P} > Re_\sigma$ in Table 6; it should behave as a smooth surface when $Re < Re_\lambda$.

Table 6 Dimensionless surface parameters

Surface	L/ε	$L/\sqrt{\varepsilon L_P}$	Re_σ	Re_λ
silicon wafer	9.8×10^6	$2.3 \times 10^6 >$	$1.2 \times 10^6 \ll$	7.5×10^7
[7] Pimenta et al.	1.5×10^4	$5.0 \times 10^3 >$	$1.3 \times 10^3 \ll$	5.5×10^4
duck tape	7.5×10^3	$1.0 \times 10^3 <$	$4.0 \times 10^3 \ll$	1.9×10^5
[14] Bergstrom et al. PS	4.6×10^3	$1.5 \times 10^3 >$	$4.3 \times 10^2 \ll$	2.0×10^4
[14] Bergstrom et al. PM	3.0×10^3	$1.3 \times 10^3 >$	$2.3 \times 10^2 \ll$	7.2×10^3
[14] Bergstrom et al. PL	2.9×10^3	$1.2 \times 10^3 >$	$2.3 \times 10^2 \ll$	8.0×10^3
[14] Bergstrom et al. WMS	3.0×10^3	$1.5 \times 10^3 >$	$2.2 \times 10^2 \ll$	5.1×10^3
[14] Bergstrom et al. WMM	2.9×10^3	$1.5 \times 10^3 >$	$2.1 \times 10^2 \ll$	5.0×10^3
[14] Bergstrom et al. WML	1.6×10^3	$7.6 \times 10^2 >$	$1.2 \times 10^2 \ll$	3.3×10^3
present work 1 mm bi-level	2.9×10^2	$8.8 \times 10^1 >$	$2.9 \times 10^1 \ll$	1.5×10^3
present work 3 mm bi-level	1.0×10^2	$5.1 \times 10^1 >$	$7.5 \times 10^0 \ll$	1.8×10^2

14.1 Pierced-Laminar Flow. Consider “duck tape”, the only row in Table 6 with $L/\sqrt{\varepsilon L_P} < Re_\sigma$.

Tuck and Kouzoubov [32] finds that slow laminar flow over a periodic roughness “. . . represents a shift of the apparent plane boundary toward the flow domain.” At small Re , the flow from the apparent boundary plane outward is the same as smooth laminar flow.

Between the surface and its apparent boundary plane, shearing stress periodically (L_P) exceeds that of a smooth surface, spawning vortexes as Re increases, asymptotically approaching smooth turbulent flow. This investigation terms this mixture “pierced-laminar flow”; the laminar flow is pierced by vortexes.

14.2 Smooth Laminar Flow. Reducing free-stream turbulence to unusually low values, Schubauer and Skramstad [33] reported that “oscillations were discovered in the laminar boundary layer along a flat plate.” These periodic oscillations suggest that rough and smooth laminar flows both spawn vortexes periodically along the plate, controlled by the purely laminar upper-bound Re_c .

14.3 Laminar-Turbulent Mixing. The hypothesized periodic vortexes pierce the laminar boundary-layer. The present theory holds that the laminar component is active through the entire $Re < Re_\lambda$ range in pierced-laminar flow, resulting in friction formula (90) and convection formula (91).

$$\overline{f_c} = \left\| \overline{f_\lambda}(Re), \overline{f_\sigma}(Re) - \frac{Re_\gamma}{Re} \overline{f_\sigma}(Re_\gamma) \right\|_\gamma \quad Re_\gamma = \left\| Re, \frac{Re_c}{\sqrt{\gamma}} \right\|_{\gamma'} \quad (90)$$

$$\overline{Nu_c} = \left\| \overline{Nu_\lambda}(Re), \overline{Nu_\sigma}(Re) - \overline{Nu_\sigma} \left(\left\| Re, \sqrt{\gamma} Re_c \right\|_{\gamma'} \right) \right\|_\gamma \quad (91)$$

Because laminar and turbulent flows mix in pierced-laminar flow, the ℓ^1 -norm and ℓ^{-4} -norm of staged-transition formulas (88, 89) are replaced by the ℓ^γ -norm and $\ell^{\gamma'}$ -norm in formulas (90, 91). The laminar and turbulent flows are in mild competition, so $1 < \gamma < 2$. Figure 24 shows $\overline{f_c}$ formula (90) curves at $1 \leq \gamma \leq 2$ and $-8 \leq \gamma' \leq -4$. Smaller γ results in a sharper downward bend, while more negative γ' results in a sharper upward bend. Letting $\gamma' = -8/\gamma$ links the variables to sharpen the bends together within their respective ranges.

The geometric mean of 1 and 2 is $\sqrt{2}$; for the moment, assume $\gamma = \sqrt{2}$ and $\gamma' = 8/\gamma = 4\sqrt{2}$.

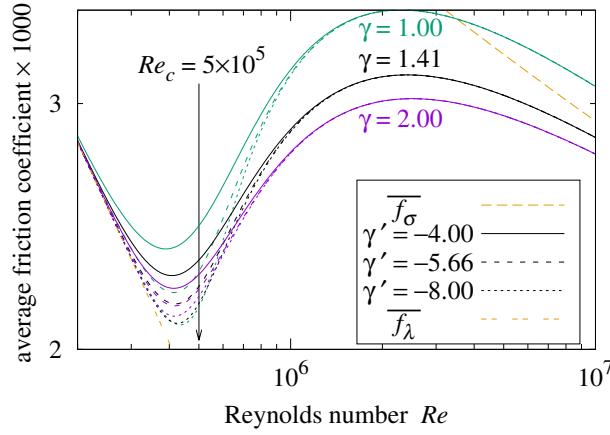


Figure 24 Pierced-laminar friction by γ, γ'

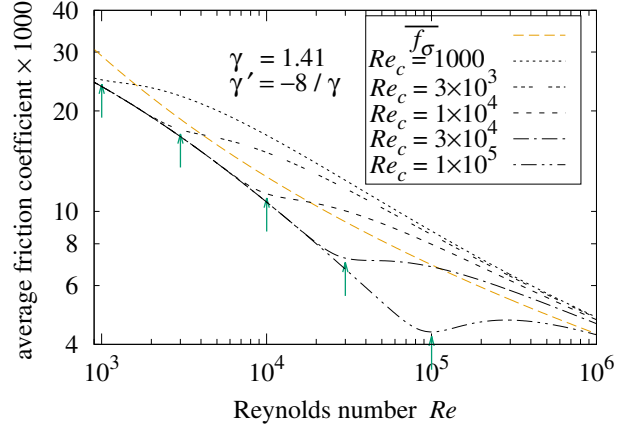


Figure 25 Pierced-laminar friction by Re_c

Figure 25 plots formula (90) at five Re_c values. Note that traces with smaller Re_c have larger friction coefficients than the smooth turbulent $\overline{f_\sigma}$ trace.

Figure 26 compares measurements from Gebers [19, 20] with staged-transition formula (88), pierced-laminar formula (90), and a formula from Schlichting [9] for an apparatus with $Re_c = 5 \times 10^5$:

$$0.455 / \log_{10}^{2.58} Re - 1700 / Re \quad (92)$$

- The Gebers [19, 20] measurements have 2.8% RMSRE from formula (90) with $Re_c = 5 \times 10^5$.

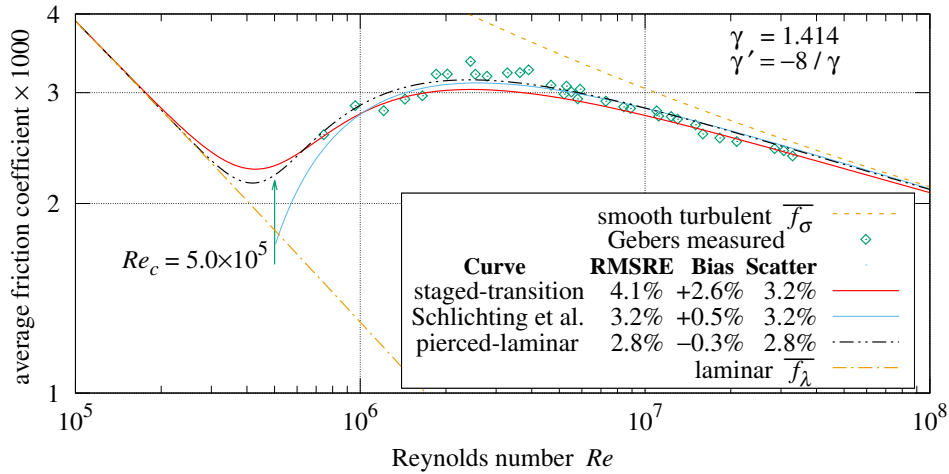


Figure 26 Average friction versus Re of smooth plate

Figure 27 shows that formula (91) $\overline{Nu_c} > \overline{Nu_\sigma}$ at small Re . Section 18 tests this property of formula (91).

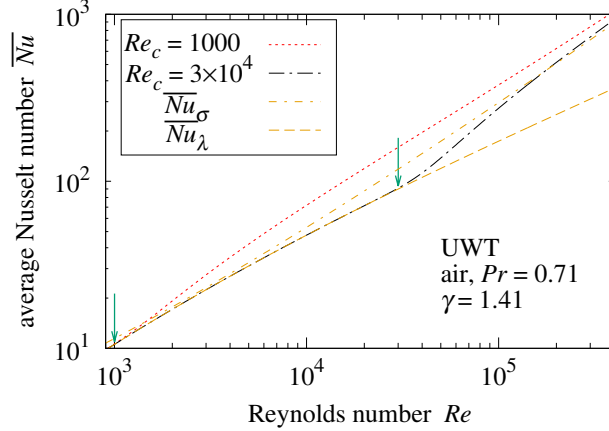


Figure 27 Convection critical transitions

14.4 **Local Skin-Friction and Convection.** Average-to-local transform (62) derives formulas (93) and (95) from formulas (88) and (90), with Re_c scaled by $\sqrt{2}$. Formulas (94) and (96) compute the local convections from the average convection formulas (89) and (91), with Re_c scaled by $\sqrt{\gamma}$. These Re_c scale factors are needed to make the local curve transitions align with Re_c .

$$f_4 = \frac{d[Re_x - Re_0] \overline{f_4}(Re_x, \sqrt{2} Re_c)}{dRe_x} \quad (93)$$

$$Nu_4 = Re_x \frac{d\overline{Nu_4}(Re_x, \sqrt{\gamma} Re_c)}{dRe_x} \quad (94)$$

$$f_c = \frac{d[Re_x - Re_0] \overline{f_c}(Re_x, \sqrt{2} Re_c)}{dRe_x} \quad (95)$$

$$Nu_c = Re_x \frac{d\overline{Nu_c}(Re_x, \sqrt{\gamma} Re_c)}{dRe_x} \quad (96)$$

14.5 **Convection Transition.** The Lienhard [29] comprehensive convection formula can be expressed using the ℓ^p -norm:

$$Nu(Re_x) = \left\| Nu_\lambda(Re_x), \left\{ \|Nu_\lambda(Re_c) [Re_x/Re_c]^c, Nu_\sigma(Re_x)\|_{-10} \right\} \right\|_5 \quad (97)$$

$$Nu_\lambda(Re_x) = 0.332 \sqrt{Re_x} Pr^{1/3} \left/ \sqrt[3]{1 - [Re_u/Re_x]^{3/4}} \right. \quad (98)$$

$$c = 0.9922 \log_{10} Re_c - 3.013 \quad (99)$$

Re_c is the critical Re_x upper-bound for purely laminar flow. Lienhard [29] states “The value of Re_c should be fit to the dataset, and the value of c may either be fitted or estimated from” formula (99). Lienhard curves in this investigation’s graphs use the c estimated by formula (99).

In the graphs which follow, the Re_c and c values fit by Lienhard [29] are marked with a star (*). The curves are computed and labeled with the Re_c value which minimizes the data-set RMSRE (relative to the formula) using the “Golden section search” algorithm from Kiefer [34].

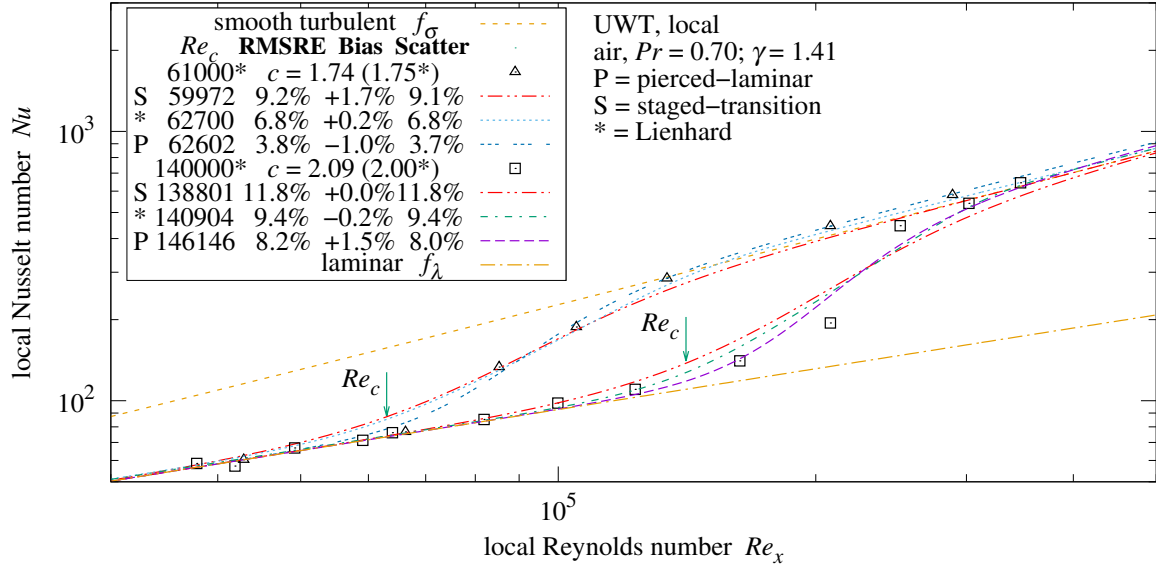


Figure 28 Kestin et al. [21] Local convection critical transition

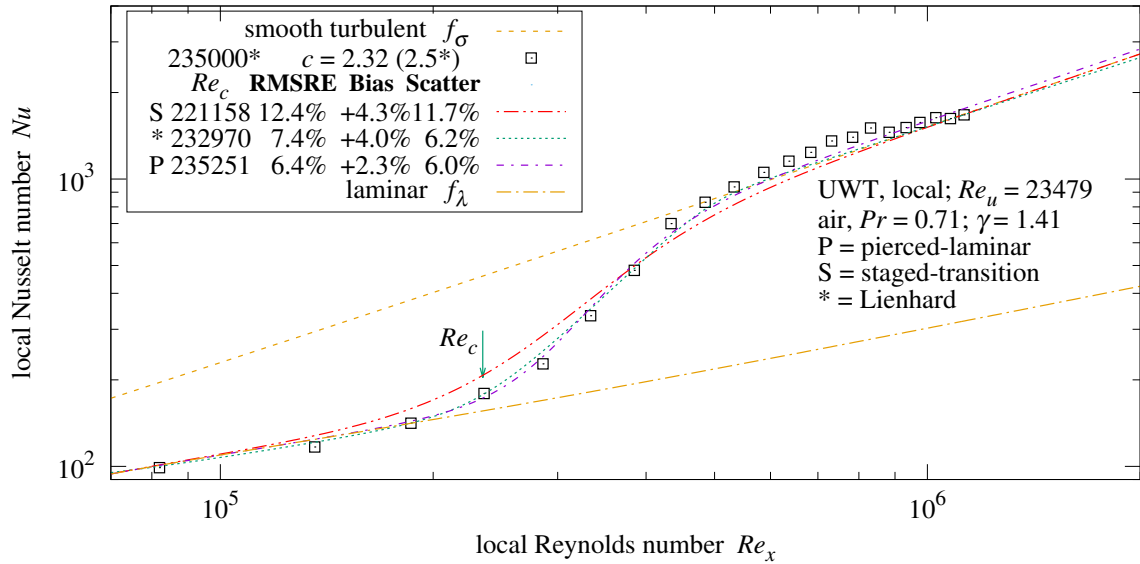


Figure 29 Reynolds et al. [22] Local convection critical transition

Figure 28 plots measurements from two Kestin, Maeder, and Wang [21] data-sets. Figure 29 plots data from Reynolds, Kays, and Kline [22] at $Pr = 0.70$ with unheated $Re_u = 23479$. Pierced-laminar formula (96) has the closest match (lowest RMSRE) to the measurements in Figures 28 and 29.

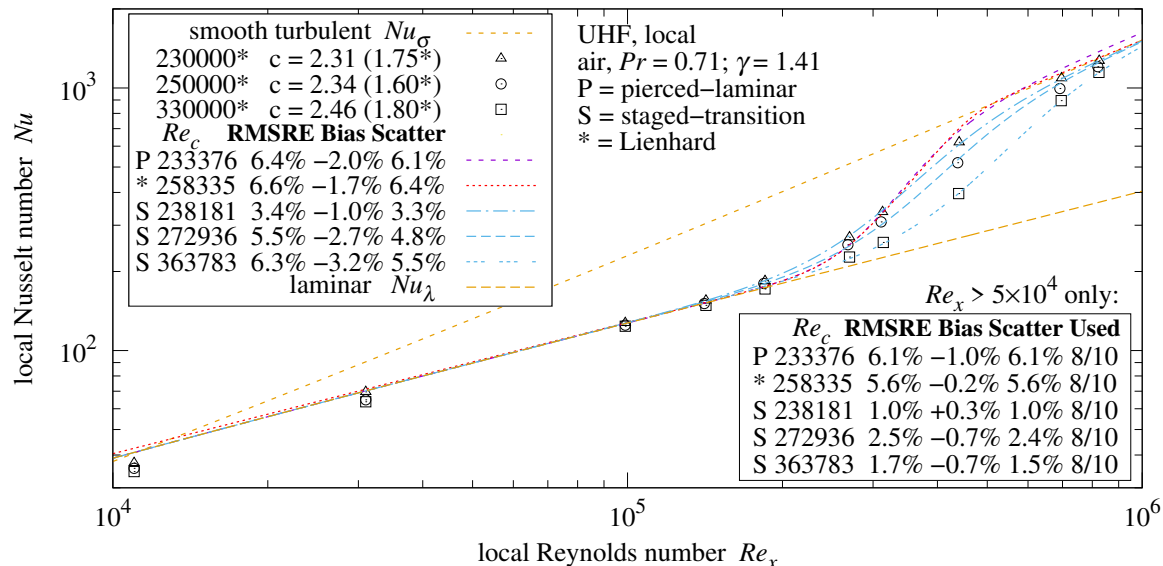


Figure 30 Žukauskas and Šlančiauskas [18] air critical transition

14.6 Uniform Heat Flux. Thus far, this investigation concerned uniform-wall-temperature (UWT, also termed “isothermal”) plates. Žukauskas and Šlančiauskas [18] measured critical transitions with a uniform-heat-flux (UHF) flowing through a smooth surface. In the present work, each convection graph is labeled UWT or UHF.

Per Lienhard [29], 0.4535 replaces 0.332 in Nu_λ formula (98) for UHF plates. Similarly, $0.4543/0.332 \approx 1.368$ scales \overline{Nu}_λ formula (77) when modeling UHF plates.

Lienhard [29] uses the Gnielinski smooth-turbulent formula (66) for both UWT and UHF plates. This investigation also applies its smooth-turbulent formula (73) to both UWT and UHF plates.

When a vortex transports fluid away from the surface of a UHF plate, the temperature of the fluid which replaces it increases more slowly than it would from a UWT plate. This reduction in local surface temperatures interferes with laminar heat transfer, largely restricting it to the $Re_x < Re_c$ region of the plate. Staged-transition formula (89) models convection from distinct laminar and turbulent areas, making it appropriate for UHF convection. Note that the fluid flow is the same; only its heat transfer is affected.

Figure 30 compares staged-transition formula (94), Lienhard formula (97), and pierced-laminar formula (96) with measurements by Žukauskas and Šlančiauskas [18] of UHF plates in air.

The two points of each Figure 30 data-set at $Re_x < 5 \times 10^4$ are far from the transition range of interest. Disregarding them reveals that the three data-sets match (S) staged-transition formula (94) with RMSRE less than 2.6%; the other formulas have more than twice this RMSRE.

- Pierced-laminar formula (96) matches UWT transitions more closely than formula (94).
- Staged-transition formula (94) matches UHF transitions more closely than formula (96).

Thus far, all the UWT transition data-sets have been in air at $Pr \approx 0.71$. Žukauskas and Šlančiauskas had $Pr > 1$ transition data-sets measured from UHF plates. How are UWT and UHF behaviors related?

Staged-transition and pierced-laminar convection will not coincide at $Re_x < Re_c$ because of their different laminar convection coefficients. Fluids with larger Pr will transport more heat away from the UHF plate’s warmer regions, reducing the temperature variations across the plate. Thus, UHF and UWT convection formulas should converge at large Pr and $Re > Re_c$.

- At $Re > 2^{1/4} Re_c$ the staged-transition curve is nearly identical to the pierced-laminar curve with $\gamma = 2$ and $\gamma' = -8/\gamma = -4$ in Figure 31. Therefore, convection γ varies with Pr , and $\lim_{Pr \rightarrow \infty} \gamma(Pr) = 2$.
- Comparison of pierced-laminar curves with convection measurements from Kestin et al. [21] in Figure 28 and Reynolds et al. [22] in Figure 29 establishes that $\gamma(0.71) \approx 1.41$.
- Mild competition between laminar and turbulent flows suggests $\lim_{Pr \rightarrow 0} \gamma(Pr) = 1$.

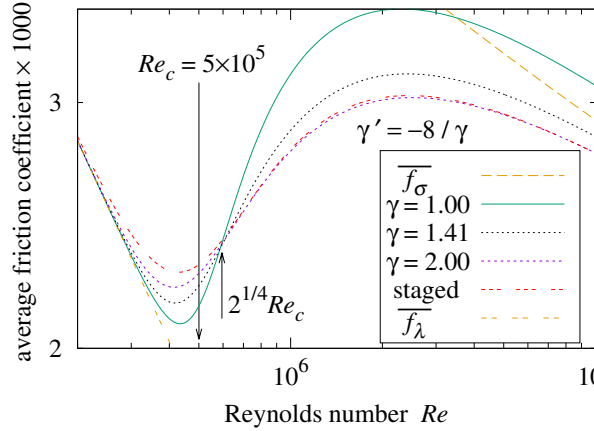


Figure 31 Pierced and staged friction

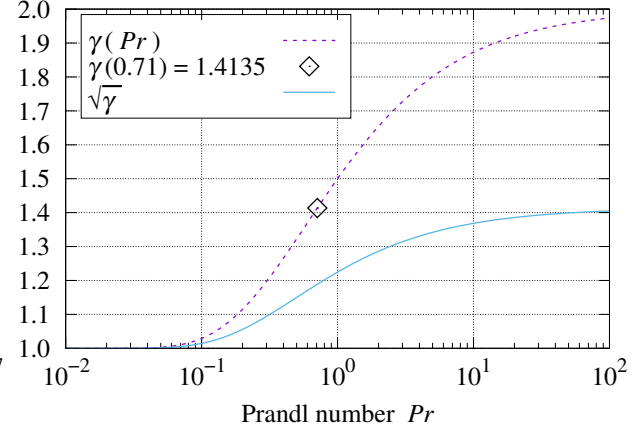


Figure 32 $\gamma(Pr)$ and $\sqrt{\gamma}$

- Figure 32 graphs proposed formula (100), which satisfies these three constraints.

$$\gamma(Pr) = 1 + \exp_2 \left(-Pr^{-\sqrt{1/2}} \right) \quad \exp_2(\varphi) \equiv 2^\varphi \quad (100)$$

Note that γ and γ' are Pr dependent only in convection. Graphing friction coefficient instead of convection in Figure 31 isolates the ℓ^p -norms from the effects of Pr on laminar and turbulent convection.

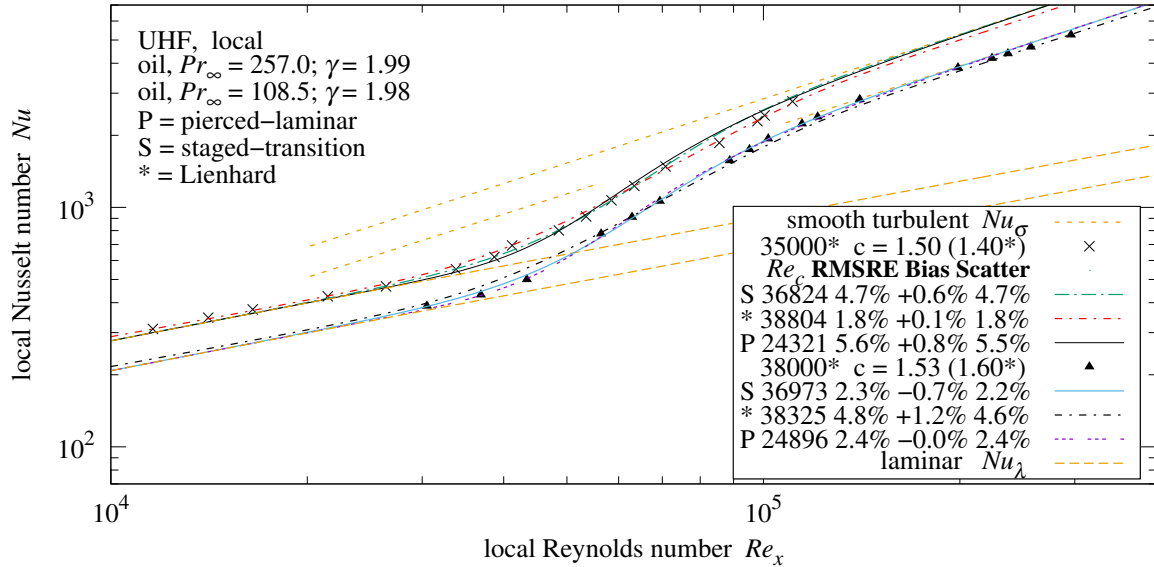


Figure 33 Žukauskas and Šlančiauskas [18] oil critical transition

14.7 Viscous Liquids. Žukauskas and Šlančiauskas [18] measured critical transitions in liquid water and transformer oil. The Pr of those fluids is sensitive to temperature. They recommended scaling the bulk fluid Pr_∞ by $\sqrt[4]{Pr_w/Pr_\infty}$ to yield $Pr = Pr_w^{1/4} Pr_\infty^{3/4}$, where Pr_w is at plate temperature. In the presence of vortices, the surface temperature of a UHF plate is not well-defined; this investigation treats UHF $Pr = Pr_\infty$. Žukauskas and Šlančiauskas [18] also scaled their UHF Nu measurements by $\sqrt[4]{Pr_\infty/Pr_w}$; the UHF data presented here is descaled.

Figures 33 and 34 compare Lienhard formula (97), pierced-laminar formula (96), and staged-transition formula (94) with UHF transition measurements in $Pr > 1$ fluids by Žukauskas and Šlančiauskas [18]. Lienhard formula (97) has 1.8% RMSRE on the $Pr_\infty = 257$ data-set in Figure 33, but larger RMSRE than staged-transition formula (94) on the other data-sets.

- With Re_c optimized to minimize RMSRE (at $Pr = Pr_\infty$), the Žukauskas and Šlančiauskas [18] UHF data-sets align to staged-transition formula (94) with RMSRE less than 4.8%.

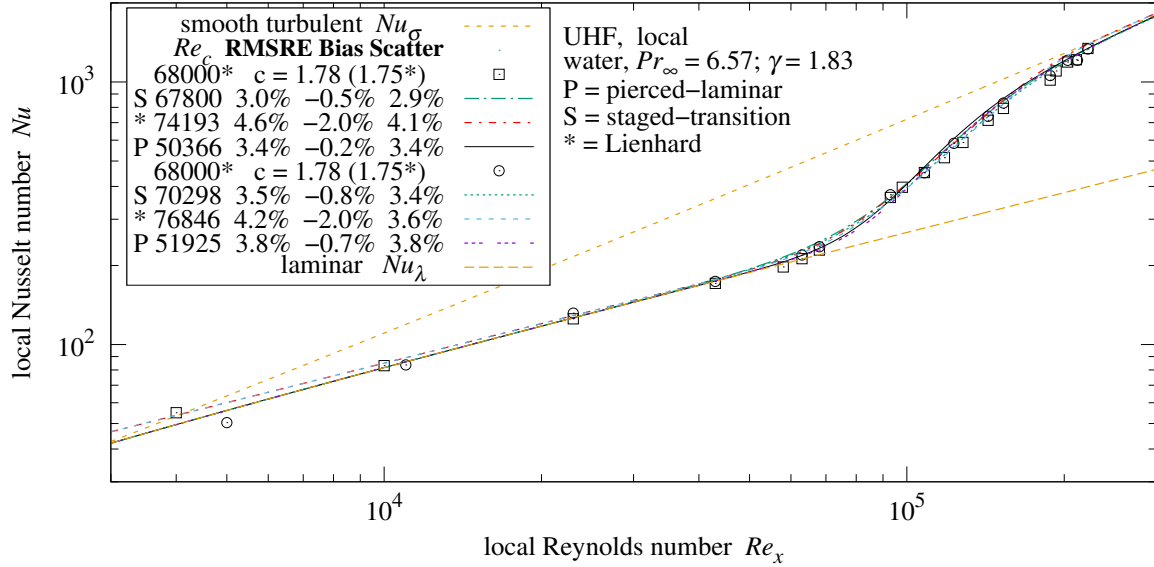


Figure 34 Žukauskas and Šlančiauskas [18] water critical transition

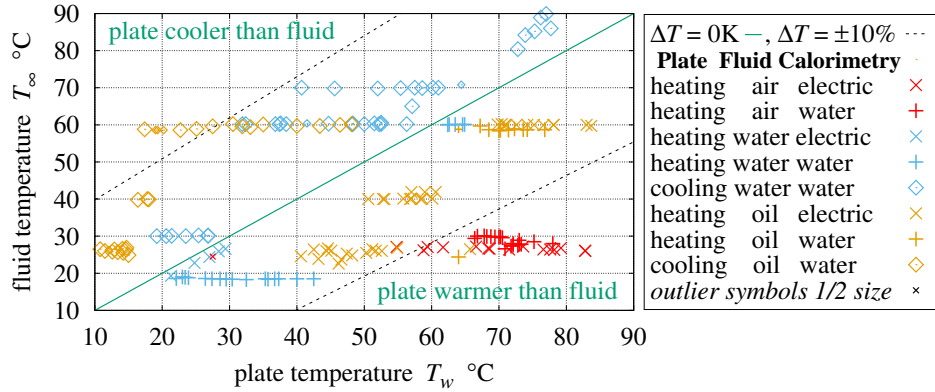


Figure 35 UWT plate-fluid temperature pairs

14.8 **UWT at Large Temperature Differences.** Thus far, the convection measurements have all been local. Žukauskas and Šlančiauskas [18] also measured average UWT heat transfer in air and liquids at the wide variety of fluid and plate temperatures paired in Figure 35. Testing both cooling and heating plates, this is a rigorous but challenging set of measurements because T_∞ , T_w , and Re are independent parameters. Adding to that challenge, $|T_w - T_\infty|/T > 10\%$ for many measurements in the UWT data-sets.

While this investigation uses $Pr = Pr_\infty$ for UHF plates, for UWT plates it uses $Pr = Pr_w^{1/4} Pr_\infty^{3/4}$ (which Žukauskas and Šlančiauskas [18] recommended for both types).

In the large temperature difference data-sets which follow, the numerically averaged version of Lienhard's comprehensive formula (97) had RMSRE values exceeding 10%; they are not tabulated here.

14.9 **Air.** Žukauskas and Šlančiauskas [18] contains a table of fluid properties by temperature. However the air properties were for dry air, as shown in Figure 36. The monthly average relative humidity (RH) in Kaunas, Lithuania, where the experiments were likely performed, varies between 70% and 90%. Section 25 details the humid-air model assembled from formulas in Kadoya, Matsunaga and Nagashima [35], Wexler [36], Tsilingiris [37], and Morvay and Gvozdenac [38]. The large relative errors in Figure 37 shows that the Žukauskas and Šlančiauskas [18] fluid table is inconsistent with 80% RH at air pressure $P = 100725$ Pa.

Using the humid air model at 80% relative humidity, Figure 38 shows the air data-sets versus smooth turbulent \bar{Nu}_σ and pierced-laminar \bar{Nu}_c . A single measurement excluded as an outlier is represented as a half-sized symbol. Figure 35 also represents outliers with half-sized symbols.

These measurements were obtained from plates incorporating either an electric heater or a water-based calorimeter in a separate apparatus for each type of fluid. Žukauskas and Šlančiauskas [18] intended to

measure turbulent convection, not critical transitions in these UWT convection data-sets; most of the $Re > Re_c$. Thus, the Re_c value is fitted to each data-set or 600, whichever is greater.

14.10 Triggered Turbulence. In these tests, Žukauskas and Šlančiauskas [18] placed a roughness strip across the leading plate edge, asserting that the downstream flow was all (smooth) turbulent. But Figure 38 shows that \overline{Nu}_σ is significantly less than \overline{Nu}_c . At $Re > Re_c$, (staged-transition) $\overline{Nu}_4 < \overline{Nu}_\sigma$. This rules out \overline{Nu}_σ and \overline{Nu}_4 as explanations of Figure 38. While these measurements exceed both laminar and turbulent convection, pierced-laminar \overline{Nu}_c has RMSRE less than 4.3%.

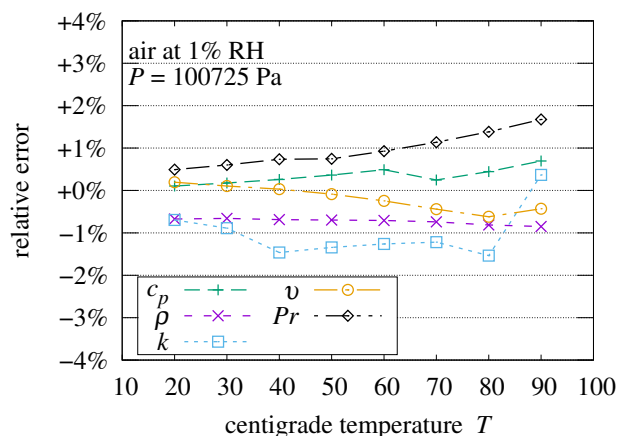


Figure 36 Air property fits at 1% RH

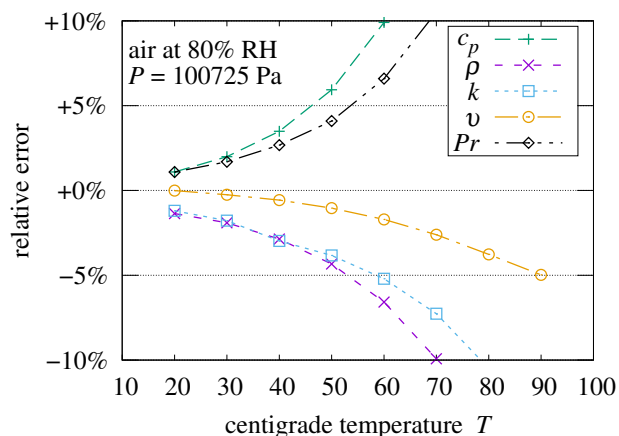


Figure 37 Air property fits at 80% RH

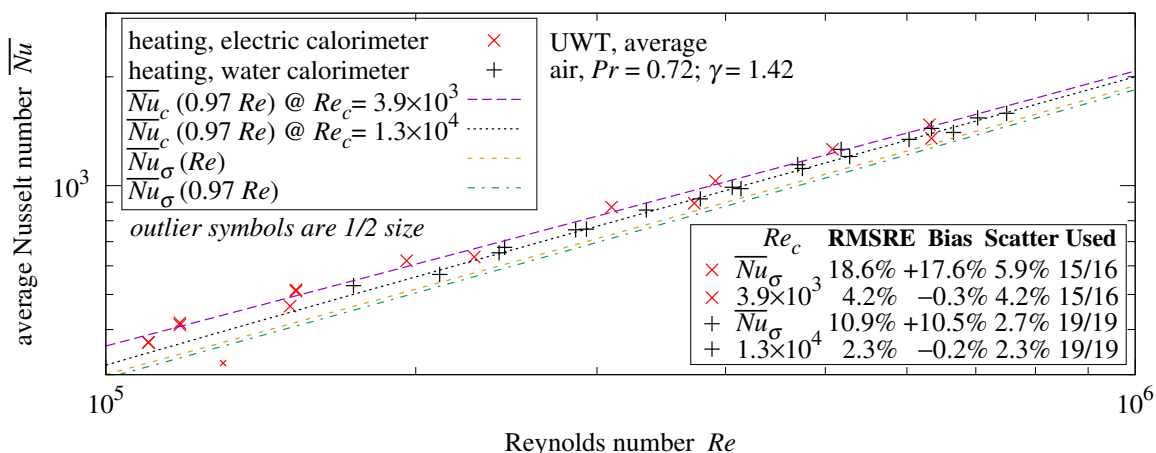


Figure 38 UWT average convection in air

14.11 Water. Unlike air, water’s viscosity and thermal properties vary significantly with temperature. Grouping by Pr is insufficient to characterize these data sets having three independent variables (T_∞ , T_w , and Re). Most are between the \overline{Nu}_σ traces for heating and cooling plates in Figure 39. The measurements below the “ $\overline{Nu}_\sigma(0.98 Re)$ @ $Pr = 2.05$ ” trace correspond to the group of measurements near the top of Figure 35.

The initial RMSRE calculations exceeded 10%. Figure 40 compares the Žukauskas and Šlančiauskas water property values with formulas from Pramuditya [39] based on Wagner and Průš [40]. Correcting per these formulas did not significantly reduce the RMSRE values.

This investigation hypothesizes that the \overline{Nu} measurements had been calculated with a constant $k = 0.54 \text{ W}/(\text{m} \cdot \text{K})$ instead of temperature dependent values. Correcting per this hypotheses and water property values, the RMSRE values for pierced-laminar \overline{Nu}_c are 5.1% or less.

- UHF convection is staged-transition \overline{Nu}_4 with $Pr = Pr_\infty$.
- UWT convection is pierced-laminar \overline{Nu}_c with $Pr = Pr_w^{1/4} Pr_\infty^{3/4}$.
- Triggered turbulence leading a smooth plate should be modeled as a smooth plate with a small Re_c .

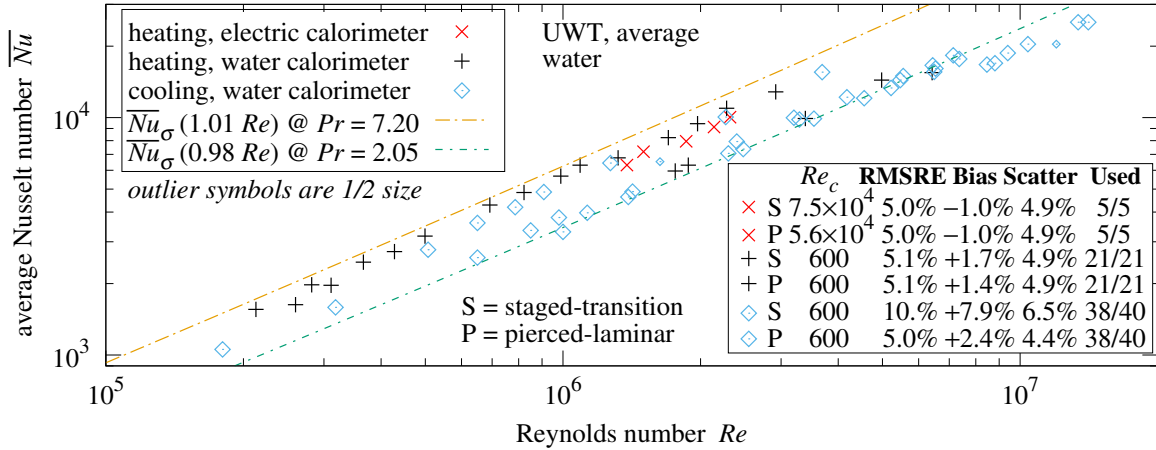


Figure 39 UWT average convection in water

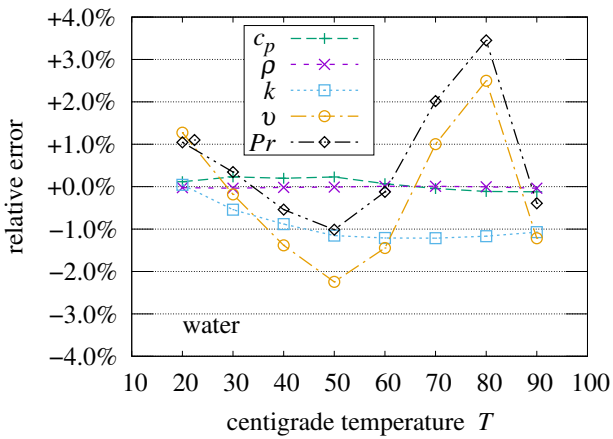


Figure 40 Water property fits

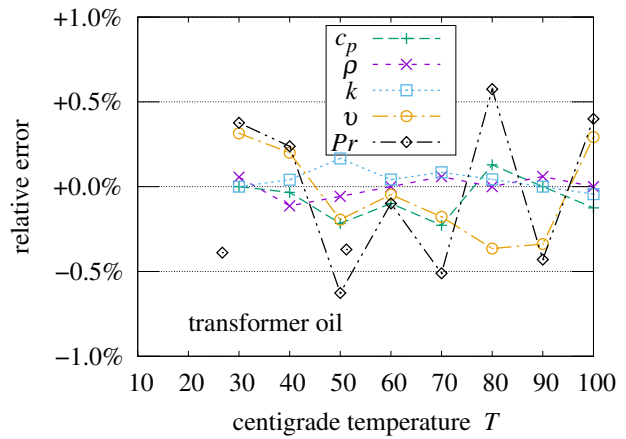


Figure 41 Transformer oil property fits

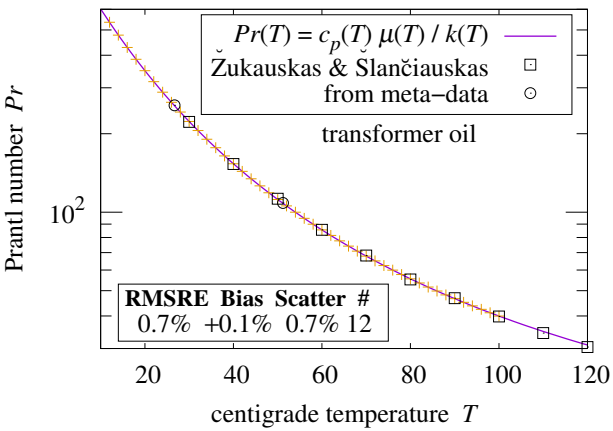


Figure 42 Transformer oil Pr

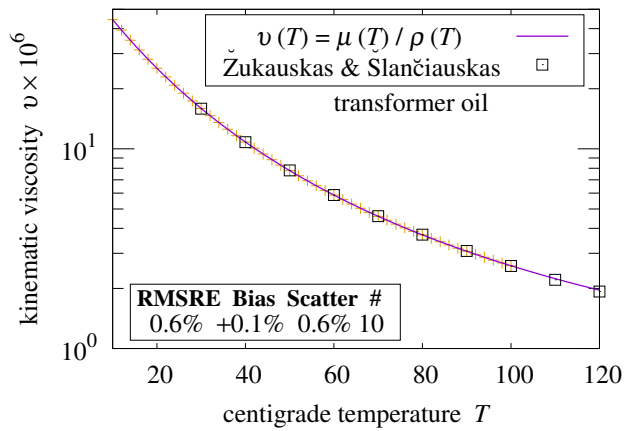


Figure 43 Transformer oil ν

14.12 **Transformer Oil.** There are multiple sources for the viscosity and thermal properties of air and water; the only source for the transformer oil used in these experiments is a 10-row table (30°C – 120°C) in the appendix of Žukauskas and Šlančiauskas [18]. The data-set temperatures span 18°C – 90°C. Thus, there is no information about the oil’s behavior between 18°C and 30°C, where the slopes of the ν and Pr curves are changing most rapidly. Dynamic viscosity was fit by $\mu = 91.877 \times 10^{-6} \exp(587/[T + 86.45])$. Having less variation, ρ , k , and specific heat (at constant pressure) c_p were modeled by linear ramps. Figure 41 shows the curves hewing to Žukauskas and Šlančiauskas [18] within $\pm 0.7\%$. Figures 42 and 43 plot the table values and this investigation’s hypothesized $Pr(T)$ and $\nu(T)$ curves at 10°C – 120°C.

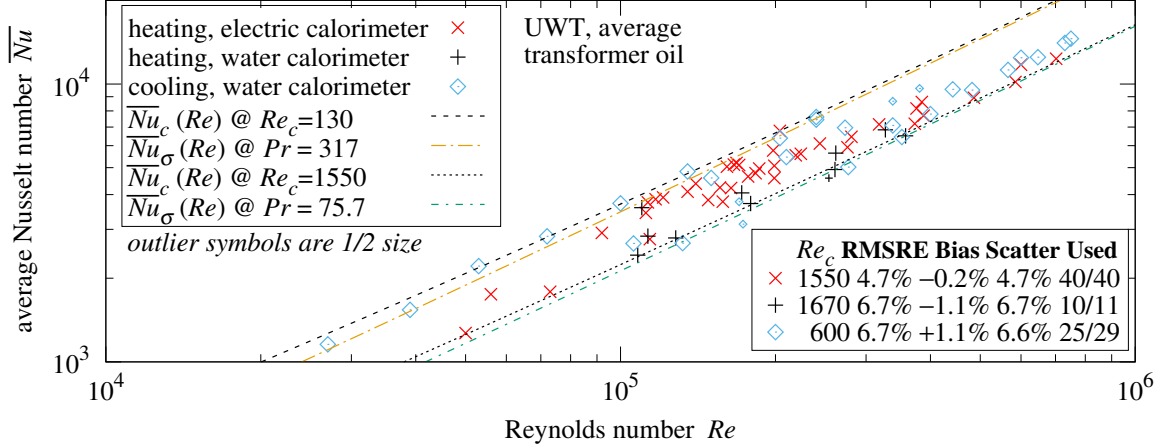


Figure 44 UWT average convection in oil

Žukauskas and Šlančiauskas [18] apparently calculated transformer oil \overline{Nu} with a constant $k(10^\circ\text{C}) = 0.126 \text{ W}/(\text{m}\cdot\text{K})$ instead of temperature dependent values. As with the water measurements, this is corrected in this investigation’s plots and RMSRE calculations. Figure 44 plots the transformer oil measurements, which are nearly bounded by pierced-laminar \overline{Nu}_c traces for heating and cooling plates.

Relative to pierced-laminar \overline{Nu}_c formula (91), the heating electric calorimeter data-set of 40 measurements had 4.7% RMSRE. Excluding one negative outlier from 11 points, the heating water calorimeter set had 6.7% RMSRE. Excluding two positive and two negative outliers from 29 points, the cooling water calorimeter set also had 6.7% RMSRE.

Having only an incomplete source of transformer oil properties creates additional uncertainty for the transformer oil convection measurements.

- Relative to pierced-laminar \overline{Nu}_c formula (91), the Žukauskas and Šlančiauskas [18] UWT data sets for air, water, and transformer oil have RMSRE values between 2.3% and 6.7%.

15. Free-Stream Turbulence

For smooth plates, Re_c varies inversely with the free-stream turbulence ratio Tu (Schlichting [9]). Figure 45 plots Re_c , which Lienhard [29] fitted to each transition data-set, versus its reported Tu .

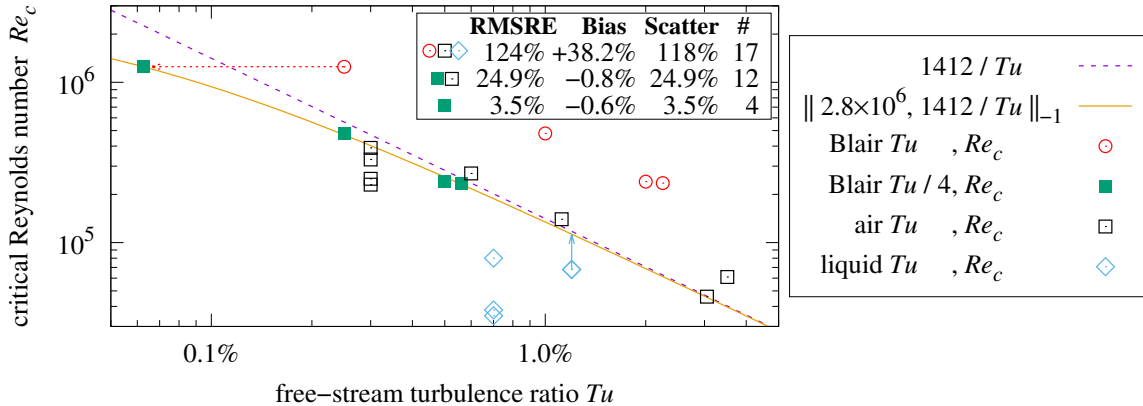


Figure 45 Critical Re_c versus free-stream turbulence

The three measurements from Blair [41] were made in air at three Tu values. The fourth is from Reynolds et al. [42, 22]. These points are above the others in Figure 45. Blair [41] wrote: “Bradshaw . . . has justified the use of the free-stream turbulence intensity (u'/U_e) to replace the more cumbersome parameter u'_e/U_τ ”. Its reference, “Bradshaw, P., Effect of Free-Stream Turbulence on Turbulent Shear Layers, ARC, Paper 35648, 1974”, has not been located by this investigation. Reynolds et al. [42] wrote “The free-stream turbulence level was measured by hot-wire-anemometry techniques.”, but gave no details.

This investigation hypothesizes that Reynolds et al. and Blair used a turbulence metric which was scaled by 4 relative to the conventional turbulence metric.

Dividing Tu by 4 (“Blair $Tu/4$, Re_c ” in Figure 45) aligns these measurements with most of the others.

The Re_c upper-bound from Schubauer and Skramstad [33] was 2.8×10^6 . Let:

$$Re_c = \left\| 2.8 \times 10^6, 1412/Tu \right\|_{-1} \quad (101)$$

The shifted Reynolds et al. and Blair points have 3.5% RMSRE from the $\left\| 2.8 \times 10^6, 1412/Tu \right\|_{-1}$ curve, formula (101). Combined, the “air” and corrected “Blair” points have 25% RMSRE.

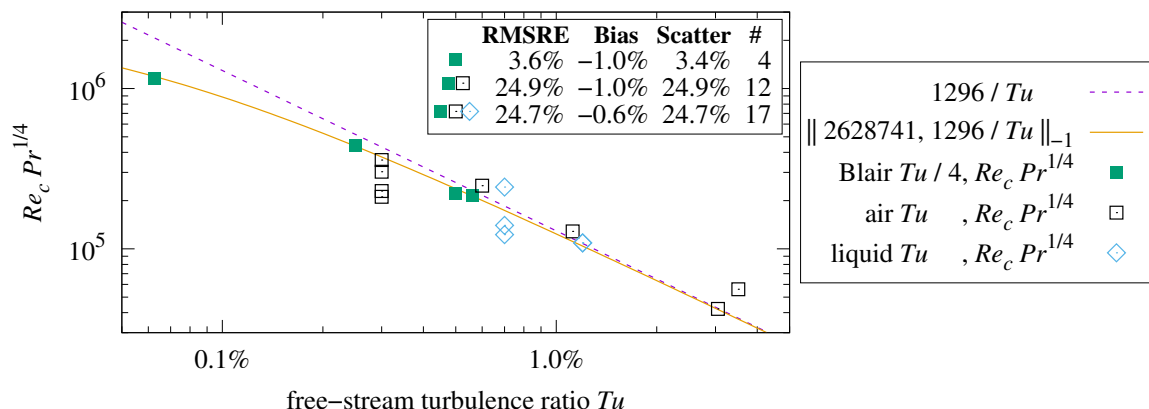


Figure 46 $Re_c \sqrt[4]{Pr}$ versus free-stream turbulence

15.1 Liquids. Only the five “liquid” points from Žukauskas and Šlančiauskas [18] had $Pr > 1$; Moreover, the larger the Pr , the lower its (Lienhard-fitted) Re_c . Figure 46 replaces the ordinate axis with $Re_c \sqrt[4]{Pr}$, moving the liquid points upward. This $\sqrt[4]{Pr}$ factor suggests $6^4 = 1296$ as the coefficient and $6^4 6^4 \sqrt[4]{6} \approx 2.629 \times 10^6$ as the upper-bound in formula (102):

$$Re_c = \left\| 2.629 \times 10^6, 1296/Tu \right\|_{-1} / \sqrt[4]{Pr} \quad (102)$$

The 17 points have 25% RMSRE from formula (102) in Figure 46. The upper-bound in air, $2.629 \times 10^6 / \sqrt[4]{0.71} \approx 2.864 \times 10^6$, is about 2% larger than the Schubauer and Skramstad [33] value, 2.8×10^6 .

- With Tu scaled by 1/4, the four Reynolds et al. and Blair points have 3.6% RMSRE from formula (102).
- Formula (102) correlates the reported Tu values from seventeen UWT and UHF transition data-sets with Re_c from Lienhard [29] with 25% RMSRE.

Several of the transition studies reported Tu values with low precision, for example the four points at $Tu = 0.3\%$ in Figure 46. Studies with more precise measurements of Tu would better test formula (102).

16. Fully Rough Regime Friction

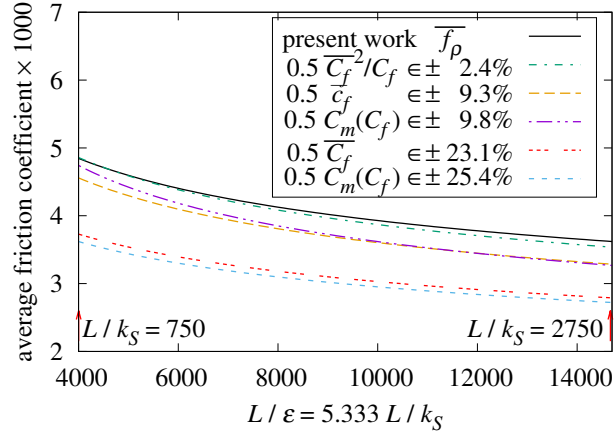


Figure 47 Average friction coefficient of sand-roughness

16.1 **Average Formulas From Prior Work.** Figure 47 compares fully rough regime average skin-friction formulas. To the right of each “ $\in \pm$ ” is the maximum discrepancy from \overline{f}_ρ formula (29) over the Mills-Hang range $750 < L/k_S < 2750$, which is $4000 < L/\varepsilon < 14666$.

Formula (9) is the Mills-Hang local friction formula. Starting from the bottom of the Figure 47 key:

- “ $0.5 C_m(C_f) \in \pm 25.4\%$ ” is 1/2 of the Churchill smooth averaging formula (14) applied to formula (9).
- “ $0.5 \overline{C}_f \in \pm 23.1\%$ ” is 1/2 of the Mills-Hang average formula (10).
- “ $0.5 C_m(C_f) \in \pm 9.8\%$ ” is 1/2 of the Churchill rough averaging formula (15) applied to formula (9).
- “ $0.5 \overline{c}_f \in \pm 9.3\%$ ” is 1/2 of the Prandtl-Schlichting average formula (8).
- “ $0.5 \overline{C}_f^2/C_f \in \pm 2.4\%$ ” is 1/2 of formula (59), the disrupted boundary-layer averaging formula (58) applied to formula (9); it matches \overline{f}_ρ within $\pm 2.4\%$.

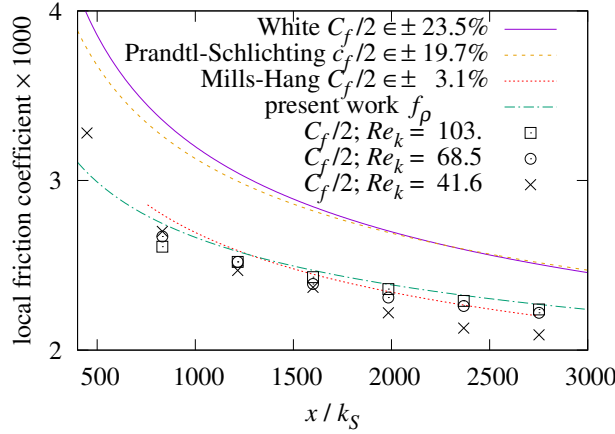


Figure 48 Pimenta et al. versus x/k_S

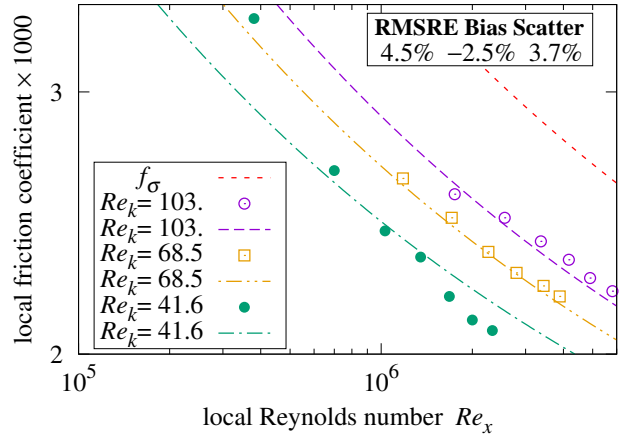


Figure 49 Pimenta et al. versus Re_x

16.2 **Local Formulas From Prior Work.** Figure 48 plots the local friction coefficients from White (11), Prandtl-Schlichting (7), Mills-Hang (9), and present work f_ρ formula (61).

- Mills-Hang matches f_ρ formula (61) within 3.1% over $750 < x/k_S < 2750$.

Table 7 Local friction coefficient of sphere-roughened plate

Source	Formula	RMSRE	Bias	Scatter	Used
Prandtl and Schlichting [3]	(7) $c_f/2$	15.6%	-15.4%	2.6%	19/19
Mills and Hang [8]	(9) $C_f/2$	3.7%	-2.4%	2.8%	19/19
White [10]	(11) $C_f/2$	16.6%	-16.3%	3.3%	19/19
present work	(61) f_ρ	4.5%	-3.0%	3.3%	19/19

16.3 Comparison With Local Drag Measurements. The points labeled “ $C_f/2; Re_k =$ ” in Figure 48 show the local drag coefficient measurements versus x/k_S for the sphere-roughened plate at three rates of flow. Table 7 presents RMSRE of this set of 19 measurements to each of the rough regime formulas.

Formula (41) calculates x/ε from the Re_x and $Re_\varepsilon = Re_k/5.333$ values supplied by Pimenta et al. [7]. Figure 49 plots local $f_\rho(x/\varepsilon)$ versus Re_x for the sphere-roughened plate.

- The Pimenta et al. measurements have RMSRE 4.5% from f_ρ formula (61).

16.4 Onset of Rough Turbulence. Table 6 (Re_λ formula (45)) predicts that fluid flow along the entire sphere-roughened plate transitions directly from laminar to rough turbulence at $Re_\lambda \approx 5.5 \times 10^4$; however, the smallest reported Re_x was 3.8×10^5 .

17. Friction Measurements of Diverse Types of Roughness

Bergstrom et al. [14] has skin-friction coefficient measurements of sandpapers, woven wire meshes, and perforated sheets attached to a smooth plate, and also the $1.67\text{ m} \times 1.16\text{ m}$ smooth plate alone. Skin-friction measurements were derived from Pitot probe measurements of air velocity at locations which were 1.3 m downwind from the leading edge of the plate. Bergstrom et al. [14] estimated 5% as the combined measurement uncertainty of the smooth surface friction coefficient, and 9% for the rough surfaces.

The measurement tables in [14] include a column for free-stream velocity, U_e . In order to compute the Reynolds number $Re = U_e L/\nu$ from U_e , the kinematic viscosity $\nu = 16 \times 10^{-6} \text{ m}^2/\text{s}$ was calculated for air at 20°C, 25% RH, and 95 kPa, the mean atmospheric pressure at the University of Saskatchewan.

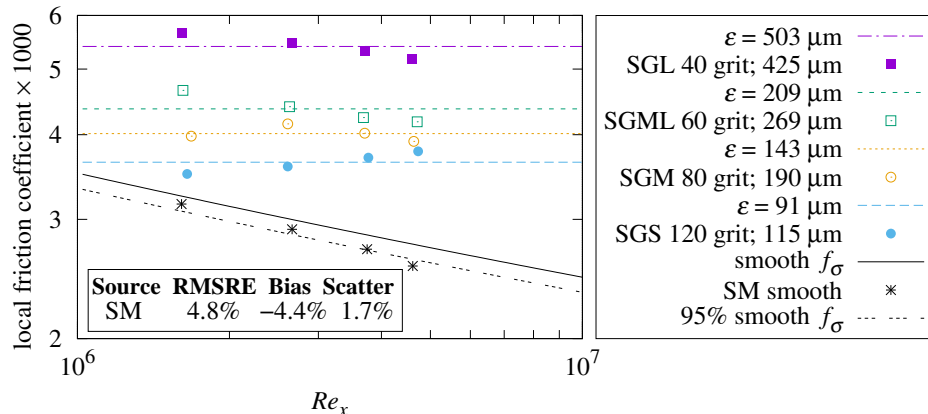


Figure 50 Local f_ρ versus Re_x of sandpaper

17.1 Smooth Plate. Three of the four smooth plate measurements are within the 5% band, as shown by the points labeled “SM smooth” in Figure 50. The RMSRE versus f_σ formula (64) is 4.8%.

17.2 Sandpaper. Microscopic examination of coarse grades of sandpaper reveals glued mounds of grits separated by canyons having depths which are several times the mean grit diameter. Sandpaper grit mean diameter is standardized, but not the height-of-roughness of the mounds; it can vary by manufacturer and lot. The horizontal traces in Figure 50 show that skin-friction coefficients which are independent of Re_x , as in the present theory, can be within the 9% estimated measurement uncertainty of the data.

17.3 Comparison With Sand-Roughness. The RMS height-of-roughness ε of sandpaper is much larger than ε of sand-roughness with the same mean grit diameter. For example, 40 grit sandpaper has a skin-friction coefficient consistent with $\varepsilon \approx 503 \mu\text{m}$, while $k_S = 425 \mu\text{m}$ sand-roughness would have $\varepsilon = k_S/5.333 \approx 80 \mu\text{m}$.

17.4 Woven Wire Mesh.

Table 8 Wire mesh dimensions

Wire diameter d	Spacing s	$[s - d]^2/s^2$	$[s - \sqrt{2}d]^2/s^2$	From [14]	Tag
1.04 mm	3.68 mm	52%	36%	35%	WML
0.58 mm	1.77 mm	45%	29%	30%	WMM
0.36 mm	1.68 mm	62%	49%	<u>44%</u>	WMS
0.36 mm	1.48 mm	58%	<u>44%</u>		
0.56 mm	1.68 mm	<u>44%</u>	28%		

17.5 Mesh Openness. Woven wire meshes are specified by wire diameter d and wire center spacing s . Bergstrom et al. [14] calculate mesh openness as $[s - \sqrt{2}d]^2/s^2$ instead of the $[s - d]^2/s^2$ formula used by manufacturers (neither metric is plateau openness Ω). Table 8 lists the dimensions and openness from [14] along with openness calculated both ways. The WML and WMM meshes have $[s - \sqrt{2}d]^2/s^2$ values close to [14]. The WMS mesh has $[s - \sqrt{2}d]^2/s^2 \approx 49\%$, versus 44% from [14]. If the 1.68 mm spacing were instead 1.48 mm, WMS would have $[s - \sqrt{2}d]^2/s^2 \approx 44\%$, but significantly less friction coefficient than the WMS measurements in Figure 51. A 0.36 mm wire diameter has conventional openness $[s - d]^2/s^2 \approx 44\%$ and matches the WMS data and the WMM trace and data.

17.6 Gaps. There are periodic gaps between the wires and the plate; so the mesh-plate combination is not strictly a roughness. With the gaps filled, the RMS height-of-roughness ε would be:

$$\begin{aligned}
 z(x, y) &= \sqrt{\frac{d^2}{4} - x^2} + d - \frac{d}{2} \cos \frac{\pi y}{s} \\
 \bar{z} &= \frac{4}{s^2} \int_{d/2}^s \int_0^{d/2} z(x, y) dx dy \\
 \varepsilon &= \frac{4}{s^2} \int_{d/2}^s \int_0^{d/2} |z(x, y) - \bar{z}|^2 dx dy + \frac{[s - d]^2 \bar{z}^2}{s^2}
 \end{aligned} \tag{103}$$

The periodic gaps between wires and the plate increase the flow’s shearing stress. Scaling ε by the square root of the filled-gap per empty-gap side area ratio is an increase of about 26% for these meshes:

$$\varepsilon' = \varepsilon \sqrt{\frac{12s + \pi d}{8s}} \tag{104}$$

The “unscaled 1.04 mm, 3.68 mm” trace in Figure 51 shows the predicted WML friction without this scaling.

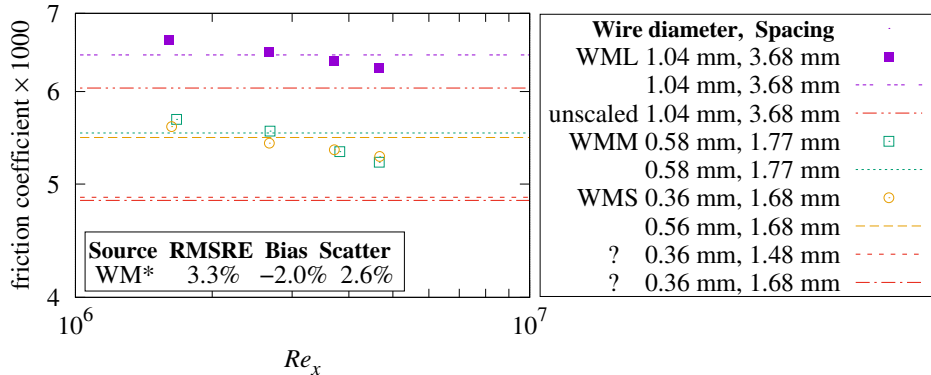


Figure 51 Local f_ρ versus Re_x of woven wire mesh

- Using (scaled) ε' , the WML and WMM measurements match the present theory well within the $\pm 9\%$ estimated measurement uncertainty. The WMS measurements do not match unless a hypothesized single digit misprint in [14] is corrected, changing the wire diameter from 0.036 mm to 0.056 mm. Taken together, the (corrected) three wire meshes have 3.3% RMSRE versus the present theory.

17.7 Perforated Sheet.

Table 9 Perforated sheet openness

Hole diameter d	Spacing s	Square Ω	Hexagonal Ω	From [14]	Tag
2.0 mm $\approx 5/64$	2.81 mm $\approx 7/64$	39.8%	45.9%	45%	PL
1.6 mm $\approx 4/64$	2.43 mm $\approx 6/64$	34.1%	39.3%	41%	PM
1.2 mm $\approx 3/64$	3.40 mm $\approx 8.6/64$	9.8%	11.3%	<u>22%</u>	PS
1.7 mm $\approx 4.3/64$	3.40 mm $\approx 8.6/64$	19.6%	<u>22.7%</u>		
1.2 mm $\approx 3/64$	2.40 mm $\approx 6/64$	19.6%	<u>22.7%</u>		

17.8 Perforated Sheet Openness. Table 9 checks the openness of the perforated sheets from Bergstrom et al. [14]. It indicates that the holes were hexagonally arrayed. However, the PS sheet’s calculated openness is 1/2 of the paper’s 22%. There are two single digit changes, either of which results in hexagonal openness near 22%: hole diameter $d = 1.7$ mm or center spacing $s = 2.4$ mm.

North American suppliers of perforated sheet metal generally specify hole diameter and center spacing in terms of 1/64 of an inch. Table 9 provides dimensions both ways. $d = 3/64$ with $s = 6/64$ is a standard size; $d = 4.3/64$ with $s = 8.6/64$ is not. Replacing PS row $s = 3.40$ mm with $s = 2.40$ mm:

Table 10 Perforated sheet parameters

$[4L^*] = d$	$L_P = s$	Ω	d^2/s^2	ζ	ε	Re_W	Tag
2.0 mm	2.81 mm	45.9%	0.507	0.90 mm	0.449 mm	1.96×10^6	PL
1.6 mm	2.43 mm	39.3%	0.434	0.90 mm	0.441 mm	3.84×10^6	PM
1.2 mm	2.40 mm	22.7%	0.250	0.76 mm	0.318 mm	2.71×10^6	PS

17.9 Plateau Wells. Table 10 shows the dimensions and metrics of the ζ -thick perforated sheets when laid on the flat plate. For PL, $[4L^*]^2/L_P^2 = d^2/s^2 \approx 0.507 > 1/2$; its flow will be rough turbulent. The “ $f_\rho(2898) = 0.0052$ ” trace in Figure 52 shows the predicted local skin-friction coefficient’s close proximity to the PL measurements. The “? 2.00 mm, 2.81 mm, 0.90 mm” trace with transition at “PL?” shows the behavior predicted if $d^2/s^2 < 1/2$ had been the case.

PM and PS have $d^2/s^2 < 1/2$. As Re_x grows to exceed Re_W , the local drag coefficient gradually transitions from blend formula (84) to smooth formula (85). The Re_W formula (51) transitions are marked by vertical lines. Figure 23 details the PS and PM abrupt and smooth transitions.

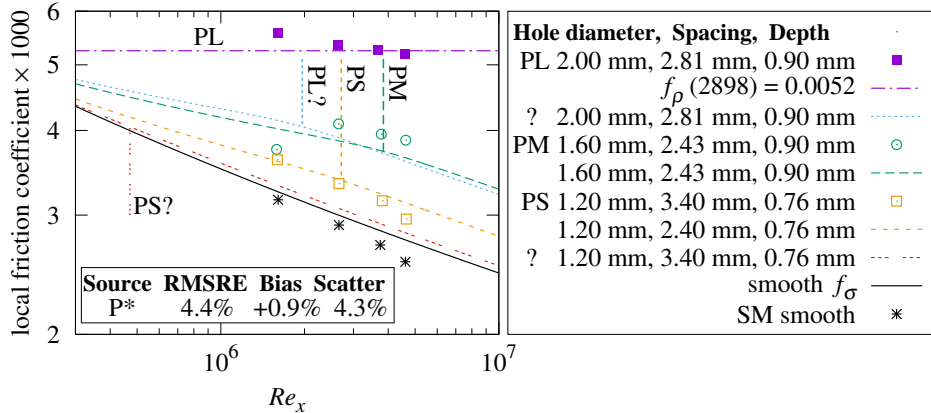


Figure 52 Local f_ρ versus Re_x of perforated sheet

- PL and PM measurements match the present theory within the $\pm 9\%$ measurement uncertainty. The PS measurements do not match unless a hypothesized single digit misprint in [14] is corrected, changing the PS hole spacing from 3.4 mm to 2.4 mm. The “PS?” trace shows the behavior predicted of the original PS. Taken together, the (corrected) three perforated sheets have 4.4% RMSRE versus the present theory.

18. Rough Convection Measurements

Both the Pimenta et al. [7] and Bergstrom et al. [14] measurements are restricted to flow rate ranges of less than 3:1. For a novel theory to be persuasive, confirmations over a wider range of flow rates are needed.

The present apparatus combined an open intake wind-tunnel, software phase-locked loop (PLL) fan control, and a heated aluminum plate. It measured average convection in air at $2300 < Re < 93000$, a 40:1 range. Section 24 describes the apparatus and measurement methodology.

18.1 Bi-Level 3 mm Roughness. A square grid of 6 mm deep grooves in a $0.305 \text{ m} \times 0.305 \text{ m}$ plate created the $\varepsilon = 3.0 \text{ mm}$ bi-level roughness.

The two peripheral $2\varepsilon \times L$ sides of the bi-level plate roughness which are parallel to the fluid flow also contribute to forced convection. Turning to dimensional analysis, ε and plate width L_W cooperate weakly, leading to an effective width of $\|L_W, \varepsilon\|_{\sqrt{1/2}}$, about a 5.4% increase.

Applying average convection formula (65) to the bi-level plate geometry, with the 5.4% increase, yields:

$$\overline{Nu}_\rho(Re) = 0.00823 Re Pr^{1/3} \quad (105)$$

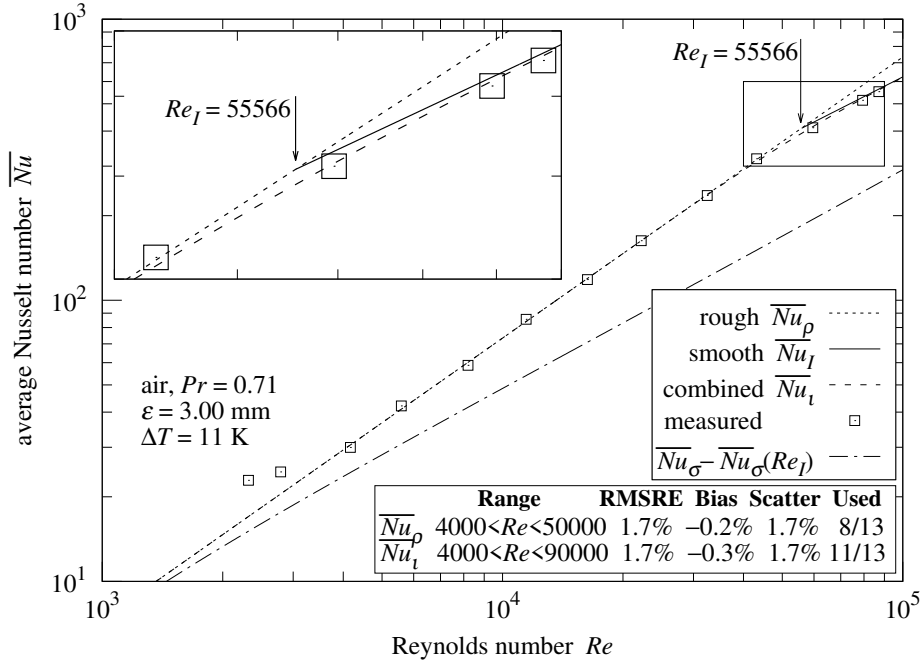


Figure 53 Convection from bi-level plate; $L/\varepsilon = 102$

Figure 53 shows convection measurements made with the plate averaging 11 K warmer than the ambient air. \overline{Nu}_ρ is formula (105); \overline{Nu}_I is formula (83). At $Re < 3000$, the natural convection component dominates the mixture; hence, measurements at $Re < 3000$ are excluded from the RMSRE calculations.

- Measurements in the range $4000 < Re < 50000$ match \overline{Nu}_ρ formula (105) with 1.7% RMSRE.

At $Re > Re_I = 55566$, \overline{Nu}_I is formula (81); its 4/5 slope shows that convection is from smooth turbulent flow. Its height above the $\overline{Nu}_\sigma - \overline{Nu}_\sigma(Re_I)$ trace shows that it is operating with a shorter characteristic length than $\overline{Nu}_\sigma - \overline{Nu}_\sigma(Re_I)$. The Figure 53 inset shows that \overline{Nu}_I formula (83) is a closer match to measurements at $60000 < Re < 90000$ than an abrupt transition.

- Measurements in the range $4000 < Re < 90000$ match the plateau islands \overline{Nu}_I formula (83) with 1.7% RMSRE.

18.2 Bi-Level 1 mm Roughness. After making a variety of convection measurements, the $\varepsilon = 3 \text{ mm}$ plate was machined to reduce its roughness to $\varepsilon = 1.04 \text{ mm}$.

In order to preserve the plate’s wire suspension, the four corner posts were not shortened. The Re_I transition involves only the leading portion of the plate. $Re_I = 6178$ was calculated by formula (50) using $\varepsilon = 1.14$ mm, the RMS height-of-roughness of the leading three rows of posts.

The plate’s effective width, $\|L_W, \varepsilon\|_{\sqrt{1/2}}$, is about 2.6% larger than L_W , but affects only \overline{Nu}_ρ flow at $Re < 6178$. \overline{Nu}_I formula (83) already accounts for smooth convection from the post sides.

In Figure 54, \overline{Nu}_i is formula (83). At $Re < 5000$, the natural convection component dominates the mixture; hence, measurements at $Re < 5000$ are excluded from the RMSRE calculations.

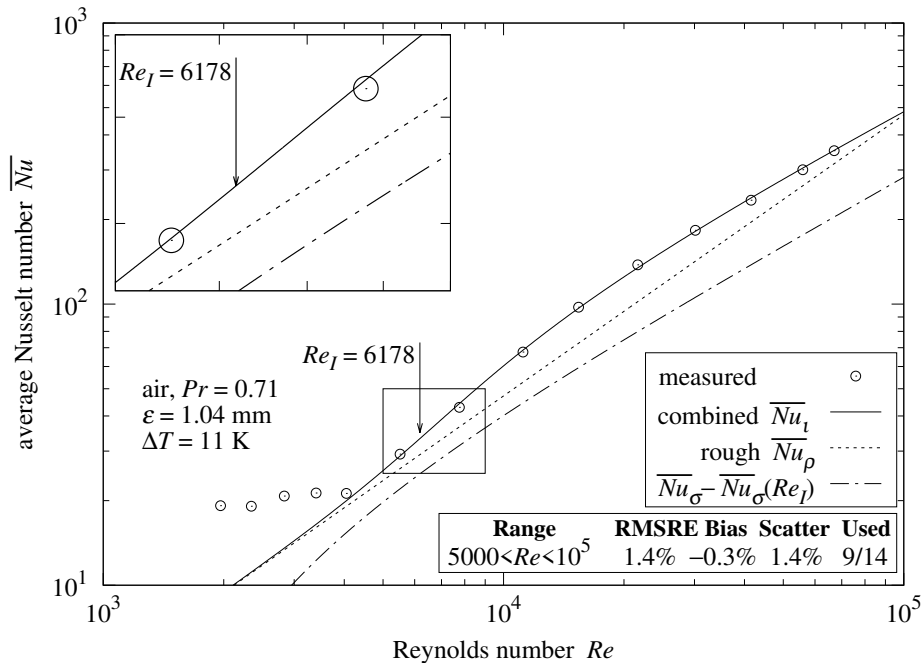


Figure 54 Convection from bi-level plate; $L/\varepsilon = 295$

The ℓ^{-4} -norm in \overline{Nu}_i formula (83) fits very well with the measurements in Figure 54. Replacing it with the ℓ^{-2} -norm drives some \overline{Nu} values out of the expected uncertainty bounds.

- Convection measurements at $5000 < Re < 10^5$ match plateau-islands formula (83) with 1.4% RMSRE.

18.3 Onset of Rough Turbulence. Re_λ formula (45) predicts that the flow along the leading band of roughness of the 3 mm bi-level plate transitions from laminar to rough turbulence at $Re_\lambda \approx 175$, which is too slow to test in this apparatus. Formula (45) predicts $Re_\lambda = 1473$ for the 1 mm bi-level plate. The plate was found to have convection consistent with rough turbulence at $Re \approx 2500$, which is less than $2 Re_\lambda$.

18.4 Duck Tape. The bi-level test plate of the present apparatus has four sides perpendicular to the test-surface, each a wedge of extruded polystyrene foam (XPS) insulation filling a 2.7 cm 45° chamfer in the metal slab. In order to isolate the convective heat flow of the test-surface from that of the sides, the estimated side convection, between 50% at $Re = 6000$ and 7% at $Re = 90000$ of the measured heat flow, is deducted from that measured heat flow (see Section 24 for details).

The surface of the XPS foam board in Figure 55 was not smooth and not an isotropic, periodic roughness. Without a theoretical basis for computing its convection, the accuracy of measurements of the surface-under-test would have been limited. Hence, the foam was covered with Intertape AC6 duck tape, a 152 μm -thick polyester cloth/polyethylene film with a pressure sensitive adhesive (shown in Figure 55). The geometric mean of its 3.62 mm \times 1.47 mm thread cell is $s \equiv L_P \approx 2.31$ mm; the thread diameter plus the sheet thickness is $d \approx 0.10$ mm. The filled-gap woven wire mesh formula (103) calculates $\varepsilon \approx 0.0403$ mm. These values with $L = 0.305$ m yielded the “duck tape” row in Table 6.

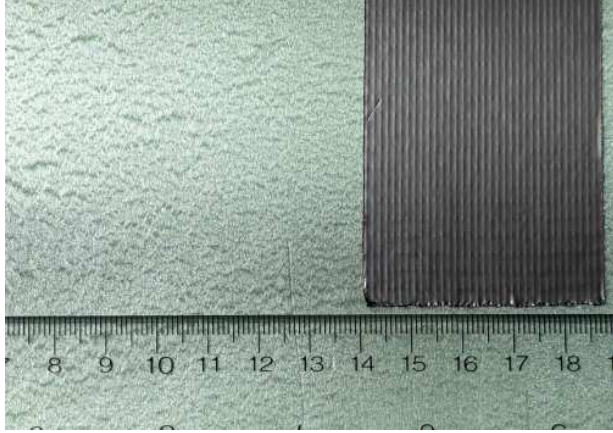


Figure 55 XPS foam board and duck tape

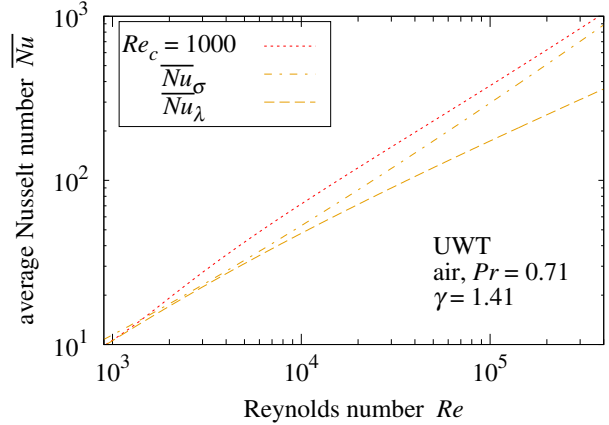


Figure 56 duck tape convection

18.5 Pierced-Laminar Convection From Roughness. In the present theory, an $L = 0.305$ m strip of duck tape fails to generate rough turbulence in the present apparatus because the apparatus’s largest $Re \approx 93000 < Re_\lambda \approx 1.9 \times 10^5$. Because $Re_\sigma > L/\sqrt{\varepsilon L_P}$ in the duck tape row of Table 6, the critical $Re_c = L/\sqrt{\varepsilon L_P} \approx 1.0 \times 10^3$ in \overline{Nu}_c formula (91) convection.

With duck tape applied to the foam faces, the measurements presented in Section 18 are consistent with the side convection modeled by pierced-laminar formula (91). The other curves in Figure 56 are substantially less than formula (91); they do not account for enough heat transfer to keep the surface-under-test measurements within the expected uncertainty bounds presented in Section 24.

That consistency rules out laminar \overline{Nu}_λ , smooth turbulence \overline{Nu}_σ , and staged-transition \overline{Nu}_4 as explanations of convection from the duck tape covered sides in combination with plateau islands \overline{Nu}_i convection from the 1 mm and 3 mm roughness plates. This evidence is not conclusive, but supports pierced-laminar formula (91) convection from the duck tape surface.

19. Results

Tables 11 and 12 summarize the present theory’s conformance with 456 measurements in 32 data-sets from one book, six peer-reviewed studies, and the present apparatuses.

Table 13 lists all of the top-level formulas tested by at least one of these data-sets.

$L/\varepsilon = \infty$ signifies a smooth plate; in Table 12 it is followed by “UHF”, “UWT” or “UWT–” indicating a heated UHF plate, a heated UWT plate, or a cooled UWT plate, respectively.

- Relative to the present work formulas, the 32 data-set RMSRE values span 0.75% through 8.2%.
- Only four of the 32 data-sets have RMSRE exceeding 6%.

Table 11 Friction measurements versus present theory

Source	L/ε	Formula	Pr_∞	RMSRE	Bias	Scatter	Used
[11, 16, 17] Churchill	∞	(32) $\overline{f_\sigma}$	0.71	.75%	+1.3%	.74%	9/9
[11, 16, 17] Churchill	∞	(64) f_σ	0.71	1.9%	+1.2%	1.4%	11/11
[18] Žukauskas & Šlančiauskas	∞	(64) f_σ	55.2	2.5%	+0.6%	2.4%	5/5
[18] Žukauskas & Šlančiauskas	∞	(64) f_σ	5.42	5.2%	+4.9%	1.8%	8/8
[18] Žukauskas & Šlančiauskas	∞	(64) f_σ	2.78	3.3%	+1.0%	3.1%	8/8
[18] Žukauskas & Šlančiauskas	∞	(64) $\overline{f_\sigma}$	0.71	4.4%	−1.4%	4.2%	9/9
[19, 20] Gebers	∞	(90) $\overline{f_c}$		2.8%	−0.2%	2.8%	33/33
[7] Pimenta et al.	1.5×10^3	(61) f_ρ	0.71	4.5%	−3.0%	3.3%	19/19
[14] Bergstrom et al.	∞	(64) f_σ	0.71	4.8%	−4.4%	1.7%	4/4
[14] Bergstrom et al. – mesh	1600-3000	(61) f_ρ	0.71	3.3%	−2.0%	2.6%	12/12
[14] Bergstrom et al. – wells	1200-1500	(86) f_w	0.71	4.4%	+0.9%	4.3%	12/12

Note: Churchill [11] extracted its measurements from Smith and Walker [16] and Spalding and Chi [17].

Table 12 Convection measurements versus present theory

Source	L/ε	Formula	Pr_∞	RMSRE	Bias	Scatter	Used
[21] Kestin et al.	∞ UWT	(96) Nu_c	0.7	3.8%	-1.0%	3.7%	7/7
[21] Kestin et al.	∞ UWT	(96) Nu_c	0.7	8.2%	+1.5%	8.0%	13/13
[22] Reynolds et al.	∞ UWT	(96) Nu_c	0.71	6.4%	+2.3%	6.0%	22/22
[18] Žukauskas & Šlančiauskas	∞ UHF	(94) Nu_4	0.71	1.0%	+0.3%	1.0%	8/10
[18] Žukauskas & Šlančiauskas	∞ UHF	(94) Nu_4	0.71	2.5%	-0.7%	2.4%	8/10
[18] Žukauskas & Šlančiauskas	∞ UHF	(94) Nu_4	0.71	1.7%	-0.7%	1.5%	8/10
[18] Žukauskas & Šlančiauskas	∞ UHF	(94) Nu_4	6.57	3.8%	-0.7%	3.8%	19/19
[18] Žukauskas & Šlančiauskas	∞ UHF	(94) Nu_4	6.57	3.4%	-0.2%	3.4%	15/15
[18] Žukauskas & Šlančiauskas	∞ UHF	(94) Nu_4	108.	2.4%	-0.0%	2.4%	17/17
[18] Žukauskas & Šlančiauskas	∞ UHF	(94) Nu_4	257.	5.6%	+0.8%	5.5%	17/17
[18] Žukauskas & Šlančiauskas	∞ UWT	(91) $\overline{Nu_c}$	0.71	4.2%	-0.3%	2.3%	15/16
[18] Žukauskas & Šlančiauskas	∞ UWT	(91) $\overline{Nu_c}$	0.71	2.3%	-0.2%	2.3%	19/19
[18] Žukauskas & Šlančiauskas	∞ UWT	(91) $\overline{Nu_c}$	5.8-7.1	5.0%	-1.0%	4.9%	5/5
[18] Žukauskas & Šlančiauskas	∞ UWT	(91) $\overline{Nu_c}$	2.9-7.2	5.1%	+1.4%	4.9%	21/21
[18] Žukauskas & Šlančiauskas	∞ UWT	(91) $\overline{Nu_c}$	2.0-5.8	5.0%	+2.4%	4.4%	38/40
[18] Žukauskas & Šlančiauskas	∞ UWT	(91) $\overline{Nu_c}$	75-246	4.7%	-0.2%	4.7%	40/40
[18] Žukauskas & Šlančiauskas	∞ UWT	(91) $\overline{Nu_c}$	80-205	6.7%	-1.1%	6.7%	10/11
[18] Žukauskas & Šlančiauskas	∞ UWT	(91) $\overline{Nu_c}$	92-317	6.7%	+1.1%	6.6%	25/29
present apparatus - 3 mm bi-level	102 UWT	(65) $\overline{Nu_\rho}$	0.71	1.7%	-0.2%	-0.2%	8/13
present apparatus - 3 mm bi-level	102 UWT	(83) $\overline{Nu_l}$	0.71	1.7%	-0.3%	1.7%	11/13
present apparatus - 1 mm bi-level	295 UWT	(81) $\overline{Nu_I}$	0.71	1.4%	-0.3%	1.4%	9/14

Table 13 Top-level formula coverage

Measured	Plate	Rough $Pr < 1$	Smooth $Pr < 1$	Smooth $Pr > 1$
average friction			(32) $\overline{f_\sigma}$; (90) $\overline{f_c}$	
local friction		(61) f_ρ ; (86) f_W	(64) f_σ	(64) f_σ
average convection	UWT	(83) $\overline{Nu_i}$; (65) $\overline{Nu_\rho}$	(91) $\overline{Nu_c}$	(91) $\overline{Nu_c}$
local convection	UWT		(96) Nu_c	
local convection	UHF		(94) Nu_4	(94) Nu_4

20. Discussion

Rather than trying to tease rough turbulence from a nearly smooth surface, this investigation started with an analysis of roughness deep enough to disrupt boundary layer flow.

20.1 Skin-Friction. With boundary layers disrupted by self-similar roughness, the flow's roughness velocity u_τ was used to derive the average skin-friction coefficient $\overline{f_\rho}$. Deriving the roughness Reynolds number Re_ε led to a formula for average smooth turbulent skin-friction $\overline{f_\sigma}$ with unprecedented 0.75% RMSRE fidelity to the Smith and Walker [16], and Spalding and Chi [17] measurements (via Churchill [11]).

Section 11 and subsequent comparisons with measurements established that transforms between local and average friction differ for continuous versus disrupted boundary layers. Thus, these transforms are not valid for flows over plateau roughnesses which shed rough and smooth turbulence simultaneously.

20.2 Laminar Friction. $\overline{f_\lambda}$ formula (57) differs from the traditional $1.328/\sqrt{Re}$ formula because formula (57) is valid for all $Re \geq 0$, with $\overline{f_\lambda}(0) = 1.328/\sqrt{Re_0} \approx 0.0542$. This removes the need to treat the leading edge differently from the rest of the plate in many cases.

Measuring smooth plate $\overline{f_\lambda}$ at $Re = 1000$ in a viscous liquid, then solving formula (57) for Re_0 would refine the Re_0 value.

20.3 Forced Convection. Combining formula (76) with rough friction $\overline{f_\rho}$ formula (29) results in the formula $\overline{Nu_\rho} = Re Pr^{1/3}/[6 \ln^2(L/\varepsilon)]$, which is identical to rough turbulent convection formula (65).

Formula (76) is the original (1933) form of the Reynolds-Colburn analogy. Lienhard [29] demonstrates that the analogy can fail for smooth turbulent flows. In particular, the Pr exponent should be 0.6 in gasses.

Formula (65) using $Pr^{1/3}$ matches rough turbulent convection from the $\varepsilon = 3$ mm apparatus spanning $4000 < Re < 50000$ within its estimated measurement uncertainties (plotted in Section 24). With $Pr = 0.71$ (air), $Pr^{0.6} \approx 0.814$ is 9% smaller than $Pr^{1/3} \approx 0.892$; this mismatch exceeds some of those estimated measurement uncertainties. Thus, the Pr dependence of rough and smooth turbulent convection differ.

20.4 UHF Convection. This investigation's mathematical development of convection is predicated on UWT plates; hence Conclusions (Section 21) omits the UHF formulas.

20.5 Small Prandtl Numbers. None of the experiments performed or cited measured fluids with $0 < Pr < 0.7$. Forced convection measurements in this range are needed.

20.6 Smooth Plate Transition. The present theory asserts that all sharp-edged, flat, smooth, UWT plates are interchangeable, and their critical Re_c is controlled only by free-stream turbulence Tu and Pr .

The Re_c dependence on Pr was unexpected. However, Pr appears in the differential equations for turbulent dissipation in Tu, Yeoh, and Liu [43].

The Reynolds et al. and Blair measurements spanning $0.25 < Tu < 2.5\%$ have 3.6% RMSRE from Re_c formula (102). This supports $6^4 6^4 \sqrt[4]{6} \approx 2.629 \times 10^6$ as the $\sqrt[4]{Pr} Re_c$ upper-bound. If this is not the true upper-bound, it can be treated empirically without invalidating other aspects of the present theory.

20.7 Onset of Rough Turbulence. The present theory predicts that an isotropic, periodic rough plate with $\Omega > 1/2$ switches from all laminar to all rough turbulence as $Re > Re_\lambda$. The prior and present work measurements from rough plates were taken at $Re > Re_\lambda$; most were at $Re \gg Re_\lambda$. Measurements at Re values closely bracketing Re_λ are needed to test Re_λ formula (45).

20.8 Pierced-Laminar. Section 18 presented indirect evidence of duck tape generating pierced-laminar convection exceeding both laminar and smooth turbulent convection.

To definitively test pierced-laminar flow from roughness, convection or skin-friction measurements at Re values near Re_c are needed from a surface having $Re_c = L/\sqrt{\varepsilon L_P} < Re_\sigma < Re_\lambda$.

Measuring this in an apparatus with a known, high level of free-stream turbulence would additionally test the interaction between $L/\sqrt{\varepsilon L_P} < Re_\sigma < Re_\lambda$ roughness and free-stream turbulence.

20.9 Expected Measurement Uncertainty. The present work made several claims based on measurements being within the present apparatus's expected measurement uncertainties. Attributing discrepancies to parameters was robust because each parameter affected different Re ranges:

- The pierced-laminar convection of duck tape-covered sides affected both plates at $Re > 1000$.
- Blending plateau islands convection using the ℓ^{-4} -norm affected plates only near their Re_I values of 6178 and 55566, respectively.
- The $Pr^{1/3}$ factor in rough turbulent convection affected the $\varepsilon = 3$ mm plate at $Re_\lambda < Re < Re_I$.

21. Conclusions

- The average skin-friction coefficient of steady flow of strength Re along a smooth, flat surface is:

$$\left\| \overline{f_\lambda}(Re), \overline{f_\sigma}(Re) - \frac{Re_\gamma}{Re} \overline{f_\sigma}(Re_\gamma) \right\|_{\sqrt{2}}$$

$$Re_\gamma = \left\| Re, \frac{Re_c}{\sqrt[4]{2}} \right\|_{-4\sqrt{2}} \quad Re_c = \frac{\|2.629 \times 10^6, 1296/Tu\|_{-1}}{\sqrt[4]{Pr}}$$

$$\overline{f_\lambda}(Re) = \frac{1.328}{\sqrt{Re} + \sqrt{Re_0}} \quad \overline{f_\sigma}(Re) = \frac{\sqrt[3]{2}/3}{[W_0(Re/\sqrt{3}) - 1]^2}$$

- The ℓ^p -norm $\|\varphi, \vartheta\|_p \equiv [|\varphi|^p + |\vartheta|^p]^{1/p}$.
- Re_c is the critical Reynolds number, the Re upper-bound of purely laminar flow.
- Tu is the free-stream turbulence ratio of the bulk flow.
- Pr is the Prandtl number of the fluid.
- $Re_0 \approx 600$. $\overline{f_\lambda}(Re)$ is valid for $Re \geq 0$.
- W_0 is the principal branch of the Lambert W function; $W_0(\varphi \exp \varphi) = \varphi$ when $\varphi \geq 0$.

- The average forced convection heat transfer from a smooth, flat, isothermal plate is:

$$\begin{aligned} & \left\| \overline{Nu}_\lambda(Re), \overline{Nu}_\sigma(Re) - \overline{Nu}_\sigma(\|Re, \sqrt{\gamma} Re_c\|_{-8/\gamma}) \right\|_\gamma \\ \gamma &= 1 + \exp_2\left(-Pr^{-\sqrt{1/2}}\right) \quad \exp_2(\varphi) \equiv 2^\varphi \\ \overline{Nu}_\sigma(Re) &= \frac{Nu_0 Re \overline{f}_\sigma(Re)}{\sqrt{3}} \sqrt{\frac{Pr/\sqrt{162} + 1}{\sqrt{162} Pr \overline{f}_\sigma(Re) + 1}} \sqrt[3]{\frac{Pr/\Xi}{\|1, 1/Pr\|_3}} \quad Nu_0 = \frac{16}{\pi^2 \sqrt[4]{2}} \\ \overline{Nu}_\lambda(Re) &= \frac{0.664 Re Pr^{1/3}}{\sqrt{Re} + \sqrt{Re_0}} \left\{ 1 - \left\| 1, \frac{Re_u}{Re} \right\|_{-2} \right\} \quad \Xi = \left\| 1, \frac{0.5}{Pr} \right\|_{\sqrt{1/3}} \end{aligned}$$

— $Re_u/Re \equiv x_u/L$ is the unheated leading fraction.

— Convection $Pr = Pr_w^{1/4} Pr_\infty^{3/4}$; Pr_w is at plate temperature; Pr_∞ is at free stream temperature.

- Periodicity combined with isotropy enables modeling of flows along many plate roughness geometries using few parameters: characteristic length L , RMS height-of-roughness ε , isotropic spatial period L_P , openness Ω , and, for plateau roughness, L^* of the periodic cell's convex region.
- The algorithms presented find ε , L_P , and Ω from an elevation grid of a square portion of the rough surface.
- A plate surface is isotropic, periodic roughness when its $L/L_P \gg 1$.

The following conclusions are for plates with $L_P > \varepsilon > 0$ and $L/L_P \gg 1$:

- An isotropic, periodic roughness with $Re_\sigma > L/\sqrt{\varepsilon L_P}$ behaves as a smooth surface with $Re_c = L/\sqrt{\varepsilon L_P}$ when $Re < Re_\lambda$.

$$Re_\sigma = \frac{\sqrt{3} L}{3^3 \varepsilon} \exp \frac{L_P}{3^3 \varepsilon} \quad Re_\lambda = \left[\frac{0.664}{\varepsilon} \right]^2 L_P L$$

- The average skin-friction coefficient \overline{f}_ρ and average forced convection \overline{Nu}_ρ of rough turbulence are:

$$\overline{f}_\rho = \frac{1}{3 \ln^2(L/\varepsilon)} \quad \overline{Nu}_\rho = \frac{Re Pr^{1/3}}{6 \ln^2(L/\varepsilon)} \quad \frac{L}{\varepsilon} \gg 1$$

- Fluid flow will be rough turbulent in the leading band of roughness when $Re > \max(Re_\sigma, Re_\lambda)$.
- Fluid flow will be rough turbulent along the entire surface when $\Omega > 1/2$ and $Re > \max(Re_\sigma, Re_\lambda)$.
- The peaks of an isotropic, periodic roughness with $\Omega < 1/2$ are co-planar areas comprising most of the plate. Designated “plateau roughness”, these surfaces can shed a mix of rough and smooth turbulence when $Re > \max(Re_\sigma, Re_\lambda)$. Plateau roughness formulas were presented and tested.

The present theory was tested with 456 convection and friction measurements in 32 data-sets from one book, six peer-reviewed studies, and the present apparatuses.

- Relative to the present work formulas, the 32 data-set's RMSRE values span 0.75% through 8.2%.
- Only four of the 32 data-sets have RMSRE exceeding 6%.

22. Nomenclature

A	surface area (m^2)
$C_f/2, \overline{C_f}/2$	local, average skin-friction coefficient Mills-Hang [8] and Pimenta et al. [7]
$C_m/2$	average skin-friction coefficient Churchill [11]
c_p	fluid specific heat at constant pressure ($\text{J}/(\text{kg} \cdot \text{K})$)
$c_f, \overline{c_f}$	local, average skin-friction coefficient Prandtl-Schlichting [3]
$f_c, \overline{f_c}$	local, average skin-friction coefficient present work
$G(t, w)$	Gray-code self-similar ramp-permutation
h, \overline{h}	local, average convective surface conductance ($\text{W}/(\text{m}^2 \cdot \text{K})$)
j_P	period index, the index of largest $ X_j $ or $ X_{j,k} $
k	fluid thermal conductivity ($\text{W}/(\text{m} \cdot \text{K})$)a
k_S	sand-roughness (m)
L	plate characteristic length (m)
L_P	roughness spatial period (m)
L^*	ratio of plateau convex region area to its perimeter (m)
Nu, \overline{Nu}	local, average Nusselt number (convection)
Pr	Prandtl number of fluid
q	positive integer = $\log_2 w$
Re	Reynolds number of flow parallel to the plate
Re_c	purely laminar upper-bound
Re_I, Re_W	Re_x rough-to-smooth turbulence threshold
Re_λ, Re_σ	laminar, smooth turbulent Re upper-bound
Re_ε, Re_k	roughness, sand-roughness Reynolds number
Re_x	local Reynolds number = $x Re/L$
Re_0	Re_x integration lower bound
Re_u	Re_x of leading unheated band
$S_{j,k}$	matrix of elevations
t	integer
Tu	free-stream turbulence ratio
u, u_τ	bulk fluid, friction velocity (m/s)
$W(t, w)$	wiggliest integer self-similar ramp-permutation
W_0	principal branch of the Lambert W function
w	integer power of two = 2^q
$X_j, X_{j,k}$	discrete Fourier transform coefficient
x, x_u	distance, unheated distance from leading edge of plate (m)
$Y(t, w)$	integer self-similar ramp-permutation
Z	roughness random variable (m)
$z(x), z(x, y)$	roughness elevation function (m)
\bar{z}	mean elevation of roughness function (m)

22.1 Greek Symbols.

γ, γ'	exponent p of the ℓ^p -norm
δ_2	momentum thickness of boundary-layer flow (m)
$\delta_{2\lambda}, \delta_{2\sigma}$	laminar, smooth turbulence momentum thickness (m)
ϵ, ε	profile, surface RMS height-of-roughness (m)
ν	fluid kinematic viscosity (m^2/s)
Ω	ratio of non-plateau area to cell area (m^2/m^2)
ρ	fluid density (kg/m^3)
τ, τ_2	fluid shearing stress (N/m^2)
ς	peak elevation of roughness (m)
φ, ϑ	mathematical scalar variables

Acknowledgments

The idea of self-similar roughness grew from a discussion with Nina Koch about turbulence self-similarity. Thanks to John Cox (1957-2022) and Doug Ruuska for machining the bi-level plate. Thanks to Martin Jaffer for critiques and insights. Thanks to anonymous reviewers for their useful suggestions.

Abbreviations

The following abbreviations are used in this manuscript:

PIR	polyisocyanurate foam
PLL	phase-locked loop
RAM	random access memory
RH	relative humidity
RMS	root-mean-squared $\sqrt{\sum_{i=1}^n x_i^2/n}$
RMSRE	root-mean-squared relative error
RSS	root-sum-squared $\sqrt{\sum_i x_i^2}$
UHF	uniform heat flux
USB	Universal Serial Bus
UWT	uniform wall temperature, isothermal
XPS	extruded polystyrene foam

23. References

- [1] L Prandtl. Zur turbulenten stromung in rohren und längs platten. *Ergebnisse der Aerodynamische Versuchsanst zu Göttingen*, 4:18–29, 1932.
- [2] T. von Kármán. Theorie des reibungswiderstandes [theory of the frictional resistance]. In *Hydromechanische Probleme des Schiffsantriebs*, pages 50–73, Hamburg, Germany, 1932. Springer.
- [3] L. Prandtl and H. Schlichting. *The Resistance Law for Rough Plates*. Translation (David W. Taylor Model Basin). Navy Department, the David W. Taylor Model Basin, 1934. Translated 1955 by P.S. Granville.
- [4] J. Nikuradse. Laws of flow in rough pipes. *VDI Forschungsheft*, page 361, 1933. Translated 1937 by A. A. Brielmaier.
- [5] H Schlichting. Experimental investigation of the problem of surface roughness. Technical Report TM 823, NACA, Washington, DC, 1937.
- [6] F. R. Hama. Boundary layer characteristics for smooth and rough surfaces. *Trans. Soc. Nav. Arch. Marine Engrs.*, 62:333–358, 1954.
- [7] M. M. Pimenta, R. J. Moffat, and W. M. Kays. *The Turbulent Boundary Layer: An Experimental Study of the Transport of Momentum and Heat with the Effect of Roughness*. Department of Mechanical Engineering, Stanford University, 1975.
- [8] A. F. Mills and Xu Hang. On the skin friction coefficient for a fully rough flat plate. *J. Fluids Eng*, 105(3):364–365, 1983, doi:10.1115/1.3241008.
- [9] Hermann Schlichting. *Boundary-Layer Theory*. McGraw Hill, New Delhi, seventh edition, 2014. Translated by Kestin, J.
- [10] Frank White. *Viscous Fluid Flow*. McGraw-Hill, 3rd edition, 2006.
- [11] Stuart W. Churchill. Theoretically based expressions in closed form for the local and mean coefficients of skin friction in fully turbulent flow along smooth and rough plates. *International Journal of Heat and Fluid Flow*, 14(3):231 – 239, 1993, doi:10.1016/0142-727X(93)90053-P.
- [12] C. F. Colebrook. Turbulent flow in pipes, with particular reference to the transition region between the smooth and rough pipe laws. *Journal of the Institution of Civil Engineers*, 11(4):133–156, 1939, doi:10.1680/ijoti.1939.13150.

- [13] Javier Jiménez. Turbulent flows over rough walls. *Annual Review of Fluid Mechanics*, 36(1):173–196, 2004, doi:10.1146/annurev.fluid.36.050802.122103.
- [14] D. J. Bergstrom, O. G. Akinlade, and M. F. Tachie. Skin Friction Correlation for Smooth and Rough Wall Turbulent Boundary Layers. *Journal of Fluids Engineering*, 127(6):1146–1153, 04 2005, doi:10.1115/1.2073288.
- [15] J. H. Lienhard, IV and J. H. Lienhard, V. *A Heat Transfer Textbook*. Phlogiston Press, Cambridge, MA, 5th edition, August 2020. Version 5.10.
- [16] D. W. Smith and J. D. Walker. Skin friction measurements in incompressible flow. Technical Report R-26, NASA, Washington, DC, 1959.
- [17] D. B. Spalding and S. W. Chi. The drag of a compressible turbulent boundary layer on a smooth flat plate with and without heat transfer. *Journal of Fluid Mechanics*, 18(1):117143, 1964, doi:10.1017/S0022112064000088.
- [18] A. Žukauskas and A. Šlančiauskas. *Heat Transfer in Turbulent Fluid Flows*. Hemisphere Publishing Corp, Washington, DC, 1987.
- [19] F. Gebers. Ein beitrag zur experimentellen ermittlung des wasserwiderstandes gegen bewegte köper. *Schiffbau*, 9:435 – 452, 475 – 485, 1908.
- [20] F. Gebers. Das ähnlichkeitsgesetz für den flächenwiderstand in wasser geradling fortbewegter polierter platten. *Schiffbau*, 22:687 – 930, 1920 - 1921.
- [21] J. Kestin, P.F. Maeder, and H.E. Wang. Influence of turbulence on the transfer of heat from plates with and without a pressure gradient. *International Journal of Heat and Mass Transfer*, 3(2):133–154, 1961, doi:https://doi.org/10.1016/0017-9310(61)90076-X.
- [22] W. C. Reynolds, W. M. Kays, and S. J. Kline. Heat transfer in the turbulent incompressible boundary layer, part 4 – effect of location of transition and prediction of heat transfer in a known transition region. Technical Report NASA-MEMO-12-4-58W, NASA, 1958.
- [23] Noor Afzal, Abu Seena, and A. Bushra. Turbulent flow in a machine honed rough pipe for large reynolds numbers: General roughness scaling laws. *Journal of Hydro-environment Research*, 7(1):81–90, 2013, doi:10.1016/j.jher.2011.08.002.
- [24] Karen A Flack, Michael P Schultz, Julio M Barros, and Yechan C Kim. Skin-friction behavior in the transitionally-rough regime. *International Journal of Heat and Fluid Flow*, 61:21–30, 2016, doi:10.1016/j.ijheatfluidflow.2016.05.008.
- [25] Mitchell G. Newberry and Van M. Savage. Self-similar processes follow a power law in discrete logarithmic space. *Phys. Rev. Lett.*, 122:158303, Apr 2019, doi:10.1103/PhysRevLett.122.158303.
- [26] RJ Goldstein, EM Sparrow, and DC Jones. Natural convection mass transfer adjacent to horizontal plates. *International Journal of Heat and Mass Transfer*, 16(5):1025–1035, 1973, doi:10.1016/0017-9310(73)90041-0.
- [27] JR Lloyd and WR Moran. Natural convection adjacent to horizontal surface of various planforms. *Journal of Heat Transfer*, 96(4):443–447, 1974, doi:10.1115/1.3450224.
- [28] Aubrey Jaffer. Natural convection heat transfer from an isothermal plate. *Thermo*, 3(1):148–175, 2023, doi:10.3390/thermo3010010.
- [29] V Lienhard, John H. Heat Transfer in Flat-Plate Boundary Layers: A Correlation for Laminar, Transitional, and Turbulent Flow. *Journal of Heat Transfer*, 142(6), 04 2020, doi:10.1115/1.4046795. 061805.
- [30] Allan P. Colburn. A method of correlating forced convection heat-transfer data and a comparison with fluid friction. *International Journal of Heat and Mass Transfer*, 7(12):1359 – 1384, 1964, doi:10.1016/0017-9310(64)90125-5.

- [31] S. W. Churchill and R. Usagi. A general expression for the correlation of rates of transfer and other phenomena. *AIChE Journal*, 18(6):1121–1128, 1972, doi:10.1002/aic.690180606.
- [32] E. O. Tuck and A. Kouzoubov. A laminar roughness boundary condition. *Journal of Fluid Mechanics*, 300:5970, 1995, doi:10.1017/S0022112095003600.
- [33] G. B. Schubauer and H. K. Skramstad. Laminar-boundary-layer oscillations and transition on a flat plate. Technical Report NACA-TR-909, NASA, 1948.
- [34] J. Kiefer. Sequential minimax search for a maximum. *Proceedings of the American Mathematical Society*, 4(3):502–506, 1953.
- [35] K. Kadoya, N. Matsunaga, and A. Nagashima. Viscosity and thermal conductivity of dry air in the gaseous phase. *Journal of Physical and Chemical Reference Data*, 14(4):947–970, 1985, doi:10.1063/1.555744.
- [36] Arnold Wexler. Vapor pressure formulation for water in range 0 to 100°C. a revision. *Journal of research of the National Bureau of Standards*, 80A(5-6):775–785, 1976, doi:0.6028/jres.080A.071.
- [37] P.T. Tsilingiris. Thermophysical and transport properties of humid air at temperature range between 0 and 100°C. *Energy Conversion and Management*, 49(5):1098–1110, 2008, doi:https://doi.org/10.1016/j.enconman.2007.09.015.
- [38] Z. K. Morvay and D. D. Gvozdenac. Toolbox 6: Thermodynamic and transport properties of moist air. In *Applied Industrial Energy and Environmental Management Part III: Fundamentals for Analysis and Calculation of Energy and Environmental Performance*. John Wiley & Sons, Ltd, 2016.
- [39] Syeileendra Pramuditya. Water thermodynamic properties. Technical report, Bandung Institute of Technology, Jl. Ganesha 10, Bandung, Indonesia, 2011.
- [40] W. Wagner and A. Pruß. The iapws formulation 1995 for the thermodynamic properties of ordinary water substance for general and scientific use. *Journal of Physical and Chemical Reference Data*, 31(2):387–535, 2002, doi:10.1063/1.1461829.
- [41] M. F. Blair. Influence of Free-Stream Turbulence on Turbulent Boundary Layer Heat Transfer and Mean Profile Development, Part II—Analysis of Results. *Journal of Heat Transfer*, 105(1):41–47, 02 1983, doi:10.1115/1.3245557.
- [42] W. C. Reynolds, W. M. Kays, and S. J. Kline. Heat transfer in the turbulent incompressible boundary layer, part 1 – constant wall temperature. Technical Report NASA-MEMO-12-1-58W/PT1, NASA, 1958.
- [43] Jiyuan Tu, Guan-Heng Yeoh, and Chaoqun Liu. Chapter 3 - governing equations for cfd: Fundamentals. In Jiyuan Tu, Guan-Heng Yeoh, and Chaoqun Liu, editors, *Computational Fluid Dynamics*, pages 65–124. Butterworth-Heinemann, third edition, 2018.
- [44] R.W. Rice. Emittance factors for infrared thermometers used for wood products. *Wood and Fiber Science*, 36:520–526, 2004.
- [45] Eva Barreira, Ricardo M. S. F. Almeida, and Maria L. Simes. Emissivity of building materials for infrared measurements. *Sensors*, 21(6), 2021, doi:10.3390/s21061961.
- [46] R.B. Abernethy, R.P. Benedict, and R.B. Dowdell. Asme measurement uncertainty. *ASME. J. Fluids Eng.*, 107(2):161–164, 1985, doi:10.1115/1.3242450.

24. Appendix A: Convection Measurement Apparatus and Methodology

This goal of the present apparatus was to measure forced convection from a precisely rough plate over the widest practical span of flow rates.

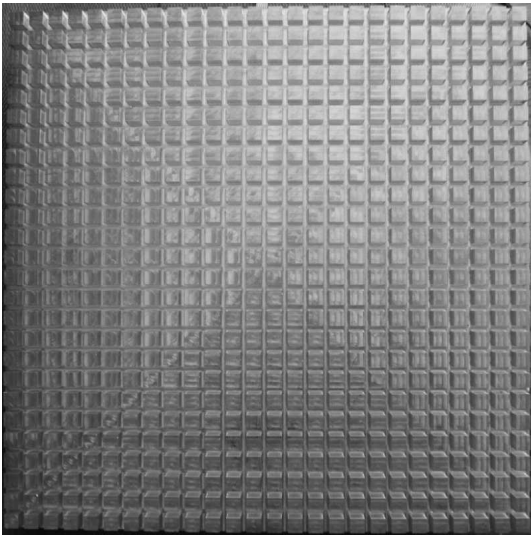


Figure 57 Rough surface of plate

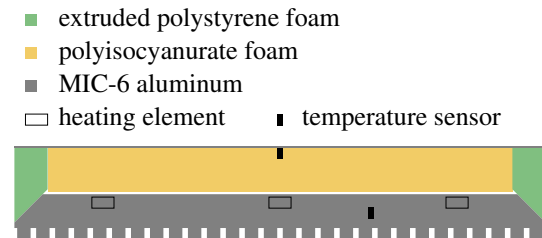


Figure 58 Plate assembly cross-section

24.1 The Plate. Figure 57 shows the rough surface of the test plate; it was milled from a slab of MIC-6 aluminum (Al) to have (676 of) square $8.33 \text{ mm} \times 8.33 \text{ mm} \times 6 \text{ mm}$ posts spaced on 11.7 mm centers over the $30.5 \text{ cm} \times 30.5 \text{ cm}$ plate. The area of the top of each post was 0.694 cm^2 , which was 50.4% of its 1.38 cm^2 cell. The RMS height-of-roughness $\varepsilon = 3.00 \text{ mm}$. Openness $\Omega \approx 49.6\%$. Embedded in the plate are 9 electronic resistors as heating elements and a Texas Instruments LM35 Precision Centigrade Temperature Sensor. 2.54 cm of thermal insulating foam separates the back of the plate from a 0.32 mm thick sheet of aluminum with an LM35 temperature sensor at its center. Figure 58 is a cross-section illustration of the plate assembly.

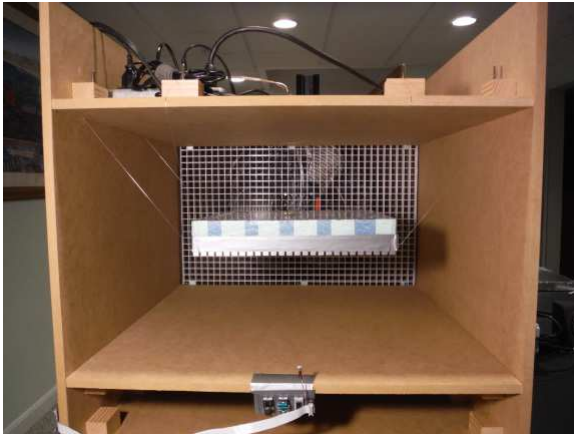


Figure 59 $\varepsilon = 3 \text{ mm}$ plate in wind-tunnel

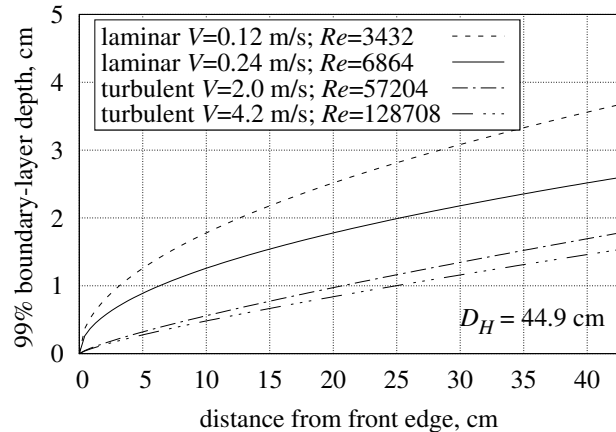


Figure 60 Wind-tunnel boundary-layers

24.2 Wind Tunnel. The fan pulls air from the test chamber's open intake through the test chamber. The fan blows directly into a diffuser made of folded plastic mesh to disrupt vortices generated by the fan. In a sufficiently large room, the disrupted vortices dissipate before being drawn into the open intake.

To guarantee isobaric (no pressure drop) flow, the wind-tunnel must be sufficiently large that its test chamber and plate assembly boundary-layers do not interact at fan-capable airspeeds.

The wind-tunnel test chamber in Figure 59 has a $61 \text{ cm} \times 35.6 \text{ cm}$ cross-section and a 61 cm depth. This allows the plate assembly to be centered in the wind-tunnel with 15 cm of space on all sides. The fan pulling air through the test chamber produces a maximum airspeed of 4.65 m/s ($Re \approx 9.2 \times 10^4$ along the

30.5 cm square plate). Its minimum nonzero airspeed is 0.12 m/s ($Re \approx 2300$).

Test chamber laminar and smooth turbulent 99% boundary-layer thicknesses (Schlichting [9]) are:

$$\delta_\lambda = 4.92 \sqrt{\frac{x\nu}{u}} \quad \delta_\sigma = 0.37 x^{4/5} \left[\frac{\nu}{u}\right]^{1/5} \quad (106)$$

Figure 60 shows that the 15 cm clearance between the plate and the test chamber walls is sufficient to prevent their boundary-layers from interacting at airspeeds within the fan’s capabilities.

The plate assembly is suspended from six lengths of 0.38 mm-diameter steel piano wire terminated at twelve zither tuning pins in wooden blocks fastened to the exterior of the test chamber. The plate is suspended face down to minimize the natural convection from the test-surface. With the plate assembly in the test chamber, the airspeed increases in proportion to the reduction of test chamber aperture A_e by the plate’s cross-sectional area A_x :

$$\frac{u_x}{u} = \frac{A_e}{A_e - A_x} \approx 107.6\% \quad (107)$$

24.3 Automation. Data capture and control of convection experiments are performed by an “STM32F3 Discovery 32-Bit ARM M4 72MHz” development board. The program written for the STM32F3 captures readings and writes them to the microprocessor’s non-volatile RAM, controls the plate heating, servos the fan speed, and later uploads its data to a computer through a USB cable.

Once per second during an experiment, the program calibrates and reads each on-chip 12 bit analog-to-digital converter 16 times, summing the sixteen 12 bit readings to create a 16 bit reading per converter.

Rotations of the fan are sensed when a fan blade interrupts an infrared beam. The microprocessor controls a solid-state relay (supplying power to the fan) to maintain a fan rotation rate, ω , which is dialed into switches. At $\omega \leq 210$ r/min, the microprocessor pulses power to the fan to phase-lock the beam interruption signal to an internal clock. At $\omega > 210$ r/min, the microprocessor servos the duty cycle of a 7.5 Hz square-wave gating power to the fan. This system operates at $32 \text{ r/min} < \omega < 1400 \text{ r/min}$.

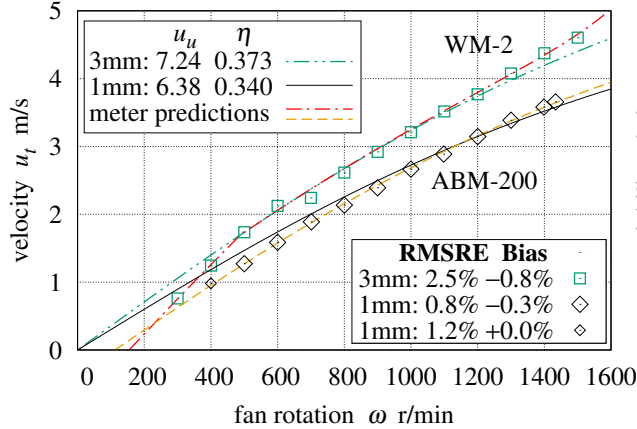


Figure 61 Airspeed versus fan speed

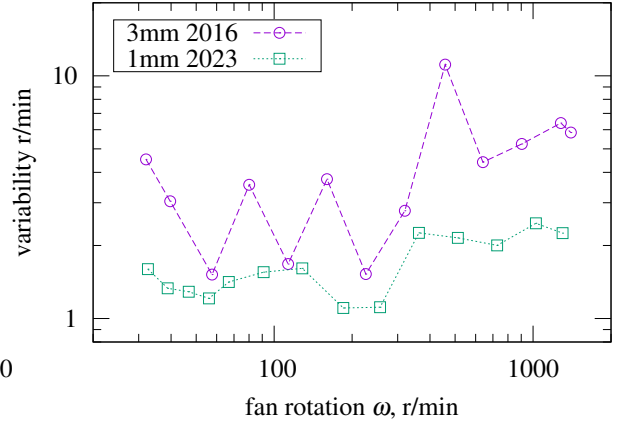


Figure 62 Fan PLL variability

24.4 Calibration. The correspondence between fan rotation rate ω and test chamber airspeed u was determined using an “Ambient Weather WM-2”, which specifies an accuracy of $\pm 3\%$ of reading. After 2017 an “ABM-200 Airflow & Environmental Meter” specifying an accuracy of $\pm 0.5\%$ of reading between 2.2 m/s and 62.5 m/s, was used.

The “UtiliTech 20 inch 3-Speed High Velocity Floor Fan” has three blades with maximum radius $r = 0.254$ m. Its characteristic length is its hydraulic-diameter, $D_H = 0.550$ m. The velocity of the blade tips is $2\pi r\omega/60$, where ω is the number of rotations per minute. The Reynolds number of the fan is:

$$Re_f = \frac{2\pi r D_H \omega / 60}{3\nu} \quad (108)$$

The 3 blade tips trace the whole circumference in only $1/3$ of a rotation, hence the 3 in the denominator.

Faster fan rotation ω yields diminishing increases of test-chamber airspeed u_t , suggesting formula (109), where u_u is the limiting flow rate for arbitrarily fast rotation, and coefficient η converts fan Re_f to test-chamber flow rate Re_t . Figure 61 gives the parameters and measurements at $300 \text{ r/min} \leq \omega \leq 1500 \text{ r/min}$. The “3mm” points are the WM-2 measurements of the 3 mm plate in the original wind-tunnel; The “1mm” points are the ABM-200 measurements of the 1 mm plate in the tunnel with a new diffuser and fan cowling.

$$Re_t = \|\eta Re_f, D_H u_u/\nu\|_{-2} \quad u_t = \|\pi \eta r \omega/90, u_u\|_{-2} \quad (109)$$

Airspeeds slower than 2 m/s should be nearly proportional to ω . Both anemometers show evidence of dry (bearing) friction in Figure 61. The ABM-200 “meter predictions” trace plots $1.125 u_t - 0.381$; the WM-2 “meter predictions” trace plots $1.477 u_t - 0.81$ when $u_t < 1.725$ and u_t otherwise. A mistake in the 2016 measurement software under-counted fan rotations at $\omega > 1200 \text{ r/min}$. It is compensated by replacing ω in formulas (108, 109) with $[\omega^{-6} - 1750^{-6}]^{-1/6}$ in the WM-2 “meter predictions”. The RMSRE and Bias are relative to the “meter predictions”. The second “1mm” row includes the point at 400 r/min.

Figure 62 shows the fan speed variability for each downward-facing experiment; these are used by the measurement uncertainty calculations. The differences reflect improvements in the fan-control software.

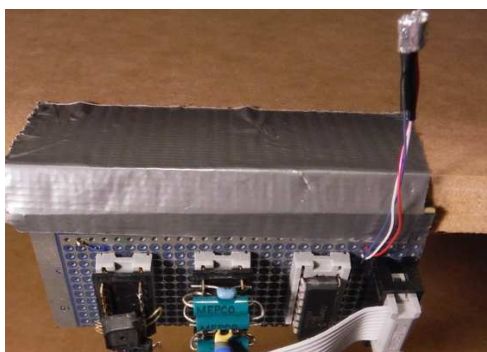


Figure 63 Ambient sensors

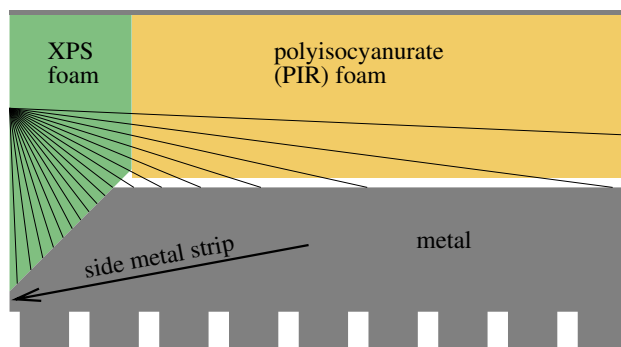


Figure 64 XPS wedge conduction

24.5 Ambient Sensing. Figure 63 shows the ambient sensor board which was at the lower edge of the test chamber in Figure 59. It measures the pressure, relative humidity (RH), and air temperature at the wind-tunnel intake. Wrapped in aluminum tape to minimize radiative heat transfer, the LM35 temperature sensor projects into the tunnel. To minimize self-heating, the LM35 is powered only while being sampled.

Table 14 Physical parameters

Symbol	Values	Description
L	0.305 m	length of flow along test-surface
A	0.093 m ²	area of test-surface
ϵ	3.00 mm 1.04 mm	RMS height-of-roughness
C_{pt}	4691 J/K 4274 J/K	plate thermal capacity
D_{Al}	19.4 mm	metal slab thickness
D_{PIR}	25.4 mm	polyisocyanurate (PIR) foam thickness
D_w	19.05 mm	XPS foam wedge height
k_{PIR}	0.0222 W/(m · K)	PIR foam thermal conductivity
k_{XPS}	0.0285 W/(m · K)	XPS foam thermal conductivity
U_I	0.075 W/K	front-to-back insulation thermal conductance
ϵ_{Al}	0.04	test-surface (MIC-6 Al) emissivity
ϵ_{XPS}	0.515	XPS foam emissivity (see text)
ϵ_{dt}	0.89	duck tape emissivity
ϵ_{wt}	0.90	test chamber interior emissivity

24.6 Physical Parameters. Table 14 lists the static parameters from measurements and specifications.

The effective ϵ_{wt} may differ from the medium-density-fiberboard emissivity given by Rice [44] because the temperatures of the test chamber surfaces may not be uniform. Through the open intake, the plate also exchanges thermal radiation with objects in the room having different temperatures.

24.7 Modeling of Parasitic Heat Flows. At low airflow rates, the sides of the insulation behind the test plate can leak more heat than the test-surface transfers, shrinking to 6% at 1300 r/min. To compensate, expected side heat transfers will be subtracted from the (combined) measured heat flow.

Figure 59 shows duck tape applied to the lower 54% of the plate's side, which corresponds to 50% coverage of the XPS foam wedge. For this partial tape coverage, ϵ_W formula (110) is the area proportional mean of the duck tape emissivity and XPS emissivity. Barreira, Almeida, and Simões [45] measured ϵ_{dt} emissivities of 0.86 and 0.89 from two brands of "duck tape"; the larger value is used for the aged tape on the plate sides. As of this writing, published emissivity measurements of XPS foam have not been located.

$$\epsilon_W = 50\% \epsilon_{dt} + 50\% \epsilon_{XPS} \quad (110)$$

Relative to the theory in Jaffer [28], natural convection measurements ($u = 0$) from the plate assembly over the span of inclinations have less than 2.8% RMSRE when calculated with $\epsilon_{XPS} = 0.515$; the RMSRE increases to either side of 0.515. This value is consistent with natural convection measurements of the plate assembly without tape.

The four sides are not isothermal; a 3.5 mm metal strip (see cross-section Figure 64) runs the length of the side; and a D_w -tall wedge of extruded polystyrene foam (XPS) insulation fills the metal slab's 27 mm ($= \sqrt{2} D_{Al}$) 45° chamfer. The local surface conductance $h_W(z)$ at elevation z (from the wedge point) is found by averaging the reciprocal distance to slab metal with respect to angle θ :

$$\begin{aligned} h_W(z) &= \int_0^{\theta_c} \frac{k_{XPS}}{\sqrt{2} z \theta_c} \cos\left(\theta + \frac{\pi}{4}\right) d\theta + \int_{\theta_w}^{\theta_W} \frac{k_{PIR}}{z - D_w} \frac{\cos \theta}{\theta_W - \theta_w} d\theta \\ &= \frac{k_{XPS}}{\sqrt{2} z \theta_c} \left[\sin\left(\theta_c + \frac{\pi}{4}\right) - \sin \frac{\pi}{4} \right] + \frac{k_{PIR}}{z - D_w} \left[\frac{\sin \theta_W - \sin \theta_w}{\theta_W - \theta_w} \right] \\ \theta_c &= \arctan \frac{D_w - z}{D_w} \quad \theta_w = \arctan \frac{D_w}{z - D_w} \quad \theta_W = \max\left(\theta_w, \arctan \frac{L - D_w}{z - D_w}\right) \end{aligned} \quad (111)$$

Forced air flows parallel to the long dimension on two sides, but flows into the windward side and away from the leeward side. Air heated by the windward side reduces heat transfer from the test-surface; air heated by the test-surface suppresses heat transfer from the leeward side. Hence, the model excludes windward and leeward forced convection. The total forced convective conductance of the flow-parallel foam wedges is calculated by integrating $h_W(z)$ in series (reciprocal of the sum of reciprocals, which is also the ℓ^{-1} -norm) with the local surface conductance $k Nu_c(Re_x)/L$, where $Nu_c(Re_x)$ is the pierced-laminar convection calculated by applying the $\overline{Nu}_\sigma \rightarrow Nu_\sigma$ transform (75) to the pierced-laminar convection formula (91):

$$U_W = \int_0^{D_w} \int_0^L \left\| h_W(z), \frac{k Nu_c(Re_x)}{L} \right\|_{-1} dx dz \quad (112)$$

The natural convection flow from the vertical faces is upward, perpendicular to the horizontal forced flow; hence, the forced convection U_W and the natural convective conductance $k L L' \overline{Nu}'/L' = k L \overline{Nu}'$ combine as the ℓ^2 -norm (introduced in Section 13). The resulting mixed convective conductance is in mild competition with the side radiative conductance, $U_R = \epsilon_W \epsilon_{wt} h_R L D_w$; they combine as the $\ell^{\sqrt{2}}$ -norm:

$$U_S(u) = 2 \left\| U_R, \left\| U_W, k L \overline{Nu}' \right\|_2 \right\|_{\sqrt{2}} + 2 \left\| U_R, k L \overline{Nu}' \right\|_{\sqrt{2}} \quad (113)$$

Each of the four side's natural convective conductance is \overline{Nu}' vertical plate formula (114) from Jaffer [28], with characteristic length $L' = D_{Al} + \sqrt{2}\epsilon$, where the metal slab thickness $D_{Al} \approx 19.4$ mm.

$$\begin{aligned} \overline{Nu}' &= \left\| \frac{Nu'_0}{2}, \frac{Nu'_0{}^{4/3}}{8 \sqrt[3]{2}} \left[\frac{Ra}{\Xi(Pr)} \right]^{1/3} \right\|_{1/2} \\ \Xi(Pr) &= \left\| 1, \frac{0.5}{Pr} \right\|_{\sqrt{1/3}} \quad Nu'_0 = \frac{8^{5/4}}{\pi^2} \end{aligned} \quad (114)$$

24.8 **Measurement Methodology.** The measurement methodology employed is unusual. Instead of waiting until the plate reaches thermal equilibrium, the plate is heated to 15 K above ambient, heating stops, the fan runs at the designated speed, and convection cools the plate. All of the sensor readings are captured each second during the 102 minute process, Table 15 lists the dynamic physical quantities measured each second. Table 16 lists computed quantities. Both $U_S(u)$ and $\{\epsilon_{A1} \epsilon_{wt} h_R A\}$ are subtracted from the combined heat flow. The mean of $\bar{h}(u, t)$ over the time interval in which ΔT drops by half (or exceeds 6142 s total time) is the result from that experiment.

Table 15 Dynamic quantities

Symbol	Units	Description
ω	r/min	fan rotation rate
T_F	K	ambient air temperature
T_P	K	plate temperature
T_B	K	back surface temperature
P	Pa	atmospheric pressure
Φ	Pa/Pa	air relative humidity

Table 16 Computed quantities

Symbol	Units	Description
h_R	W/(m ² K)	radiative surface conductance
$U_S(u)$	W/K	side radiative and convective conductance
$\bar{h}(u, t)$	W/(m ² K)	convective surface conductance

24.9 **Heat Balance.** Collecting into $U_T(u)$ formula (115) those terms which have a factor of temperature difference $\overline{T_P} - \overline{T_F}$, formula (116) is the heat balance equation of the plate during convective cooling:

$$U_T(u) = U_S(u) + \{\bar{h}(u) A\} + \{\epsilon_{A1} \epsilon_{wt} h_R A\} \quad (115)$$

$$0 = U_T(u) [\overline{T_P} - \overline{T_F}] + U_I [\overline{T_P} - \overline{T_B}] + C_{pt} \frac{d\overline{T_P}}{dt} \quad (116)$$

The plate and ambient temperatures are functions of time t . Determined experimentally during heating, the temperature group-delay through the 2.54 cm block of insulation between the slab and back sheet is 110 s:

$$\overline{T_P}(t) = \frac{U_T(u) \overline{T_F}(t) + U_I \overline{T_B}(t - 110 \text{ s}) - C_{pt} [d\overline{T_P}(t)/dt]}{U_T(u) + U_I} \quad (117)$$

To compute Nusselt number $\overline{Nu} = \bar{h} L/k$, equation (117) is solved for the $\{\bar{h}(u, t) A\}$ term from equation (115).

$$\zeta(u, t) = -U_I [\overline{T_P}(t) - \overline{T_B}(t - 110 \text{ s})] \quad (118)$$

$$\{\bar{h}(u, t) A\} = \frac{\zeta(u, t) - C_{pt} [\overline{T_P}(t) - \overline{T_P}(t')]/[t - t']}{\overline{T_P}(t) - \overline{T_F}(t)} - \{\epsilon_{A1} \epsilon_{wt} h_R A\} - U_S(u) \quad (119)$$

where t' is the previous value of t . In equations (118) and (119), $\overline{T_P}(t)$, $\overline{T_F}(t)$, and $\overline{T_B}(t)$ are the 15-element cosine averages of plate and fluid temperatures (centered at time t).

24.10 **Measurement Uncertainty.** Following Abernethy, Benedict, and Dowdell [46], the final steps in processing an experiment's data are:

- 1) Using equation (119), calculate the sensitivities of convected power $\bar{h} A \Delta T$ per each parameter's average over the measurement time-interval;
- 2) multiply the absolute value of each sensitivity by its estimated parameter bias to yield component uncertainties;
- 3) calculate combined bias uncertainty as the root-sum-squared (RSS) of the component uncertainties;
- 4) calculate the RSS combined measurement uncertainty as the RSS of the combined bias uncertainty and twice the product of the rotation rate sensitivity and variability.

Table 17 Estimated measurement uncertainties, bi-level 3mm roughness at $Re = 59593$					
Symbol	Nominal	Sensitivity	Bias	Uncertainty	Component
ΔT	9.47K	+12.2%/K	0.10K	1.22%	LM35C differential
P	101kPa	+0.0009%/Pa	1.5kPa	1.28%	MPXH6115A6U air pressure
C_{pt}	4.69kJ/K	+0.024%/(J/K)	47J/K	1.14%	plate thermal capacity
η	0.401	+180%	0.014	2.52%	anemometer calibration
ς	6.00mm	+11299%/m	100um	1.13%	post height
				3.50%	combined bias uncertainty
Symbol	Nominal	Sensitivity	Variability	Uncertainty	Component
ω	905r/min	+0.081%/(r/min)	5.2r/min	0.43%	fan rotation rate
				3.60%	RSS combined uncertainty

Table 18 Estimated measurement uncertainties, bi-level 1mm roughness at $Re = 55935$					
Symbol	Nominal	Sensitivity	Bias	Uncertainty	Component
ΔT	10.2K	+11.8%/K	0.10K	1.18%	LM35C differential
P	100.0kPa	+0.0008%/Pa	1.5kPa	1.26%	MPXH6115A6U air pressure
C_{pt}	4.24kJ/K	+0.028%/(J/K)	42J/K	1.18%	plate thermal capacity
η	0.340	+195%	0.003	0.66%	anemometer calibration
u_u	6.381	+2.44%	0.100	0.24%	diffuser airflow upper bound
L_T	8.34mm	+9361%/m	100um	0.94%	post length
L_m	3.57mm	+473%/m	500um	0.24%	side metal strip width
ϵ_{rs}	0.040	+21.3%	0.010	0.21%	test-surface emissivity
ϵ_{wt}	0.900	+9.48%	0.025	0.24%	wind-tunnel emissivity
				2.45%	combined bias uncertainty
Symbol	Nominal	Sensitivity	Variability	Uncertainty	Component
ω	1.03kr/min	+0.065%/(r/min)	2.5r/min	0.16%	fan rotation rate
				2.48%	RSS combined uncertainty

Tables 17 and 18 list the sensitivity, bias, and uncertainty for each component contributing more than 0.20% uncertainty for the 3 mm and 1 mm roughness plates, respectively. Figures 65 and 66 show the measurements relative to the present theory for rough turbulence and smooth turbulence, respectively.

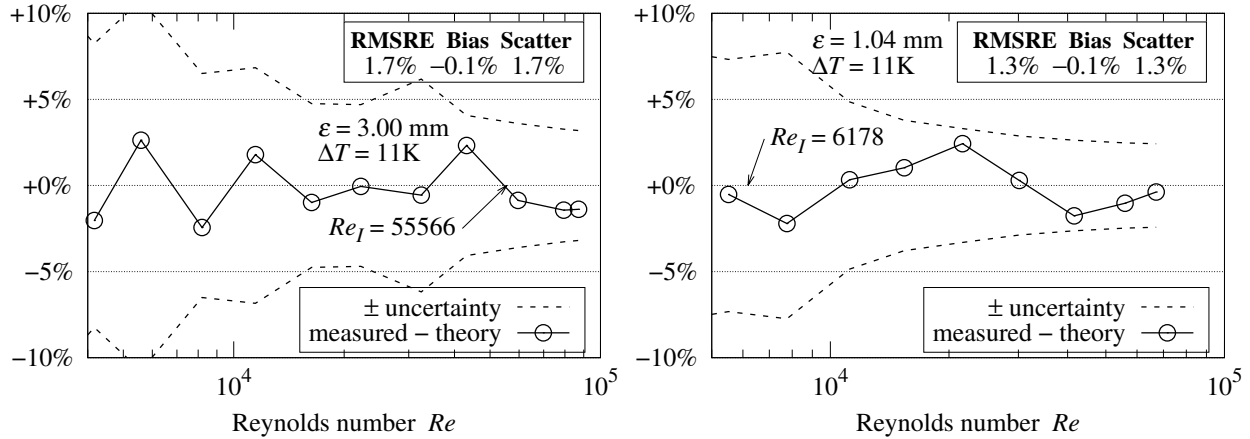


Figure 65 Measured versus theory $\epsilon = 3$ mm Figure 66 Measured versus theory $\epsilon = 1$ mm

24.11 Details. Documentation, photographs, electrical schematics, and software source-code for the apparatus, as well as calibration and measurement data are available from:

<http://people.csail.mit.edu/jaffer/convect>

25. Appendix B: Thermal and Transport Properties of Humid Air

Wexler [36] approximates the (partial) pressure of saturated water vapor as:

$$P_v = \exp\left(-0.63536311 \times 10^4/T + 0.3404926034 \times 10^2 - 0.19509874 \times 10^{-1}T + 0.12811805 \times 10^{-4}T^2\right)$$

where T is absolute temperature in Kelvins.

An ideal gas has density $\rho = PM/[\bar{R}T]$, where the gas constant $\bar{R} = 8.314 \text{ J}/(\text{kg} \cdot \text{mol})$. Air with relative humidity $0 < \phi < 1$, modeled as a mixture of dry air and water vapor, has density:

$$\rho = \frac{M_a [P - \phi P_v] + M_v \phi P_v}{\bar{R}T}$$

where the molar masses of air and water are $M_a = 28.97 \times 10^{-3} \text{ kg/mol}$ and $M_v = 18.0153 \times 10^{-3} \text{ kg/mol}$.

Tsilingiris [37], approximates the specific heats of dry air and water vapor:

$$\begin{aligned} c_{pa} &= +1034 - 0.2849T + 0.7817 \times 10^{-3}T^2 \\ &\quad - 0.4971 \times 10^{-6}T^3 + 0.1077 \times 10^{-9}T^4 \\ c_{pv} &= +1869 - 0.2578[T - 273.15] + 1.941 \times 10^{-2}[T - 273.15]^2 \\ c_p &= \frac{c_{pa}[1 - \chi_p]M_a + c_{pv}\chi_p M_v}{[1 - \chi_p]M_a + \chi_p M_v} \quad \chi_p = \phi P_v/P \end{aligned}$$

Morvay and Gvozdenac [38], approximate the viscosity of air and water vapor as:

$$\begin{aligned} \mu_a &= +0.40401 \times 10^{-6} + 0.074582 \times 10^{-6}T - 5.7171 \times 10^{-11}T^2 \\ &\quad + 2.9928 \times 10^{-14}T^3 - 6.2524 \times 10^{-18}T^4 \\ \mu_v &= \frac{10^{-6} \gamma^{-1/2}}{0.0181583 + \gamma [0.0177624 + \gamma [0.0105287 - \gamma 0.0036744]]} \end{aligned}$$

where $\gamma = 647.27/T$. They combine these into dynamic viscosity μ using absolute humidity χ , the mass ratio of water vapor to air.

$$\begin{aligned} \chi &= \frac{M_v \phi P_v}{M_a [P - \phi P_v]} \quad r_m = M_a/M_v \quad \chi_m = \chi r_m \\ \Phi(r_m, r_\mu) &= \left[1 + \frac{\sqrt{r_\mu}}{\sqrt[4]{r_m}}\right]^2 \sqrt{\frac{1}{8[1 + r_m]}} \\ \mu &= \frac{\mu_a}{1 + \Phi(r_m, \mu_a/\mu_v)\chi_m} + \frac{\mu_v}{1 + \Phi(1/r_m, \mu_v/\mu_a)/\chi_m} \end{aligned}$$

Morvay and Gvozdenac [38] approximates the thermal conductivity of water vapor at $t = T - 273.15$:

$$\begin{aligned} k_v &= +1.74822 \times 10^{-2} + 7.69127 \times 10^{-5}t - 3.23464 \times 10^{-7}t^2 \\ &\quad + 2.59524 \times 10^{-9}t^3 - 3.17650 \times 10^{-12}t^4 \end{aligned}$$

Kadoya, Matsunaga and Nagashima [35] approximates the thermal conductivity of dry air as:

$$\begin{aligned} k_a &= 0.0259778 \left(+0.239503 T_r + 0.00649768 \sqrt{T_r} + 1.0 - 1.92615/T_r \right. \\ &\quad + 2.00383/T_r^2 - 1.07553/T_r^3 + 0.229414/T_r^4 \\ &\quad + 0.402287 \rho_r + 0.356603 \rho_r^2 - 0.163159 \rho_r^3 \\ &\quad \left. + 0.138059 \rho_r^4 - 0.0201725 \rho_r^5 \right) \end{aligned}$$

where

$$\rho_r = \frac{P/314.3}{287.058 T} \quad T_r = \frac{T}{132.5}$$

Both Morvay and Gvozdenac [38] and Tsilingiris [37] develop the combined thermal conductivity k as:

$$k = \frac{k_a}{1 + \Phi(r_m, r_\mu)\chi_m} + \frac{k_v}{1 + \Phi(1/r_m, 1/r_\mu)/\chi_m} \quad r_\mu = \mu_a/\mu_v$$